POLITECNICO
MILANO 1863

Active Opto-Magnetic Biosensing System On Chip

Doctoral dissertation in Physics

Author: **Piero Borga**

Student ID: 922853
Supervisor: Prof. Andrea Melloni
Tutor: Prof. Riccardo Bertacco
Chair of PhD program: Prof. Marco Finazzi
PhD cycle: XXXIV
Year: 2022

Abstract

Biosensors are tools that became nearly essential to the present day, being widely exploited in various fields. From water quality check to patient clinical analysis, the knowledge evolution lead to the necessity of having a precise and accurate way to measure the characteristics of the sample under test. Based on different technologies, divided in many branches depending on the use case and with different levels of requirements, biosensors mostly are composed by several parts. From the sample preparation to the result interpretation, a biosensor is a system that needs to strongly integrate all the different steps and parts to reduce costs and simplify operator's job while improving detection performances such as speed and limit of detection. The development of a biosensor needs to take into considerations very different subsystems to be accurately joined and make them work properly.

This thesis condenses three years of PhD work focused on biosensing technology in integrated photonics. During this period the main goals were to study and implement a new biosensing technique and to apply the knowledge to design and build a system that could be easily prototyped.
First, the development of a system and then a diagnostic device have been completed. In collaboration with several partners from a regional project, we designed, realized and tested a machine to be used in hospital laboratories for diagnostic purposes. Then we theorized, implemented and successfully demonstrated a new biosensing technique, here named opto-magnetic, that exploits magnetic nanoparticles as labels activated by external magnetic fields. The promising results in terms of interrogation time and theoretical limit of detection, comparable to the state of the art, led us to keep evolving the technology. In order to increase robustness and improve reliability of the system towards a possible prototyping, we studied a new chip in silicon photonics platform that integrates the optical sensor and the magnetic field generator possibly improving the performances and suitable for large-volumes and low-cost production.

To sum up, during this PhD, we developed systems for biosensing with optical platforms. Essential to this path have been the relations with other research and industrial groups, to merge different expertise and create something new, from idea to the real world object.

Lot of time has been spent in experimental and system improving activities, learning how to apply the correct approach, maximize the outcomes, reduce risks and keep the research standards up to the maximum levels.

Preface

This thesis reports the most relevant works carried out by the author, Piero Borga, during the Doctoral studies in Physics at Politecnico di Milano under the supervision of Prof. Andrea Melloni and Prof. Riccardo Bertacco.

The experimental activity was mainly performed in two different laboratories of Politecnico di Milano: the Photonic Devices Laboratory and the micro- and nano-fabrication facility Polifab, from November, 1st 2018 to January, 31st 2022.

The works resulted in the following pubblications and contributions to international conferences:

Journal articles

- "Active Opto-Magnetic Biosensing with Silicon Microring Resonators", Sensors 2022, 22, 3292 [1]

- "Differential Impedance Sensing platform for high selectivity antibody detection down to few counts: A case study on Dengue Virus", Biosensors and Bioelectronics 202, 2022, 113996 [2]

Conference contributions

- "Dynamic labelling for enhanced biosensing with silicon microring resonators", ECIO 2022

- "Control of programmable photonic integrated meshes for free-space optics applications", OSA Advanced Photonic Congress 2020

- "Integrated optomagnetic platform for biosensing applications", JEMS 2019

- "Manipulating optical beams with a programmable silicon photonic mesh", PIERS 2019

- "Processing free space optical beams with a silicon photonic mesh", ECIO 2019

- "Opto-magnetic platform for biosensing applications", Ricerca e innovazione in fisica medica e biomedica: la Lombardia risponde, AIFM 2019

If it works, it's obsolete

Contents

Introduction

In this introductory chapter the whole work is presented. An introduction to biosensors is given, to provide a context to the reader and to start exposing the nature of the problems that may occur when developing a device devoted to biosensing applications.

Health care and biosensing

Referred to Gross Domestic Product (GDP), health care expenditure is one of the top largest voice if we look at developed countries. In the last 20 years the world GDP increased by 74% (Figure 1a), while global spending on health more than doubled in the same period (Figure 1b) showing a net growth around 9%. However, expenditures are not the same for all the countries, with the poorest nations unable to spend large portions of their GDP. As shown in Figure 1c the higher income countries can put up to 8% of the GDP in health care, while other nations cannot afford such expense [3]. In particular, very poor countries mostly rely on external aid to cover health expenses.

Large amounts of money flowing into health care both from public and from private funds (Figure 1d) push the continuous innovation inducing a better life quality and life expectancy to increase. One important aspect in the health field is biosensing: a set of techniques and tools that are capable to detect, measure and quantify the presence and the concentration of a specific molecule in biological samples.

A system for biosensing

A biosensor is basically the device that detects and measure a targeted substance in a given solution, that could be organic or inorganic. They can be used in various applications such drug discovery, disease monitoring, detectors for pollutants, disease-causing micro-organisms and markers that indicates health issues.

Biosensors research history starts centuries ago, and a good example could be the introduction of mice and canaries into coal mines. Having small dimensions and a basal metabolic rate higher than workers, the Serinus Canaria birds in particular exhibit poi-
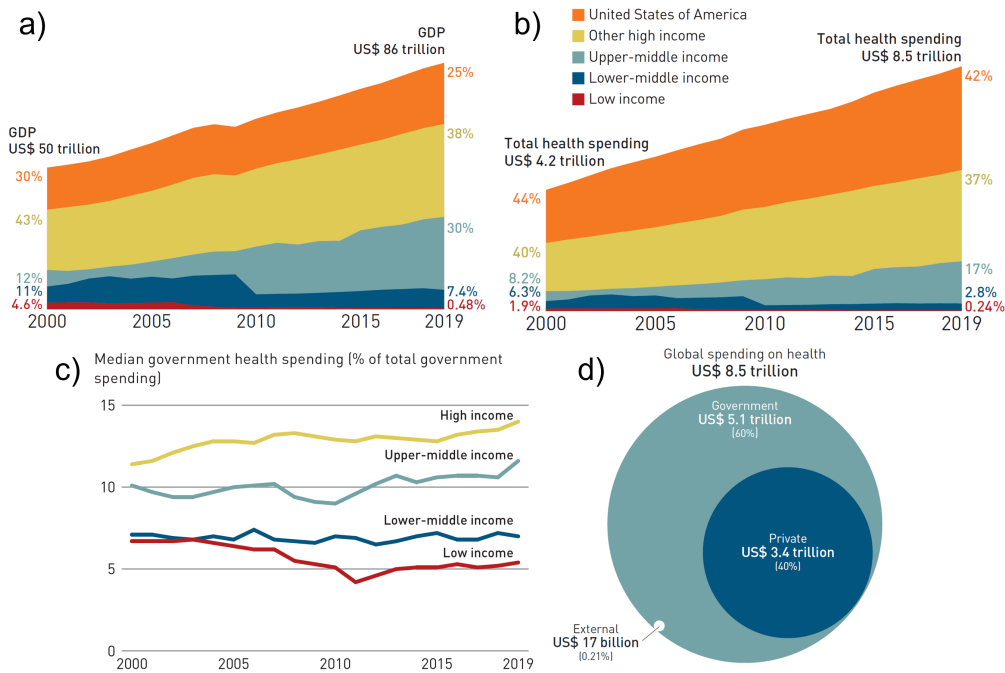
Figure 1: Health expenditure over the world in the last two decades. (**a**) Global GDP; (**b**) global expenses for health; (**c**) percentage of internal GDP allocated to health; (**d**) health funds origin. From [3].

soning symptoms before gas concentrations could become truly dangerous for the people in the cave. The animal fainting was a clear signal that something in the air was off from the safe values [4, 5].

In 1906 the first biosensing demonstration proved that the acid concentration in a liquid is proportional to the electric potential between two parts of the liquid separated by a glass membrane. After few years the concept of pH was introduced and sensor development started exploding. First as industrial related sensing, then after the '60s focusing also on health applications.

Nowadays biosensor are a mixture of different fields, a truly multidisciplinary area of research since biosensors examples can be found in almost any type of platform and technology niche, as shown in Figure 2.

Biosensors, although in different technologies, present the same components, that will be discussed later: an analyte to be measured, the bioreceptor that attracts and binds the analyte, the transducer element that converts the biochemical information into another form of energy that has to be processed by a proper electronics. A final processing of the data might be needed, as well as an interface to easily read the result.
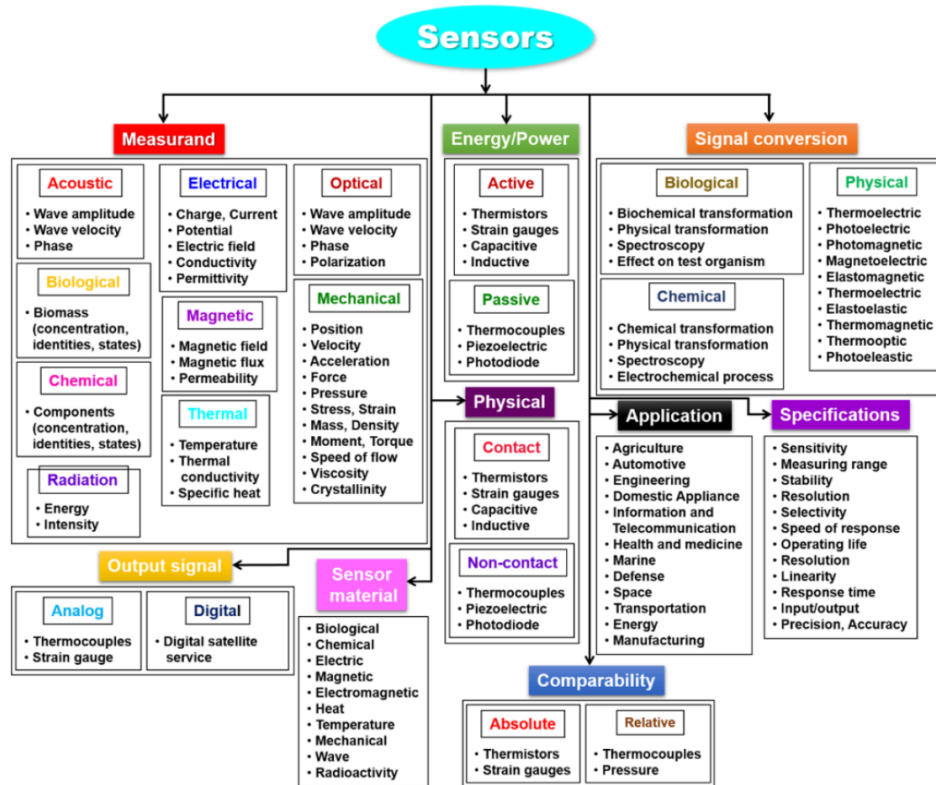
Figure 2: Sensors come in many variants, with different technologies and approaches. From [6].

These components have to be accurately assembled into a system without creating conflicts and assuring the characteristics that make a biosensor valuable: selectivity to avoid false positives measurements, reproducibility to have constant values on same samples measurements, stability to be robust against disturbances, sensitivity to detect low concentrations as desired and linearity to have a direct relation between the measured concentration and the output signal.

Lab on a chip

Thanks to the strong development in the recent years it is now possible to miniaturize the biosensors' components, reducing the overall size of tools that just few years ago were impossible to fit on a desk. The miniaturized sensors, that incorporate the sample preparation and management as well as the other building blocks and that are capable of performing most of the required steps usually performed in a laboratory, are called Lab On a Chip (LOC). A LOC that integrates the possibility to perform all the steps, from the sample collection to the result illustration, would be one of the best achievement in modern medicine and technology.

Plus, the road to miniaturization of such testing devices brings other important features: low volume of samples are required to perform the tests, less materials are needed to build smaller devices, efficiency is higher because of the easier control of the little volumes, nanofabrication technologies allow a strong integration of multiple devices in the same sensor with a limited effect on the external dimensions.

Once realized a small, easy to use and cheap device, this could really be an innovation, being used in point of care locations or directly at patients' homes.

Accomplishment and original work

This work is focused on the realization and the testing of a system for biosensing and diagnostics that can be easily employed and possibly developed into a LOC.

Classical hybridization schemes, both in label-free and label-based approaches, are possible in our optical platform with an experimental bench setup designed and tested with relatively low cost instrumentation. With the regional project READy partners we designed, assembled and tested a diagnostic tool prototype to be tested at hospital laboratories with human samples.

We then developed a new active labelling technique to enhance sensing capabilities of the optical sensors. The sensing system joins photonics, magnetism, fluidics and electronics to obtain the fully working new technique. New interrogation methods have been studied and applied to obtain results in line with the state of the art capabilities, using chips that show low sensitivity. The setup assembly and the measurement method were improved over time, validating the chosen research path.

The integration in a single chip of the opto-magnetic platform have been first simulated to find the best solutions in accordance to fabrication requirements and tolerances and then fabricated. The newly designed control electronics will allow to test the chips and verify the actual capabilities.

This thesis is the natural continuation of all the effort put by my colleagues P. Sharma [7], C. Groppi and in particular N. Peserico [8].

The author personally contributed in the majority of the described activities. Specifically: theoretical analysis of the problem, numerical simulations, design of experiments, assembly and maintenance of experimental setup, software programming for laboratory testing and automation, experiments and measurements performing, data collection, analysis and interpretation of the results.

The original work and the project achievements generated several conferences contributions and have been published in scientific journals.

Thesis overview

The thesis is organized following this order:

- The first chapter focuses the attention on the optical biosensing. In the first section the different parts of a biosensors are illustrated in more details reporting some notable examples. Then, some important biosensing principles, in particular related to optical technologies, are presented like the several figures of merit that we may use and the biosensing labelling approaches. The chapter continues with descriptions of different optical technologies employed in biosensing. In the list, non comprehensive of all the possible optical solutions, results from the state of the art are reported. To conclude the chapter we mention some existing platforms and techniques that already join optical sensing with magnetic particles labelling.

- In the second chapter we go into detail of part of our work on biosensing detection, with a focus on the hybridizations, both label free and labelled. First the used microchip is described, having care to specify the additional fabrication steps we have done on it. Then we introduce the biomolecules used for the conducted tests, with the functionalization and hybridization processes descriptions. Later on, the experimental part becomes more relevant, with details of the laboratory setup and how it works. The obtained measurements are then illustrated, with some commenting on the results. At the end of the chapter, we report the designing and realization of a diagnostic device, tested with human samples infected by Dengue virus in the framework of a regional project devoted to reduce the risk of future bioemergencies.

- In the third chapter we introduce the biosensing technique developed in our laboratories: the opto-magnetic. The labels used in the technique, the magnetic nanoparticles, are briefly reviewed with some basic concepts, nanoparticles' structure description and their behaviour in presence of external magnetic fields. Then we go through the active labelling technique and its working principle, exposing the relation between the external stimulus of the label and the optical response. A deeper analysis on the expected sensor output is then provided, with considerations on the waveguide technology and the label position. Then the experimental setup description highlights what are the needed tools to perform the tests, with the measurement methods illustrated after that. Finally, the results are collected showing the possible improvement that our new technique could provide to refractive index sensors used for biosensing.

- The fourth chapter is directed towards the future of the opto-magnetic technique.

The generation of magnetic field is moved inside the microchip. Various possible solutions are analyzed and the effects of the new magnetic fields on nanoparticles and biomolecules are studied. A new photonic chip has been designed, with the goal in mind to enhance the capabilities of the approach. Performances estimations of the renovated optical and magnetic structures are reported. To drive the fabricated chip with the new concepts, a control electronics is necessary and its design is described at the end of the chapter.

- The final conclusion offer a recap of the work and the advantages of the implemented technique with some considerations on possible future developments.

1 | Optical Biosensing Systems

Biosensors are evolving at an increased rate year by year. The more we know about the world, the more we want to detect, analyse and measure. This is even more true in medical field thanks to the strong advances in healthcare technologies: health checks, diagnosis and cure processes are received by patients with more and more attentions, leading to an increased life expectancy and, more importantly, to a better life quality.

So, if few years ago we just needed to know if a certain antibody was present or not in the bloodstream of a patient, we now want to know how much of it there is, how other parameters are affected by its presence, how the situation will evolve and what is the best way for the patient to recover if needed. These auspicable new performances require a constant evolution of the biosensors, both in term of sensing technology and of system integration.

1.1. Biosensor parts

Biosensors development is a multidisciplinary activity. Transferring a biochemical composition to an information requires some major building blocks that are all part of the biosensor: the solution containing the biological sample, the suitable layer meant to probe that sample, the transducing element generating a readable signal from the biochemical events and the system detecting and processing the information allowing the user to understand the result of the assay.

Biological sample

The sample to be analysed can be of very different kind, with the main applications being with gaseous and liquid media. Gas sensors are particularly used to detect specific air components in a broad range of applications like air quality monitoring system both indoor and outdoor and environmental science, but also find a large use in medical field, automotive and military industry [10]. Integrated photonics for gas sensing is a promising platform and, despite not having yet a market, it is seeing a great performances evolution in the last years [11]. The most common applications are dedicated to liquid substances.
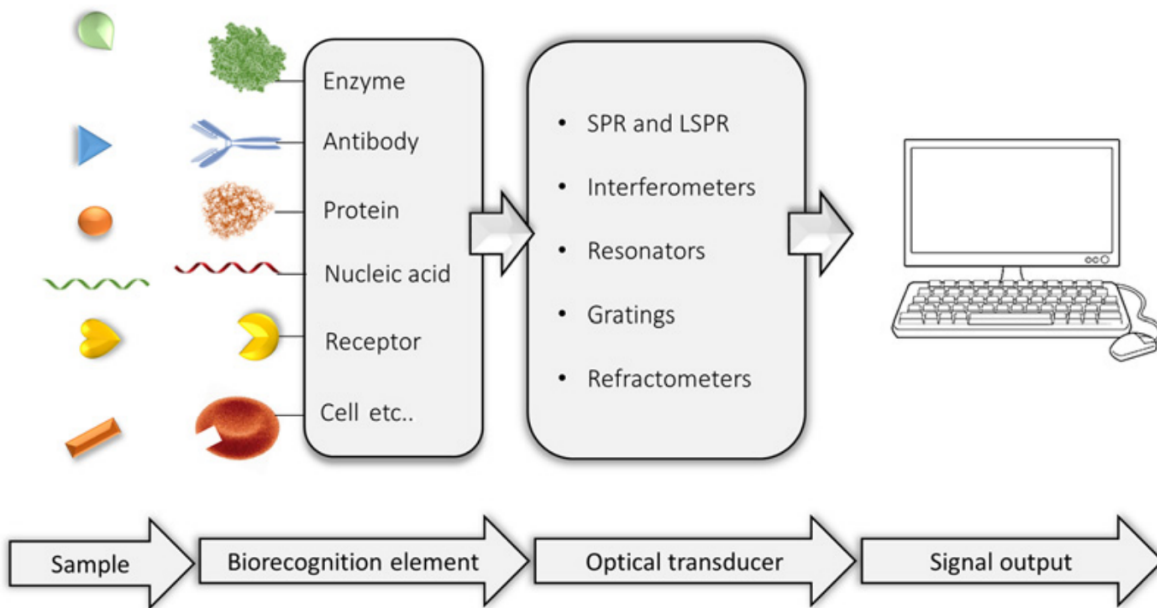
Figure 1.1: A biosensor is a complex of multi subsystems, each dedicated to a specific task. From [9].

Dissolved contaminants in sea and river, industry and laboratory wastes, water quality in public aqueducts [12] are large fields where sensors are widely used. The application where photonic sensors are showing huge potential is the sensing for health. Blood, plasma, urines, sweat [13] are just some of the possible biological fluids under tests that can be used to diagnose a specific illness, track the evolution of a condition or periodically check the generic health state of a patient. As example, conventional blood analysis delivers the sample to dedicated laboratories, where several techniques can be used to perform the different studies, with required times ranging from 12-72h. Human blood, composed by more than 4000 bio-constituents other than the most known red blood cells and white blood cells, is a complex fluid to manage and blood plasma presents proteins, minerals, vitamins, hormones, glucose, dissolved gases and so on. The load of insight on a patient's health that a biological fluid can give is huge and the correct extraction of these information is fundamental to let diagnostics and health sciences develop.

The fluid under test usually must be prepared before the analysis. Sample preparation techniques, e.g. liquid-liquid or liquid-solid extraction and protein precipitation, are classified into analyte separation from the matrix, unwanted or endogenous material removal, selectivity and sensitivity enhancing and basic liquid handling procedures like solvent dilutions [14–17]. The preparation is usually performed by laboratory technician, however new systems are implementing automatic sample preparation for routine procedures [18].

To convey the sample in contact with the sensitive device, fluidic systems need to be used. Comprising a pumping device, sometimes a circuit selector, a cell and a waste collector, fluidics is allowing to facilitate many molecular binding processes. In particular fluidic cells are widely used in laboratories [19] and for commercial applications [20] since different technologies have been developed to fabricate them for various cases [21]. The most used typologies are fabricated in Polymethilmethacrylate (PMMA), a plastic material to be processed usually by numerical control mill, and in Polydimetilsiloxane (PDMS), a polymer that through microfabrication methods can form micrometer size fluidic channel [22] as in Figure 1.2.
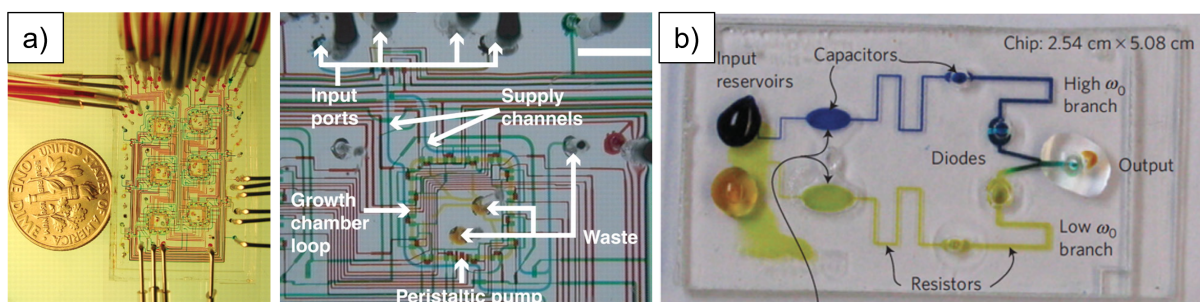

Figure 1.2: Examples of fluidic cells: they can be used just for liquid transportation or to perform complex tasks. From [22, 23].

Biochemical layer

To attract and capture the analyte on the sensitive element, a biochemical layer is needed. The biochemical layer is formed starting from the functionalization of the biosensor surface [24] and a widely used technique to achieve it is to perform a surface silanization, typically with APTES molecules that bond their $-NH_2$ terminations to the silicon oxide layer. Then, the probes can be attached to the surface either by immersing the chip into the receptors solution or by depositing with the use of a microarray spotter, that allows a multiplexing detection on a single surface [25].

Another technique is the use of particular polymers that can coat the surface and bind the receptors keeping them in a conformal configuration, avoiding molecule folding and consequently improving the efficiency thanks to the increased concentration of binding sites.

The choice of the receptor is based on the analyte to be detected and measured. Usually the biosensors are classified into different categories depending on the receptor: ligand biosensors are based on the interaction between the receptor and the biological analyte, called ligand; immunosensors exploit the attraction between an antibody and the relative

antigen and are widely used in medicine; nucleic acid biosensors relies on the strong affinity between two complementary strands of oligonucleotides and are largely used both in medicine and in applied research to test new biosensors and biosensing techniques.

Transducer element

Transforming biochemical events to processable information is the role assumed by the transducing elements. Most of them are designed to generate an electrical signal, so it can be acquired by a proper electronic system. All transducers categories exploit a different physics concept and the most common in biosensing are gravimetric, electronic, impedance, magnetoresistive and optical biosensors.

Gravimetric transducers are based on mass changes. Micro Electro-Mechanical Systems (MEMS), and in particular micro cantilevers, can be covered by receptor molecules that attract the analytes. Then, due to the mass difference, the structure is deflected. A piezoelectric material can translate the deflection magnitude to a measurable electric signal. Another method is to look at the light shined on the moving surface from a laser source: the deflection changes the direction of the reflected beam, giving the mass count. Many MEMS [26] work on frequency-shift measurement: a suspended mass is put in oscillation and the analyte change this overall mass by a measurable factor when looking at the resonating frequency.

Electronic biosensors in their recent versions are mostly based on the working principle of the field effect transistor (FET). The current flowing between source and drain is determined by the charges that are induced in the insulator above the channel on the layer covered by receptors. In the BioFET [27], the charges are generated by the analytes binding to the surface and the current that starts flowing can be accurately measured. The small footprint and the high sensitivity of these devices are pushing the research for optimal solutions.

Impedance biosensors are based on the measurement of changes in impedance between electrodes that are interdigitated. Capturing the analyte, the media between the electrodes change conductivity properties and using a single frequency this variation can be accurately detected [2, 28]. Signal amplification can be performed by using polystyrene particles attached in a second step to the analyte in a labelled assay.

Magnetoresistive biosensors exploits changes in the electrical properties of certain materials or structures when a magnetic particle approaches. Due to the small magnetism present in biology, molecular labels are needed. Widely spread are platform that use the magnetic tunnelling [29], Hall effect [30] and giant magnetic resistance [31, 32].

Optical biosensors are the focus of this work and to detect they exploit a difference in refractive index caused by the binding molecules. Incident light on a surface or propagating in a waveguide produces evanescent electromagnetic field outside of the structure. The evanescent tail is affected by the environment and in this case by the analyte binding to the receptor molecules [33]. The generated disturbance can be detected in various ways that will be presented in the next Section.

Signal processing

The extracted information from the events detected by the sensors' transducing component need to processed to be readable and to offer a simple interpretation. Some of the briefly presented transducers generate a directly acquirable current or voltage signal, while others need a bit of more processing and calculation to provide valuable results that can be understood by the user [34]. Signal processing approaches strongly depends on the type of input, i.e. the transducer's outcome, and on the requested output, i.e. how the sensor communicates the result.

1.2. Biosensing principles

Here, descriptions of some important biosensing principles are presented. First we explain the different Figures Of Merit (FOM) that define a biosensor, then we briefly clarify the possible labelling approaches for an assay.

1.2.1. Figures of merit

In very general terms, a biosensor's quality can be defined by a list of parameters that are the FOM.

Time

A biosensing analysis should be fast. A biosensor that returns the result faster than a competitor's, given the same performances, it is definitely a better device. However, some speed limits are imposed by biological constraints and are due to the affinity between molecules and their diffusion in the buffer. In particular, depletion and diffusion impose a trade off between the ability to detect small quantities and the speed achievable. Plus, a limited time to perform the sensing could have detrimental effects on the measurement robustness. Typically, have a complete result in around one hour can be considered a good target for a biosensor if compared with the days usually required to perform clinical

tests.

Complexity

It is particularly difficult to avoid complexity in a biosensor. The different parts described before have all their own specific needs that prevent to develop a simple device. The preparation of the sample, the fluidics to obtain its efficient transportation along with other solutions to manage biochemical protocols and routines, the physical sensor with its interactions with the environment and the biology, the processing of the collected data, and so on. Moreover, having multiple analytes or a detection multiplexed in subsequent steps have huge impacts on the complexity of the system. Last but not least is the user interface: the more a biosensor is wide-spreaded and mass adopted, the more it has to deal with non expert users. In order to look simple it has to hide the complexity behind a graphical user interface for control and a data processing and data presenting software that require additional resources to be developed.

Cost

Regarding the price of the biosensor, it obviously needs to be as low as possible. An high cost could limit the use of the biosensor to a bunch of applications in few laboratories. Techniques can be used to lower production costs without affecting reliability, in particular to fabricate the sensor and the interrogation system. The higher costs usually come from the technological parts with sensor and interrogation system fabrication and from the biochemical part with the receptor and the preparation of the sample. A hybrid system between fixed (instrumentation and reading electronics) and disposable (sensors and fluidics in cartridges) components can be the best solution to cut costs without affecting robustness and reliability.

Selectivity

As already seen, the choice of the biological interface over the sensing area depends on the analyte that we want to detect and measure. The same layer is responsible for the sensor's selectivity, its ability to attract the analyte of interest while ideally having no interactions with other biomolecules. The study of biomolecule affinity in the biochemical layer is fundamental to develop a sensor that reacts only when needed and it is not affected by other biological species that can increase the readout noise and false the results.

Sensitivity

An useful biosensor should be able to detect the analyte at the quantity we are looking for. Great research effort is put in developing biosensors able to detect very low quantities down to the single-molecule, but also a wide sensitivity range is important for many applications. To define the sensitivity, the biochemistry literature uses different terms due to the difference between the various possible analytes and receptors: a certain terminology may be more adapted to certain analyte than to other molecules.

The Limit of Detection (LoD) is the minimum amount of a certain species that can be detected. It is usually given in molar concentration (M or mol/L) and specify the number of molecules in a certain volume that can be detected by the system. For biosensors that use samples with reduced volumes, this means that for fixed concentrations also the number of analyte moles to be detected is small and it can be an issue, while with larger volumes, more molecules are present in the system and can bound to the receptors. Strictly confined in the optical world, in optical biosensing LoD can be also expressed in Refractive Index Units (RIU), indicating the smallest variation in refractive index that can be detected by the biosensor. A FOM more related to waveguide-based sensors is the bulk sensitivity that will be better explained later.

Another FOM that is widely used is the surface mass density, which is usually expressed mass/surface (pg/mm^2) and indicates the minimum mass bound to the sensing surface that can be detected. It is a powerful parameter, but refractive index and density differences between molecules reduce the universality of this FOM. Moreover, being used to indicate the LoD, it omits all the information regarding the sensor linearity range.

That is why in literature all these different FOM are found, depending on the considered analyte. Plus, the choice of transducer technology affects the convenience to use one FOM or another, since to analyse the overall sensitivity one can separate different terms, each one related to different aspect of the technology in use. An example is provided in Chapter 3 for the analysis of the overall sensitivity of an opical microring resonator.

1.2.2. Label-free and label-based approaches

In biosensors, the quantification of physiological states need to assume that the intensity of the acquired signal is in some way proportional to the quantity of detected analyte. It is important, as already seen, to reduce the complexity of the sensor as well as the complexity of the assay reducing the steps, simplifying the materials and samples preparation and the protocol, i.e. the sequence of actions needed to complete the assay. However, sometimes can be problematic to decipher and understand the abundance of analyte in a solution, in particular if it is close or below the level of sensitivity relative to the used

method.

To address this issue, two distinct approaches have been exploited, depending on the particular situation: label-free and label-based detection schemes. Label-free measurements are all those schemes in which the acquired signal is directly generated by the analyte interacting with the receptor and no means are used to enhance the effect [35]. In contrast, label-based methods of detection use labels that are attached to or incorporated within the biological target, causing a tangible difference in the experimental conditions and the outcome of the test [36].

The most known label-based technique is the Enzime Linked ImmunoSorbent Assay (ELISA), shown in Figure 1.3. On a solid surface an antibody is immobilized, then a target solution, dispensed on the surface, puts in contact antibody and antigen and they bind, completing the first biomolecular recognition. Then, to add more stringency to the measure, more material (in the example the secondary antibody) is added that will bind to the target molecule specifically. The analyte becomes sandwiched between the receptor and the secondary antibody, from which the name *sandwich immunoassay*. To enhance the outcome, a label particle is added to bind to the secondary antibody.
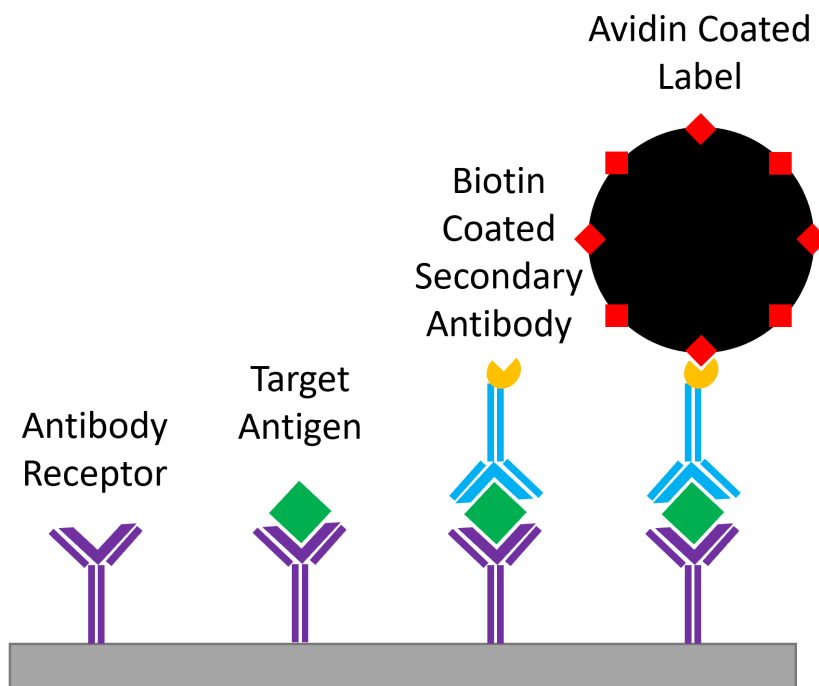

Figure 1.3: Classical ELISA steps for antigen detection. Receptor, target and additional biomolecules used as labels bind together allowing the detection.

Labels are used to improve the result exploiting the sensitivity to particular parameters of the detection method: an avalanche photodiode will be sensible to fluorescent emission so fluorescent dye will be used, while a high refractive index label could be better for

a refractive index sensitive platform. It is common to perform the binding between the biomolecular sandwich and the label making use of the biotin-avidin strong affinity, so usually the secondary antibody are already functionalized with biotin vitamin to create a stable complex with the avidin or streptavidin protein functionalized label. Due to the sensibility enhancement generated by the addition of detectable labels and the assay robustness thanks to the specific target-label binding, label-based approaches are usually preferred. However, a complete specificity in detection is not possible in real samples and a minimum effect from aspecific binding has to be expected, causing possible false positive results. Multiplexing is also possible with labels, by using markers adequately functionalized in order to bind to different molecules. With labelled sensing real-time measurements are no longer a necessity. The comparison between outcomes of different times are not needed to evaluate the entity of the biomolecular recognition: on-demand system interrogations can be implemented, producing an off-line detection that need to be monitored after the binding process thanks to the presence and properties of the labels. But of course these advantages come at the expense of assay duration and complexity due to the extra binding steps that need to be performed, with all the complications implied.

To avoid or reduce those issues there is a strong development of devices that can be used in label-free configurations aiming to reduce time duration, complexity and used material costs while maintaining the sensitivity high enough to detect and recognize slight modification in the environment caused by the molecules. Limits and advantages are present in both label-free and label-based typologies of biosensors, so an interesting research line consists in trying to combine the two detection approaches: a fast label-free assay for high analyte concentrations and then labelled steps to obtain the higher sensitivity and robustness needed for the assay.

Labelling techniques can be furthermore divided into two categories: passive or active.

Passive labels bring their physical properties in the sensing process and enhance the signal by just interacting with the analyte or the sensor, e.g. with an extra massive particle or, in the case of optical biosensors, a large refractive index difference with respect to the buffer solution. Examples of passive labels can be the exploitation of a massive particles [37, 38] like latex particles [39], liposomes [40], massive proteins [41] or metallic nanoparticles [42] due to their dielectric constant, high density, ease of preparation and biocompatibility [43].

Active labels add to the assay some peculiarities specific of the used marker to induce an externally observable signal exploiting their intrinsic properties. Being the labels chosen specifically for the application, the output signal should be strongly dependent on the presence of the active label, in order to possibly achieve a high specificity. Being active,

their activity can be switched on and off in a reversible way, thus paving the way for new sensing strategies: real-time measurements for the whole duration of the assay are not necessary anymore and a reduction of spurious contributions is expected. Active labels can be of very different typologies: enzymes [44], charged molecules [45], radio-isotopes [46] and fluorescent molecules [47] are widely used, especially in biochemistry and medical diagnostics.

In this work the different mentioned approaches have been used. Oligonucleotides chains (DNA) and antibodies have been detected first in label-free mode, then labels have been passively used to improve the results. The technique we developed actively exploits the labels, magnetic nanoparticles, to obtain a high quality result within a short interrogation time.

1.3.   Biosensing in integrated optics

Optical transducing technologies are now presented, with a brief overview on the most commonly used platforms and some data from literature. Optical sensors exploit light to translate a characteristic or a parameter of the world into a physical signal that is related to the concentration of the analyte under test.

There are several reasons to focus the attention on optical biosensors and in particular in integrated optics.

- The electromagnetic field of the light is affected by physical changes in the materials in which it is propagating. Not being sensitive to electromagnetic interference, the noise is mostly caused by the readout electronics.

- Depending on the waveguide shape, material, wavelength and excited mode (i.e. field distribution) the evanescent tail of the electromagnetic field reaches from few nm up to 1 µm distance, meaning that even large molecules can be detected.

- Conductivity of the buffer solution does not affect the measurement, reducing the sources of noise.

- Label-free techniques as well as label-based ones (both passive and active) are possible and already proven, like this work will show.

- Some of the optical technologies can be easily scaled up to mass production, reducing the cost per unit and possibly allowing a wide spread of the biosensing solution.

To perform the translation, optical sensors force the optical field to interact with an area where a molecular biorecognition is happening, and most of the time this have been

achieved with the evanescent field. Coming from the total internal reflection effect, the evanescent field magnitude can be described in a very general way by:

$$E(x) = E_0 \exp\left(-\frac{x}{d_p}\right) \tag{1.1}$$

where E_0 is the amplitude of the field at the interface between the guiding medium core and the cladding to be sensed, x is the distance from the core and d_p is the penetration depth, that indicates how much the field is expanding into the cladding and it depends on several parameters, e.g. angle of incidence of light and refractive indexes of the media. Several technologies have been developed to force the electromagnetic field in the biochemically active area, generating the evanescent field. Some of the most used ones are briefly presented now.

Optical fibers

Optical fiber, due to their simplicity and low cost, are still largely used in biosensing [48]. Although there are several approaches to use optical fibers sensors, they all rely on the evanescent field. In this case the penetration depth d_p (Figure 1.4a) is given by:

$$d_p = \frac{\lambda}{2\pi\sqrt{n_{co}^2 \sin^2\theta - n_{cl}^2}} \tag{1.2}$$

where λ is the wavelength form the light source, n_{co} and n_{cl} the refractive indexes of fiber core and cladding and θ the incident angle at the interface.

To increase d_p to enhance the sensing capabilities it is possible to modify the geometry and properties of the fiber. As in Figure 1.4b, optical fibers can be simply stripped from their original cladding or their cross section can be tapered to expand the optical mode into the environment. Fiber bends excite higher order modes that interact with the sensing medium and tapering fiber up to a tip end is useful to sense the medium in a specific point. In Figure 1.4c an example of tapered fiber for biosensing is shown.

The most common detection principles for optical fiber sensing are:

- output power change due to cladding refractive index modifications and evanescent field absorption: the optical power at the output strongly depends on how much light is absorbed by the medium and a strong contribution is given by the evanescent part;

- fluorescence detection: labelled assay in which fluorescent particles are bound to the analyte on the fiber surface, then evanescent field excites the fluorophores that emit

at specific wavelengths that can be detected by external devices. A second way to proceed is to attach functionalized fluorophores to the fiber and then measure the quenched emitted light as soon as the analyte binds;

- surface plasmon resonance fibers use the same concept from its peculiar technoloy, described later. In this case the field in the optical fiber is used to excite the plasmonic resonance.
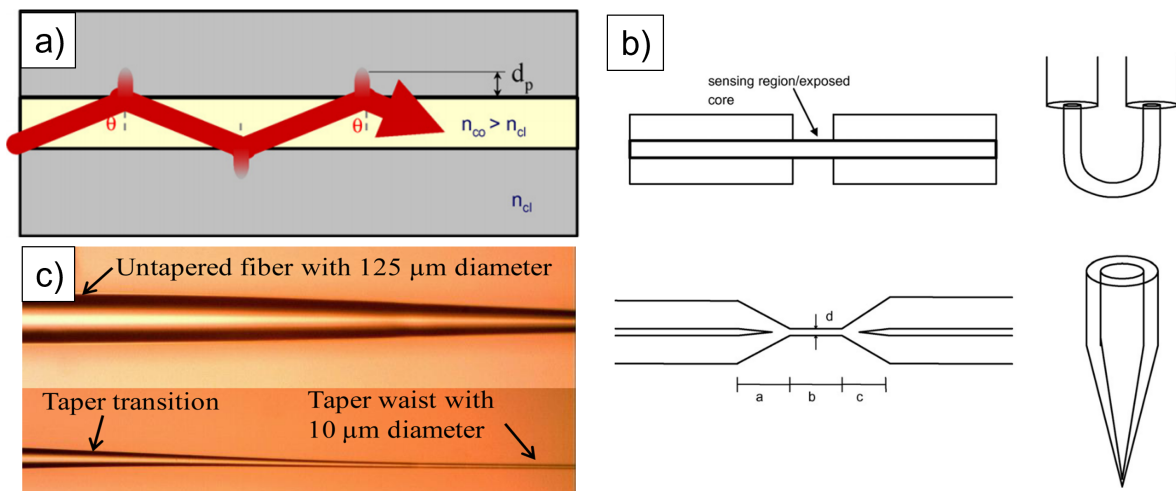

Figure 1.4: Optical fiber sensing: (**a**) evanescent field expanding into the cladding via total internal reflection. (**b**) Optical fibers configurations for sensing (from [48]). (**c**) Tapered fiber example (from [49]).

Devices like these proved great flexibility and reached detection limits down to $20\,\mathrm{fM}$ for IgG antibodies (tapered) [50] and $70\,\mathrm{fM}$ concentration for DNA detection [51]. Disadvantages of these technology approaches are the fact that they are difficult to scale for large production due to the non-integrated scheme, so they are still commonly used but competing platforms are closing the gap.

Surface plasmon resonance

Surface plasmon resonance (SPR) [52], is an oscillation of charge-density that happens at the interface between two media that present the dielectric constant of opposite sign, e.g. a metal, typically gold or silver, and a dielectric that could be air, water or a buffer. The charge oscillation is activated by incident light with proper polarization. This combination of ingredients causes the dielectric medium refractive index to change and that modifies the propagation constant of the surface plasmon. The resonance condition between the surface plasmons and the incident optical wave is thus altered. Being this effect strongly dependent on the refractive index of the dielectric medium, it is convenient to measure

the biochemical reactions happening on that surface, as in Figure 1.5.
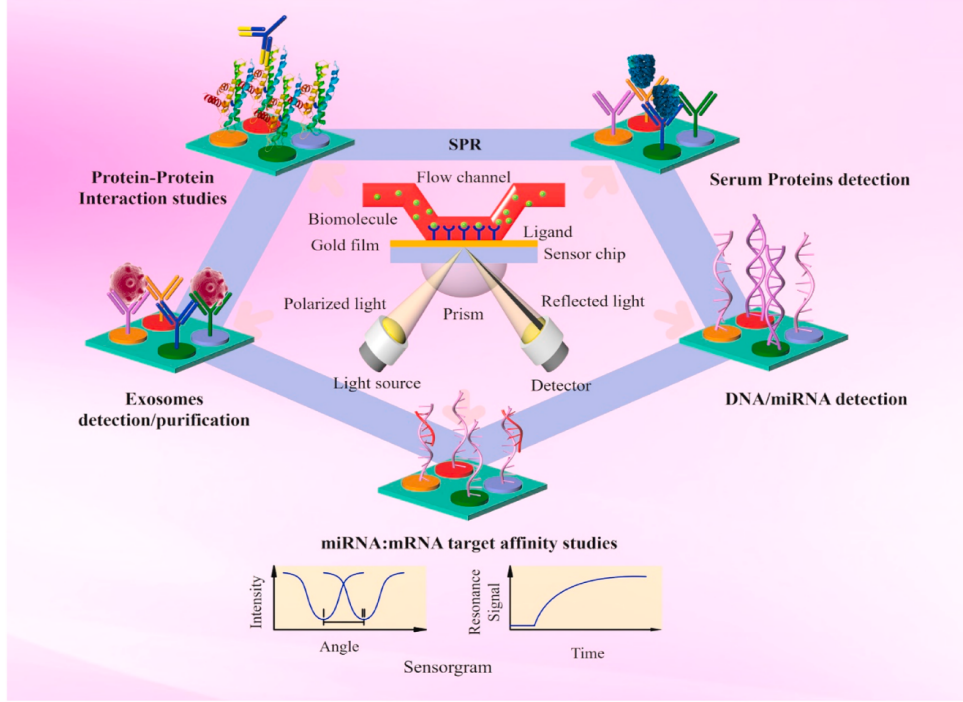

Figure 1.5: Surface plasmon resonance biosensor schematic diagram. Monitoring ability of the interactions between RNA, DNA, proteins and ligands. From [53].

Most of the SPR biosensors are in the prism-coupled configuration, in which a prism is used to couple light to the interface [54].
The reflection condition is given by:

$$\frac{2\pi}{\lambda} n_p \sin\theta = \frac{2\pi}{\lambda} \Re\left(\sqrt{\frac{\epsilon_m \epsilon_d}{\epsilon_m + \epsilon_d}}\right) \tag{1.3}$$

where the prism refractive index n_p and reflection angle θ are related to the real part of metal and dielectric medium dielectric constants ϵ_m ϵ_d. Thus the detection can be performed by monitoring the reflected light at wavelength λ, either in intensity or in angle, since the reflection angle θ will shift depending on the refrative index seen by the light, modified by the biomolecules.

This technique is largely used in biomedical applications since very interesting sensitivity values have been proved: LoD down to 1×10^{-7} RIU for bulk sensing and $1\,\mathrm{pg/mm^2}$ for surface sensing [55] have been proved also in commercial application, e.g. Spreeta from Texas Instruments (Dallas, TX, USA) [56, 57].
The difficulties in integration of such structures poses a limit in the costs and dimensions

reduction, precluding large adoption and relegating SPR systems in clinical laboratories. Recently, however, SPR concepts have been introduced in integrated fields, e.g. metal coating on optical fibers and waveguides to exploit the oscillating charges resonances, implementing a novel series of optical sensors that promise good performances in a scalable and reduced form factor [58, 59].

Interferometers

With the advances coming from quality improving in integrated chip foundries [60] and the knowledge in particular from telecommunication field, many devices once used just to manage signals are gaining attention for their use in sensing applications.

Interferometers are devices that compare the light propagation in two separate waveguides, one used as reference and the other for sensing, where the evanescent field interacts with the environment and the analyte. The comparison is performed thanks to interferometric schemes, that translates little propagation differences into power variations.

There are mainly two configurations of interferometers used in sensing: Mach-Zehnder (MZI) and Young Interferometers, shown in Figure 1.6.
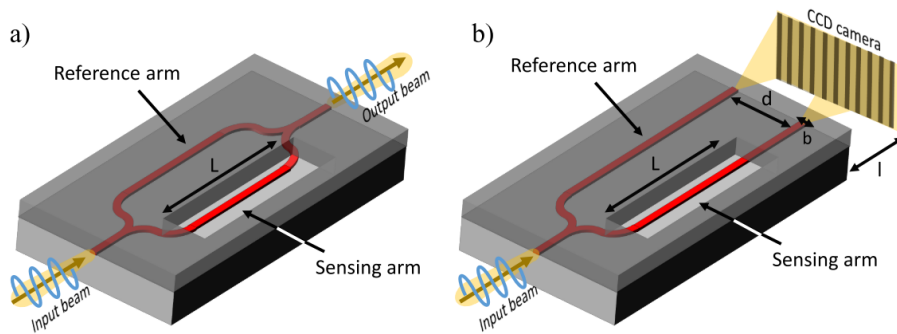
Figure 1.6: Interferometers working scheme. (**a**) MZI where intensity is probed after the arms recombination and (**b**) Young interferometer where the interference pattern is acquired by a CCD camera at a distance. From [61].

In MZI, the output intensity periodically oscillates as the phase shift between the two arms changes. An accurate measurement of the output intensity allow to calculate the phase shift occurred in the sensing arm and the refractive index change that caused it. Similarly, in Young's interferometer the two arms shine light on a further away surface and the interference pattern depends on the relative phase of the coherent sources.

Due to the easy integration of interferometers, many researches focus on the topic to develop a very compact and sensitive interferometer. Up to now for a MZI, bulk sensitivity showed results up to $20\,\mu m/RIU$ and $1 \times 10^{-7}\,RIU$ detection limit [62], while Young in-

terferometer with a CCD camera and performing a fast Fourier transform of the acquired image detected 9×10^{-9} RIU variation and down to $0.013\,\text{pg/mm}^2$ for IgG antibodies with protein G [63].

Resonating cavities

Resonating cavities based devices for sensing are showing great potential, mostly thanks to the small dimensions and possible integration that allow highly compact arrays devoted to sensing. In an optical cavity structure, the incident light brought by a waveguide or an optical fiber excites the whispering gallery modes or the circulating waveguide modes. The numerous round-trips completed by the light force, due to internal interference, to have a specific series of wavelengths that are allowed to live inside the cavity. The resonance condition can be written as:

$$\lambda = \frac{2\pi R n_{eff}}{m} \tag{1.4}$$

where λ is the wavelength that resonates, R the cavity radius, n_{eff} the effective refractive index seen by the electromagnetic field and m is an integer that indicates the order of the resonance.

Any disturbance caused by the environment causes the resonance to shift according to

$$\Delta\lambda_{res} = \frac{\Delta_{env} n_{eff} \lambda_{res}}{n_g} \tag{1.5}$$

where $\Delta_{env} n_{eff}$ is the effective refractive index shift induced by an environmental change and $n_g = n_{eff} - \lambda_0 \frac{dn_{eff}}{d\lambda}$ the group refractive index, that takes into account the waveguide chromatic dispersion. A deeper analysis on the sensitivity of resonating cavities is reported in Chapter 3.4.

Among all the parameters of a resonating cavity, worth to be mentioned are the Q-factor and the Free Spectral Range (FSR). Q-factor is defined as the number of electromagnetic oscillations inside the resonator before its power gets lost [64] and measures the sharpness, measured as full width at half maximum (FWHM), of a resonance relative to its central wavelength λ_{res}:

$$Q - factor = \frac{\lambda_{res}}{FWHM} \tag{1.6}$$

The FSR indicates the wavelength range between two consecutive resonances

$$FSR = \frac{\lambda^2}{n_g L} \tag{1.7}$$

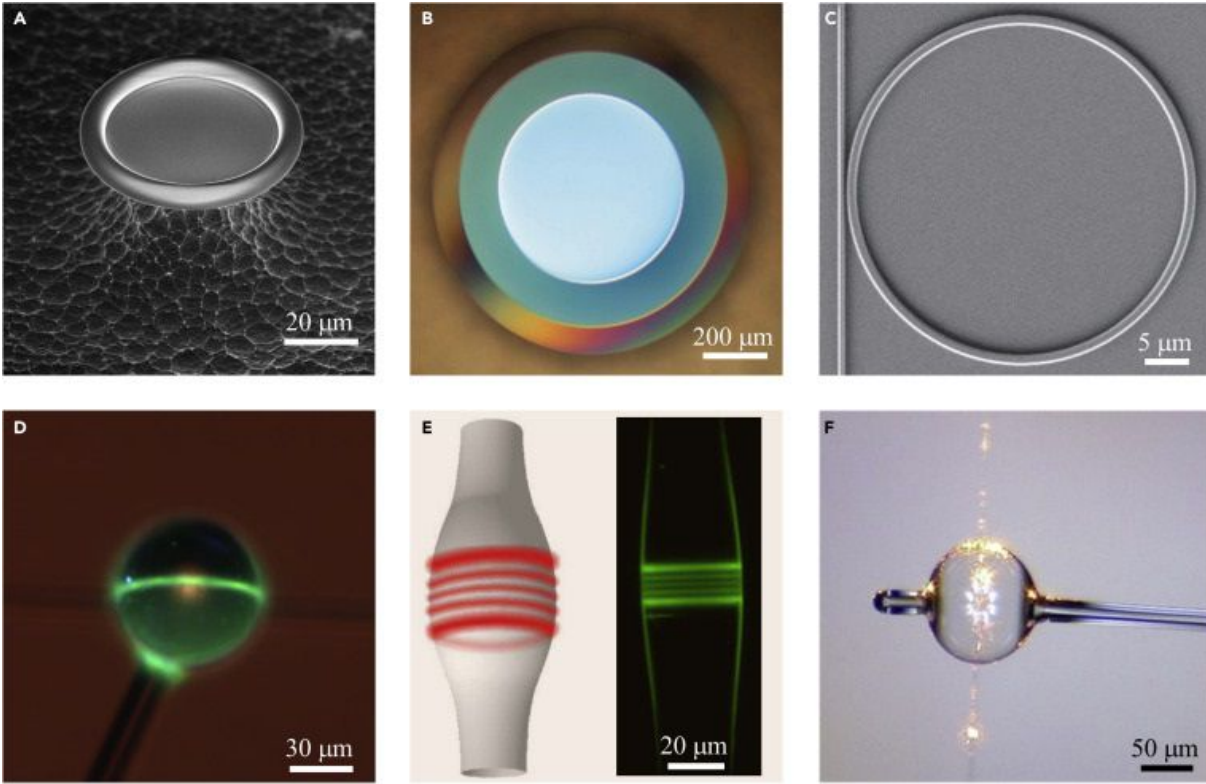where λ is the wavelength in between the two resonances and L the round trip length.

Figure 1.7: Examples of resonating microcavities geometries: (**a**) Microtoroid, (**b**) Microdisk, (**c**) Microring, (**d**) Microsphere, (**e**) Microbottle and (**f**) Microbubble. From [65].

Various shapes and versions of resonating cavities have been studied. As shown in Figure 1.7 some are chip-based, while others are free-standing microresonators. Common chip-based resonators are microrings, microdisks and microtoroid; free-standing structures are microspheres, microbottles and microbubbles. With optimized processing techniques like laser reflow process, some of these cavities possess surface roughness at atomic scale level, reaching Q-factor up to 10^{10} [66]. High Q-factor cavities can achieve very low concentration detection down to the single molecule, e.g. as demonstrated by [67] with small oligonucleotide chains. Limits of detection can reach interesting values of 1×10^{-6} RIU and sensitivity $850\,\mathrm{nm/RIU}$ and above [68]. In an interesting work, [69] realized and tested a frequency-locked detection method with a microtoroid able to detect fm-range wavelength shifts and single molecule binding.

However, suspended structures come with difficult fabrication and integration procedures. In this sense microring resonators (MRR) are more suitable for large scale production, in particular with CMOS compatible platform, e.g. silicon photonics. Existing in a large variety of configurations and interrogation methods, MRR are promising for implementing

highly sensitive biosensing devices, as it was proven by [70] that with Vernier-scheme cascaded MRR reached 24.300 nm/RIU in sensitivity, while [71] achieved a 912 nm/RIU bulk sensitivity with slot waveguide MRR. These structures are competitive thanks to their sensitivity and integration and commercial applications have already been on the market for few years, e.g. Maverik M1 from Genalyte [72–74].

1.4. Optical biosensors and magnetic nanoparticles

The optical biosensing is based on the detection of an absorption or a phase shift induced by the biochemical analyte on the sensor surface. On a photonic integrated chip (PIC), both label-free and labelled methods can be used, each with its own pros and cons: label-free approaches, in which the analytes are the only cause of sensor response change, allow to ease the sample preparation and the assay execution while labelling techniques offer sensitivity, selectivity and speed improvements.

Magnetic nanoparticles (MNP) offer interesting developments in the active labelling context [75]: the intrinsic magnetic properties allow to magnetically manipulate the labels and everything attached to them by applying properly designed magnetic fields, either permanent or time varying, as we will show in Chapter 3.
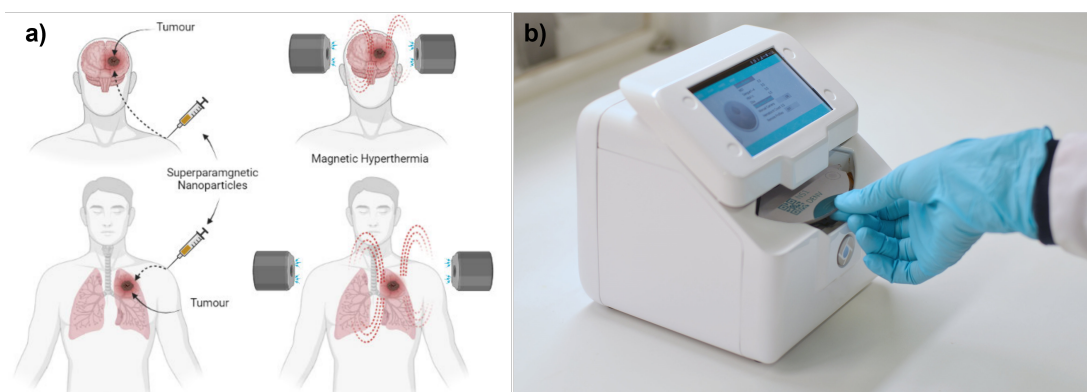
Figure 1.8: Magnetic particle applications. (**a**) Hyperthermia: MNP bound to the tumor and with the magnetic field heat the area killing the ill cells, from [76]. (**b**) BluBox from BluSense Diagnostics in operation: a drop of blood in the disposable cartridge is enough to have a quantification of virus or antibodies concentration in roughly 15 minutes.

Medical applications of MNP are certainly very important for life sciences and health improvements [77, 78].

Specifically labelling cells and biomolecules with MNP led to the development of in vitro applications of cell manipulation, DNA sequencing, biomolecule separation, selection and purification. A very important application performed in vivo exploits MNP to perturb the

magnetic field at a specific investigation site via magnetic resonance imaging (MRI) [79]. The cell contrast is highly altered, allowing to visualize specific portions of otherwise non-detectable objects. Drug targeting also took advantage of the manipulation properties of MNP, as they can transport drug and be directed to the desired location [80]. Well known are hyperthermia treatments, in which MNP are used to heat specific location of the body to kill cancer cells [81, 82], in Figure 1.8a.

More than heating a samples, stirring/separating biomolecules in solution, enhancing in vivo imaging and killing ill cells, MNP can be used to enhance the capabilities of existing biosensors or develop new sensing concepts.
External magnetic fields can be used to attract molecules labelled with MNP towards the sensor surface covered with probes [83, 84]. Another example is the use of MNP chains and external varying fields to dynamically modulate the light intensity in transmission optical biosensors, a solution that found its way to the market by BlueSense Diagnostics [85–88], in Figure 1.8b.

In surface-based sensors, great performances enhancement can be obtained by attracting MNP towards the sensing area, in Figure 1.9.
In SPR sensors, MNP attraction has been demonstrated with a strong improvement in sensitivity, up to four times, with respect the non-magnetic version [89–91].
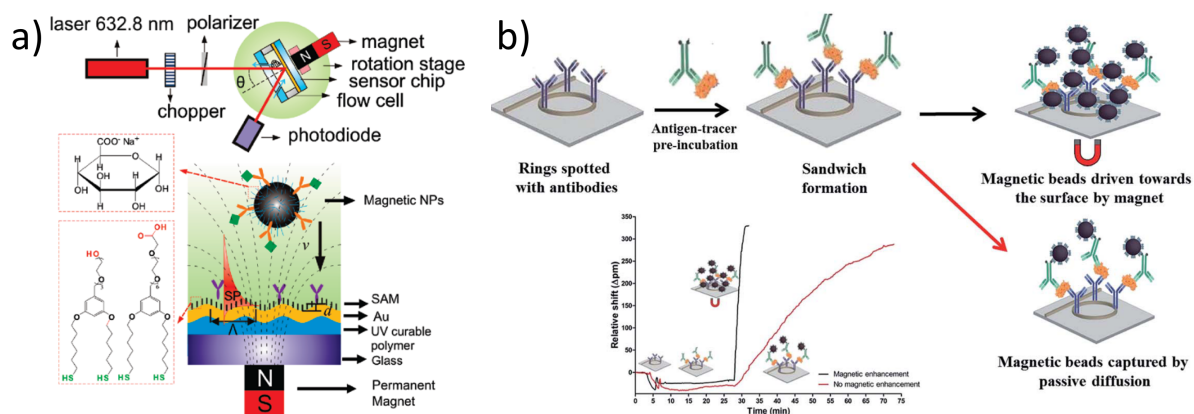
Figure 1.9: MNP assisted surface-based optical biosensing. (**a**) MNP enhanced SPR detection [90]; (**b**) MNP enhanced MRR detection [92].

Also MRR have been tested with magnetic particles attracted towards the waveguides and measurements showed that the binding step time was lowered by a factor of 11 and that the limit of detection lowered from 124 pg/mL down to 57 pg/mL [92].

In this work we show how MNP can be used on MRR as both passive and active labels with a new technique, here named opto-magnetic.

2 | Label-Free and Passive Labelling

2.1. Introduction

As described in the previous chapter, there are different approaches to perform biosensing. If we consider the time from when the biological sample is inserted in the system to the result visualization, the fastest scheme is the detection of molecular binding without markers, i.e. label-free. In this case the refractive index change is caused purely by the target molecules attaching to the probes fixed on the sensor. Because of the low impact of molecules on the RI, labels can be passively used to increase the effect, improving S/N ratio and LoD at the cost of a more complex sample preparation and a longer incubation time.

In this chapter we want to describe the photonic chip used for the tests and how the waveguides have been prepared to allow the sensing of the molecular binding. Then the experimental setup, the procedures and the results for both label-free and passive labelling will be shown. The test have been conducted twice: with a 60 base pairs DNA model for validation and with a peptide-antibody model meant to reproduce the immune response of the human body to Dengue virus. To conclude, we describe the diagnostic device prototype that have been designed, realized and tested in collaboration with regional project partners, with the aim of use it for a real testing campaign at the hospital laboratories.

2.2. Chip description

Silicon photonics (SiPh) is a nanotechnology branch that exploits the maturity, experience and know-how of the silicon complementary metal-oxide semiconductor (CMOS) fabrication and processing techniques to realize optical devices. Researchers in photonics and opto-electronics hope to achieve high yield, low costs and low time-to-market time without additional investments [93].

The chips used for the measurements in this Chapter and the next one are based on a Silicon On Insulator (SOI) platform. From a previous project, design and fabrication have been provided by STMicroelectronics srl (STm) which have been working for several years on SiPh platforms, mainly for datacom applications [94]. The acquired experience of STm on SOI led to choose a SiPh platform for the chips. Fabricated on a Multi-Project Wafer, the waveguide has a rib structure, as showed in Figure 2.1a, with 400 nm width, 160 nm rib height and 300 nm total height. Able to support both 1300 nm and 1550 nm wavelength in single mode, the waveguide does not support Transverse Magnetic mode (TM), which is leaky, while the Transverse Electric mode (TE) is able to propagate and its field distribution is plotted in Figure 2.1b. The large percentage of the field is confined in the silicon waveguide and just a little portion of it expands in the cladding above through the evanescent tails, making this structure a poor platform for biosensing. With
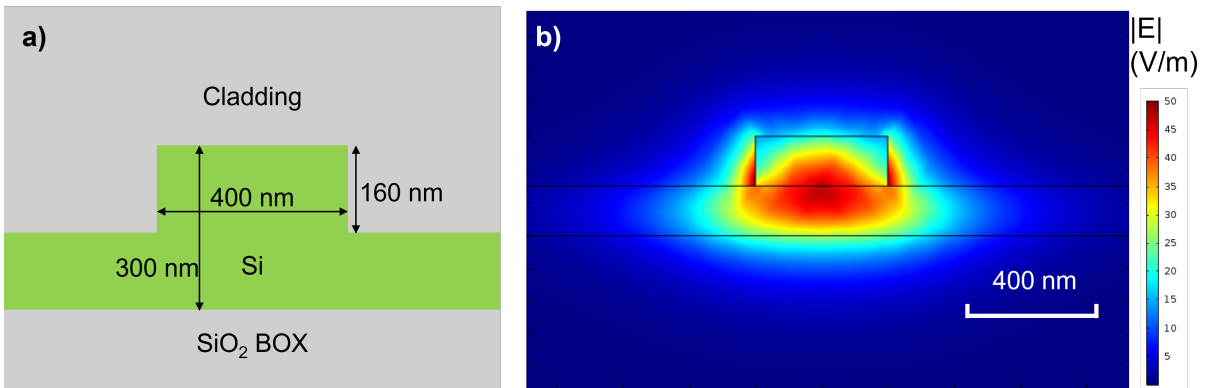
Figure 2.1: Silicon waveguide: (**a**) cross section of the guiding structure and (**b**) COMSOL simulation of the electric field distribution.

the exposed waveguide, the light propagation properties are affected by the environment and in particular by the refractive index of the medium above the sensing element. It is possible to verify this dependence defining a bulk sensitivity S_b of a ring resonator, usually measured in nm/RIU, as the wavelength shift per refractive index change of the cladding:

$$S_b = \frac{\Delta\lambda_{res}}{\Delta n_{clad}} \tag{2.1}$$

with λ_{res} the resonating wavelength and n_{clad} the gas or liquid refractive index. Simulating different refractive index materials over the completely exposed waveguide, we can estimate a bulk sensitivity of around $S_b =$40 nm/RIU. This is a poor result in integrated optical biosensing even when compared to other SiPh solutions. This effect is due mainly by two reasons: the high refractive index of silicon ($n_{Si} = 3.48$) with respect the cladding solutions (n_{sol} between 1.3 and 1.5) confines the EM field in the guiding structure and

the rib shape mostly forces it in the lower section, strongly reducing the evanescent field intensity in the sensing region. The advantage of this structure is the low propagation losses, usually below $1\,\mathrm{dB/cm}$.

The $5 \times 6\mathrm{mm}^2$ SiPh chip, in Figure 2.2a, features several MRR with a fixed diameter of $80\,\mu\mathrm{m}$ in add-drop configuration, as visible in Figure 2.2b.

The vertical row on the right side is formed by 4 all-optical MRR devoted to testing and first evaluations. The two horizontal rows contain 7 MRR each with integrated photodiodes (PD) at each output. The MRR are designed to present a quality factor Q ranging from 5000 to 65000. The light can be vertically coupled to the waveguide by means of grating couplers placed on the left side. To avoid alignment noise at the output and build a more reliable setup, the outputs of the MRR are terminated into integrated Germanium-on-Silicon photodiodes. The PDs are designed for telecom applications, showing a low-noise and a large bandwidth meant to recover fast signals. The dark current is measured to be below $1\,\mu\mathrm{A}$ and signal current from $1\,\mu\mathrm{A}$ to $100\,\mu\mathrm{A}$. Electrical pads are placed at the edges of the chip to access the PD signals via wire bonding.
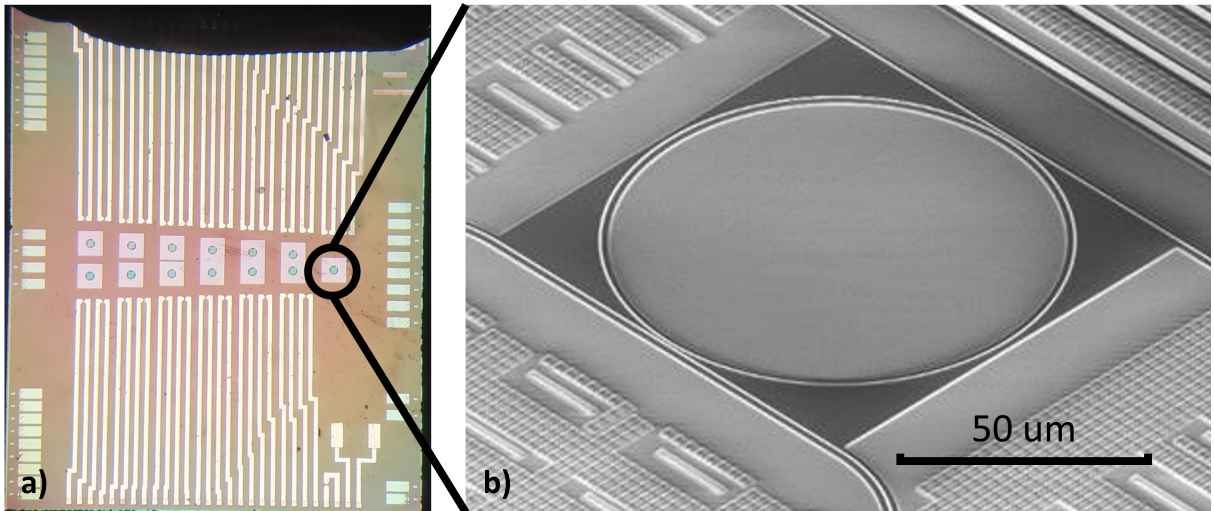
Figure 2.2: SiPh chip: (**a**) two rows of MRR in the center, grating couplers on the left, binding pad on the two shorter sides with electrical bonds protected by means of a drop of resin; (**b**) Image of the $40\,\mu\mathrm{m}$ radius MRR in add-drop configuration.

The MRR transfer function is plotted in Figure 2.3. From the spectrum it is possible to evaluate the free spectral range to be around $2.5\,\mathrm{nm}$ and, reversing Equation 1.7, the group refractive index is calculated to be $n_g =3.89$.
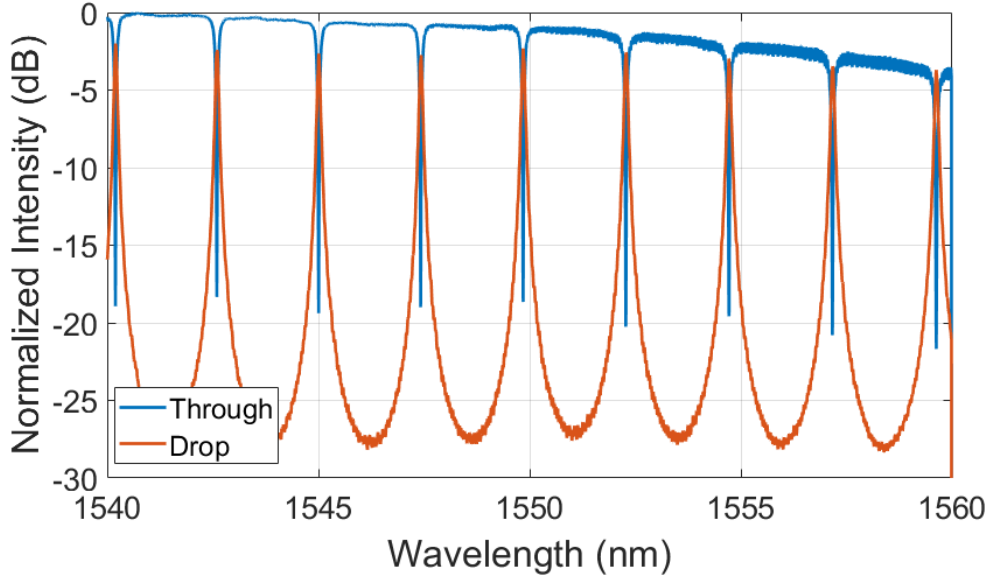
Figure 2.3: Through and drop output ports transfer functions: the FSR of the MRR results in roughly 2.5 nm

Waveguide exposure

The silicon layer from which the waveguides are built is buried under a multi-layered structure of silicon dioxide and silicon nitride layers forming the so called back end of line of the fabrication process [94]. The full stack measures a total thickness of 5.3 µm.

To expose the waveguides and allow the sensing area to be in contact with the environment, a custom recipe has been developed by my colleague F. Milesi. First a hard mask is fabricated on the chip surface, then a sequence of several dry and wet etching processes is performed to carefully remove the covering materials. The fabrication of the hard mask consists in spin-coating a layer of AZ5214E photoresist, to obtain a 1 µm thickness. Hardened photoresist islands above the MRR are obtained with a positive exposure lithography and then developing the sample in AZ726MIF developer. The metallic mask is created depositing a 150 nm thickness layer by sputtering Cr over the whole surface and then an acetone bath dissolves the photoresist freeing the apertures on the MRR areas in a lift-off process. With the hard mask protecting the surface, it is possible to proceed with the etching. For this job both dry and wet etching techniques are used. In particular, the dry Reactive Ion Etching (RIE) process have been optimized to remove the SiO_2 and SiN layers of the structure. It is a BOSCH-like process during which two gases are alternated inside the machine chamber. SF_6 gas is used for etching for 7 s and while C_4F_8 performs the side walls passivation for 5 s. Pumping steps of 5 s to remove the reactive agents are used in between the two gases steps to avoid contacts between
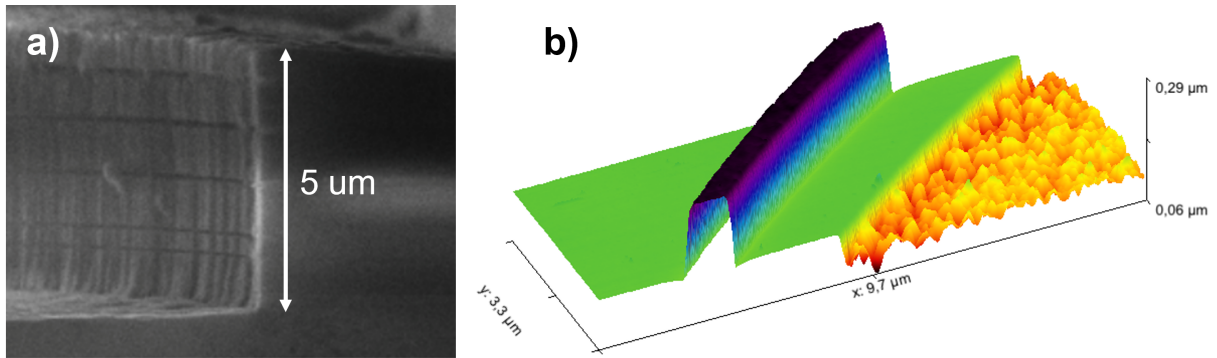
Figure 2.4: Etched surface to expose the waveguide: (**a**) Scanning Electron Microscope image of a profile during etching (credits: F. Milesi); (**b**) Atomic Force Microscope measure of an exposed rib waveguide (credits: N. Peserico).

SF_6 and C_4F_8, which mixture may have detrimental effects on the etching efficiency in terms of rate and profile quality. The loop is repeated until the back end of line above the silicon is removed, as visible in Figure 2.4a. Once the Si waveguide is reached, the wet etching process in Buffered Oxide Etchant is performed, removing the SiO_2 around the sidewalls and freeing the guiding structure, shown in Figure 2.4b. As last step, a chromium etchant solution dissolves the hard mask and the chip presents a flat and clean surface while the MRR are exposed thanks to a $\sim$5 μm deep, 100 μm diameter well. To conclude the fabrication process, the chip is glued and wire bonded to a custom PCB, presented in the Setup section. The wire bondings are then covered by a resin which provides protection from the functionalization process and the fluidic assembly.

The S_b value (Equation 2.1) strongly depends on the quality of the waveguide exposure process and it can be easily estimated by collecting the optical spectra of a MRR with different liquids with known refractive index deposited on the surface. Easily available liquids can be different concentrations of isopropyl alcohol or sodium chloride solutions in water [95, 96]. Their use allow to obtain a transfer function shift as shown in Figure 2.5.

2.3. Biochemical components

There can be different definitions of a "good" biosensor. In some cases it may be needed to detect very low concentrations of a very specific biochemical entity, or the measurements have to be done in a very short time, so a great effort should be put to optimize the desired result. While developing one aspect, e.g. speed, it may be an unrealistic expectation to obtain also very high performances in terms of sensitivity or selectivity. In our case, the first goal was to develop a system that was adaptable to a wide span of applications
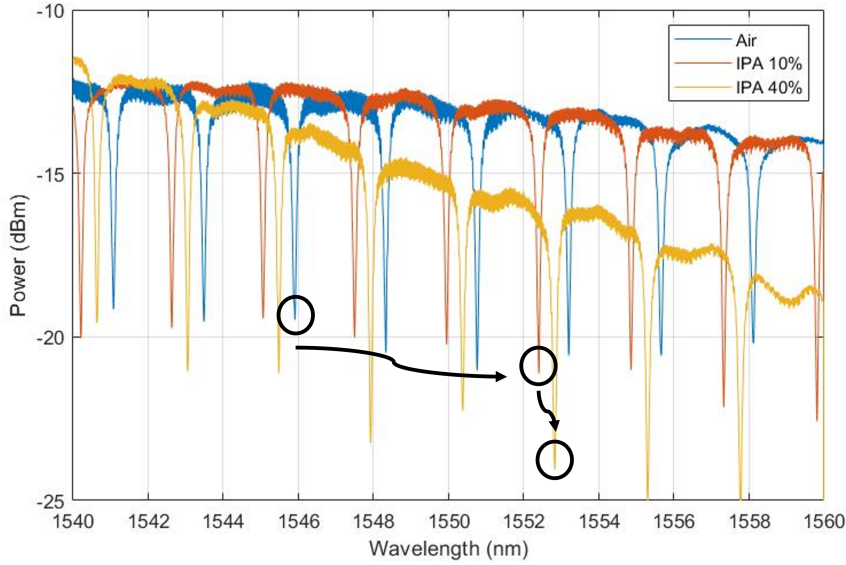
Figure 2.5: S_b measurement on an exposed MRR with air, 10% and 40% isopropyl alcohol solutions ($n_{air} = 1$, $n_{IPA10} = 1.3412$, $n_{IPA40} = 1.3622$ [95]) resulting in $S_b \simeq 20$ nm/RIU.

and then to optimize sensitivity and speed. A biosensor that can operate with a large variety of different molecules and corpuscles could be of great use in a clinical laboratory where different tests can be performed with a single tool. This means that the same device can detect proteins, oligonucleotides, cells or antibodies depending just on the functionalization and on the sample preparation but not on the technology.

As will be more clear in the following Sections and Chapters, our sensing technique exploits magnetic nanoparticles used as passive and active labels, so the big constrain is being able to perform a binding between the target we want to detect and the label. In order to develop our system we needed to test it on at least two different biological protocols. First, we started with a simple oligonucleotide model widely used for preliminary tests and validations and then we moved to a more clinically interesting antibodies system based on the human immunology response to Dengue virus infection.

The use of a copolymer is an effective solution that is being widely studied [97, 98], used at the beginning just over glass and silicon slides for fluorescent analysis, now finding application in different platforms [99, 100]. The process used to functionalize the chip is the coating with DMA-NAS-MAPS copolymer. This material, named MCP, offers several advantages when compared to other techniques. The MCP is suitable for oligonucleotides and for proteins, meaning that both molecule categories can be fixed on the coated surface, simplifying the preparation of the sensors if different tests have to be performed. The targets, proteins in particular, can be immobilized in the so-called native conforma-

tion in order to keep the biological function unaltered, improving efficiency and reducing false negatives responses. The copolymer offers a low unspecific background, crucial to avoid unwanted binding and adsorption that would result in false positive responses when dealing with complex samples containing a mixture of thousands of molecules.
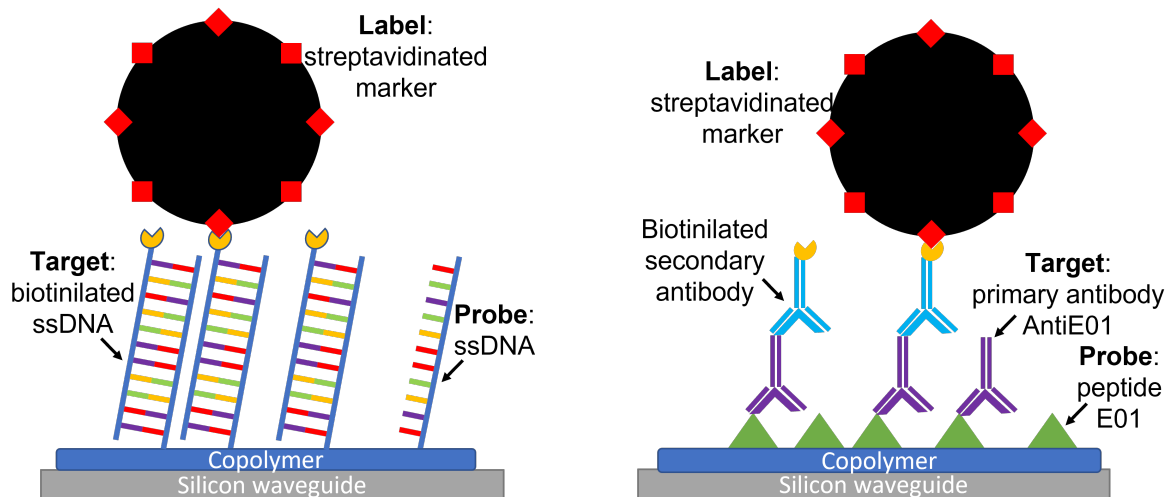

Figure 2.6: Biochemical components used in the hybridization protocols. The copolymer fixes the probe on the silicon. The target molecules then can bind. Subsequent binding steps, with secondary antibodies and/or label are used to increase the output signal.

The oligonucleotides model, from now on called DNA, is schematically shown in Figure 2.6a. The target that we want to detect is a 60 base pairs single strand oligo chain (60bp ssDNA). Artificially synthetized on demand, it brings at one end a biotin molecule that is used to enable an easy labelling thanks to the strong biological affinity between biotin and avidin-based complexes. To be detected, the ssDNA target need to be in close proximity of the sensing surface, i.e. the waveguide of the MRR. The wanted molecule is attracted to the desired position by the molecular probe, that hybridizes through binding. To obtain an efficient and specific molecular recognition, the probe should be biologically complementary to the target, so the natural choice is an oligonucleotide chain with the same length and a complementary sequence of bases. At one end of the strand, an amino group is attached to the sequence in order to be able to fix the probe on the copolymer that acts as functionalization layer above the silicon. The DNA sequences used are summarized in Table 2.1.

Aiming to test Dengue virus positive human samples, we used an antibody model to mimic the real situation. In this case, being unable to work on the target molecule to add biotine molecules, we used a double step hybridization, shown in Figure 2.6b. The probe is the Peptide E01, designed and then synthesized as described in [101]. E01 is a

	Weight (kDa)	Sequence
Probe	18	5′-NH$_2$- TCA TCG GTC AGG TGC AAC AAA TTG ATA AGC AAT GCT TTT TTG GCC CTA TCT TCT AAC AGC-3′
Target	18	5′-Biotin- GCT GTT AGA AGA TAG GGC CAA AAA AGC ATT GCT TAT CAA TTT GTT GCA CCT GAC CGA TGA-3′

Table 2.1: Sixty base DNA sequences as probe and target molecules and their molecular weights. A: adenine, C: cytosine, G: guanine, T: thymine.

peptide that has a similar antigenic behaviour to the Dengue virus envelope protein E, that covers the viral capside. The target, rabbit anti-E01 IgG antibody, was kindly provided by Primm (Milano). The secondary antibody that we used for model measurements is a biotinylated goat anti-rabbit IgG, while for the human model we used a biotinylated rabbit anti-human IgG. With the proper binding process, the system Peptide E01, target antibody and second antibody can be created. Then we can exploit the biotin molecule to bind the streptavidinated label.

Surface functionalization

The preparation of the coating and the functionalization of the chip with probe molecules have been performed at SCITEC-CNR laboratories. The two probe components, 60 bp ssDNA and Peptide E01, need a slightly different procedure to be deposited, so they will be treated separately.

To immobilize DNA on the surface the first step is a cleaning process of 15 min with O$_2$ plasma to remove residues, prepare the surface and make it hydrophilic. Then the chip is immersed for 30 min in a MCP-4 (Lucidant Polymers Inc., Sunnyvale CA, USA) solution, that is 1%w/v in water solution of ammonium sulfate kept at 20% saturation. A DI water rinse and N$_2$ dry step prepare the chip for a 15 min baking at 80 °C. Now the surface is fully covered by the copolymer and the probe molecules can be immobilized onto it as next step, Figure 2.7a. The probes are diluted to a concentration of 10 µM in the printing buffer, which is 150 mM sodium phosphate, pH 8.5, 0.01% sucrose monolaurate. The robotized spotter SciFLEX ARRAYER S12 by Scienion (Berlin, Germany) uses a piezoelectric dispenser to print the probes on the coated chip. As visible in Figure 2.7b, the molecules can be spotted in specific locations. For the experiments we decided to functionalize half

MRR, leaving the others with the copolymer coating but without the probe molecules. In this way the functionalized and non-functionalized MRR are completely comparable, with the first used as sensing elements and the latter as control or reference.

After the spotting process, the incubation lasts overnight and then the chip is immersed in a blocking solution (50 mM ethanolamine, 0.1 M Tris, pH 9.0) for 60 min to deactivate all residual active groups of the coating. The ssDNA sequences, shown in Table 2.1, were purchased by Metabion International AG.
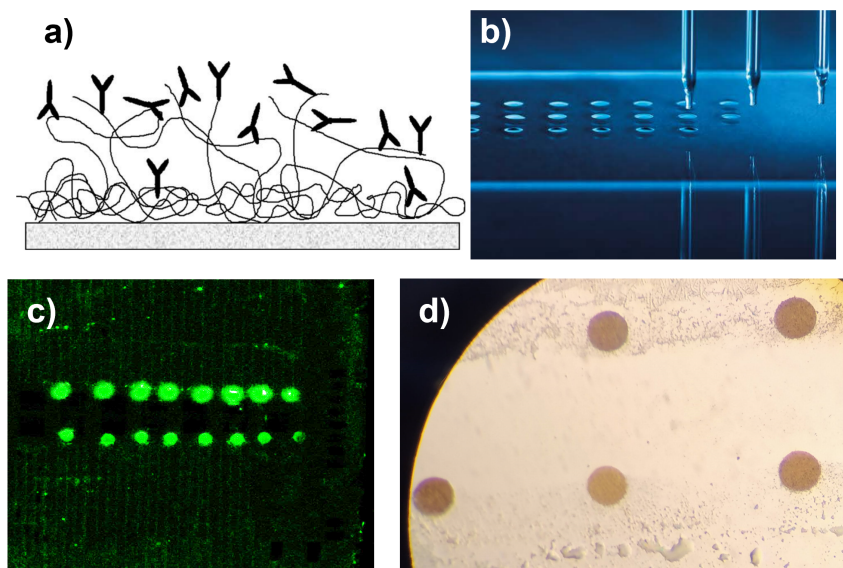
Figure 2.7: Functionalization of the sensor's surface: (**a**) copolymer representation [97], (**b**) spotter for probes deposition, from Scienion catalogue; (**c**) chip functionalised and then hybridised with fluorescent dye, (**d**) silicon slide functionalised and then hybridised with magnetic nanoparticles.

The Peptide E01 functionalization process is described in full details in [2]. Chip surface is pretreated with 15 min of O_2 plasma, then immersed in a 1%W/v solution of MCP-6 copolymer (Lucidant) having 0.8 M ammonium sulfate. The peptide E01 was diluted with a 15 mM sodium acetate buffer containing 25 mM trehalose to 100 µM. The composition of the spotting buffer has been optimized to be 1-1.8 ng/mm^2 [102]. After the overnight sitting, the blocking step was performed for 1 h in 2 mM EDTA solution and then DI water rinse and N_2 dry competed the functionalization process. The functionalization steps have been optimized both with fluorescent dye and magnetic nanoparticles, Figure 2.7c and 2.7d.

Hybridization process protocol

The hybridization protocol ensures that the biomolecular recognition can show a good efficiency rather than speed. The whole process take place in a fluidic cell, and the flux is controlled by a programmable syringe pump.

The target DNA is diluted at several concentrations in saline sodium citrate solution (SSC), which is also used as washing buffer. The labels are magnetic nanoparticles (MNP), more details in the next chapter, and are diluted in a Phosphate Buffered Saline solution (PBS).
The solutions are listed in Table 2.2

Solution	Components
Washing	2xSSC
PBS	1xPBS
DNA	target ssDNA in 2xSSC, concentrations from $10\,\text{pM}$ to $1\,\text{µM}$
MNP	streptavidin-coated MNP in PBS, $\sim 10^{11}$ particles/mL

Table 2.2: Solutions used for the hybridization.

The solutions are preloaded in the fluidic system tube and the sequence of fluids that arrive on the chip surface is reported in Table 2.3. Washing and buffer steps are also used to create a baseline for better evaluation of the MRR resonance shift. To avoid target or MNP depletion in the sample long pauses are avoided preferring to keep a continuous flow or emulating some periodical mixing by fluxing for a minute between small resting steps.
From start to finish the overall time can easily be above the 2 hours limit: depending on the measurement requirements this time can be reduced by cutting the time for each step.

2.4. Experimental setup

The tests were conducted in a lab-on-chip platform meant to perform sequentially the molecular recognition and the active labelling measurements, described in the next Chapter. To reduce efficiency losses in the biomolecular hybridization, lower optical alignment issues and improve the repeatability of the tests, the platform we designed is an assemble of modular building blocks that are securely and tightly connected together to perform the measurements as needed.

Step	Solution	Repetitions	Volume/Repetition	Flow	Step Pause
			μL	μL/min	min
1	Wash	1	>500	100	
2	DNA	1	200	100	
3	DNA	1	300	20	>5
4	Wash	1	300	100	>5
5	PBS	1	300	100	>5
6	MNP	1	200	100	
7	MNP	4	25	20	>4
8	PBS	1	>500	20	
				Total time:	>100 min

Table 2.3: Hybridization protocol

Reach high reliability of the system is fundamental for several reasons. First, the hybridization processes can last from few minutes to several hours. With the scanning technique described in the next section, we need to compare the chip response between different moments and noise sources cause the information to be disturbed or, in case of low signals, completely unreadable. Second, early stage development of sensing and diagnostic tools such the one under test need to produce a calibration curve, which shows the output signal depending on the concentration of the analyte. To obtain the curve, a large set of measurements have to be performed and these tests must be in the same environmental conditions to avoid systematic errors in the outcome.

The setup used for the hybridization is schematically showed in Figure 2.8 and it is the evolution of the one used by N. Peserico in his works. It fits on a laboratory bench and is partially manually operated and partially automatized for repeatability and convenience. The electromagnetic radiation is generated by a diode laser, which we can modulate by controlling its temperature and current to obtain the desired lasing wavelength at the output. The light is guided by a single mode fiber (SMF) to a polarization rotator before getting splitted into four different channels to have the possibility to simultaneously monitor multiple sensors. Then a custom 8-channel glass fiber array is used to couple the SMF to the grating couplers of the chip. The correct micrometer precision alignment is obtained with a 3-axis micropositioner on which a custom 3D-printed support holds the fiber array.

The chip, described before, is mounted, glued and wire bonded to the custom PCB, named
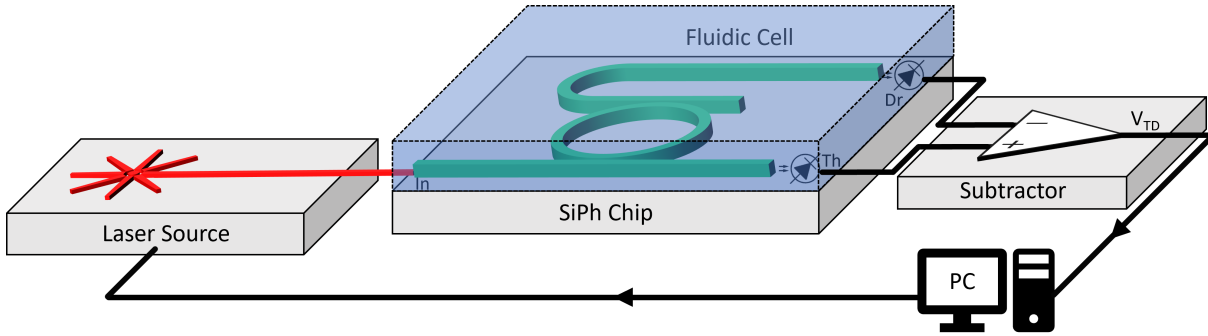
Figure 2.8: Schematic of the experimental setup used for hybridization measurements. The PC drives the laser that scans the wavelength. The chip with MRR is in contact with the sample fluid thanks to the fluidic cell. The PD intensities are collected and analysed by the PC.

photonic board. The fluidic cell is also fixed on the photonic board to control the liquid to be sampled. The PDs at the MRR output collect light and current signals are brought by a flex cable to the processing electronics. The electronic board, designed and fabricated by Elite srl, contains four 2-channels trans-impedance amplifiers that convert the currents to voltage signals. Another functionality of the electronic board is a feedback system to accurately track the MRR resonance shift. Then the data acquisition PC interface acquires the voltages and the data analysis script extracts the resonating wavelength over time.

Laser

Scanning detection methods are usually performed with expensive tunable sources for bench-top applications, but to reduce costs and move towards an efficient implementation we used a more common laser for telecom application. The source is a distributed feedback (DFB) laser from JDS Uniphase in butterfly package, Figure 2.9a. The central wavelength of this model is around 1560 nm, with a linewidth around 700 kHz ($\simeq$5 fm), more than optimal for our application.

To perform the wavelength scan over at least a free spectral range of a MRR, we controlled temperature and current of the diode. The tunability characterization results are in Figure 2.9b and 2.9c: one parameter has been fixed and the other was changed to measure the emission wavelength change. From the calculations the temperature tuning coefficient resulted $c_T \simeq 93$ pm/K and the current tuning coefficient $c_C \simeq 1.3$ pm/mA. These results indicate that we have different available tuning methods, each one with its own peculiarities.
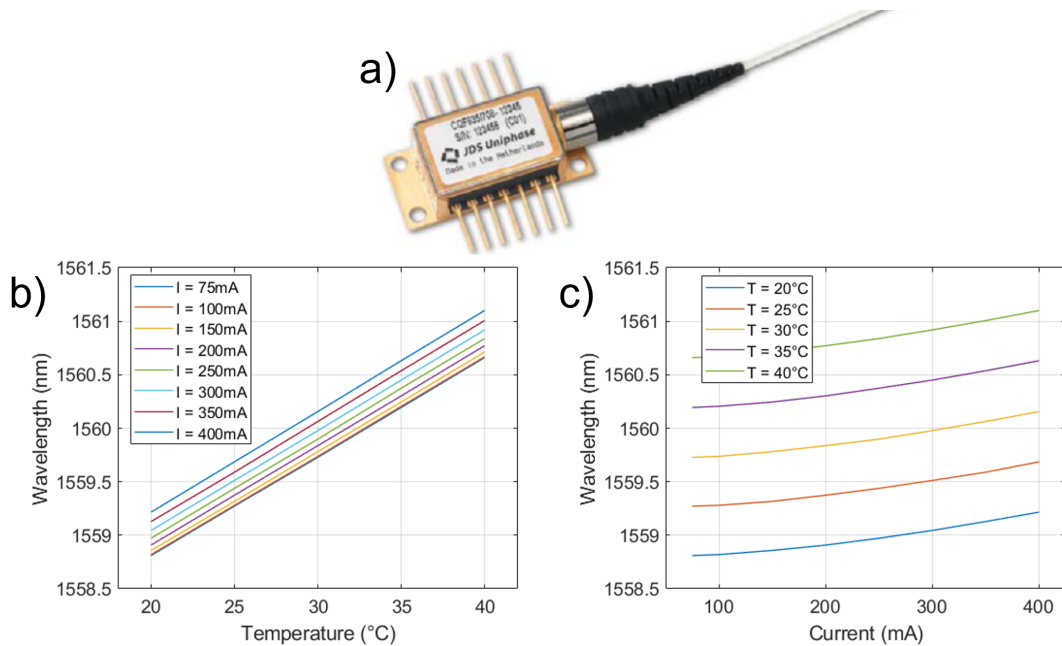
Figure 2.9: JDS Uniphase laser: (**a**) picture of the butterfly DFB laser, rated for 1560 nm emission wavelength; (**b**) characterization of the temperature wavelength tunability and (**c**) characterization of the current wavelength tunability.

The temperature is driven by a termo-electric cooler and an in-package Peltier cell and in tests we pushed it up to a maximum of 100 pm/s ($\sim$1 K/s), therefore it is a slow way to modulate the wavelenth. These type of telecom lasers are meant to work at a fixed temperature, but they are tested for wide temperature ranges [103, 104], and so it is possible to slowly scan the lasing spectrum up to few nanometers range. In our case we covered the full MRR FSR linearly modifying the temperature between 15 °C and 45 °C over a 90 s periods.

The second tuning parameter is the diode current. Between the threshold current (I_{th} =75 mA) and the maximal rated one (I_{max} =400 mA) we have a $\sim$400 pm range. The current driver can perform current modulation by external signal, with a conversion coefficient of 20 mA/V. With respect the temperature tunability, this approach has a limited range, but offers a faster way to shift the lasing wavelength. Tests with direct sinusoidal modulation up to 1 kHz frequency showed a consistent diode response.

Photonic board and fluidics

The photonic board in Figure 2.10a has been designed with a multiple purpose. The PDs on the SiPh chip are electric active elements, therefore they must be connected to a suited electronics to properly work. Electrical pads are presents on the photonic board

to wire bond the chip and transport the current signals coming from the PDs placed at the through and drop outputs of the MRR. Then, to put in contact the sensing area of
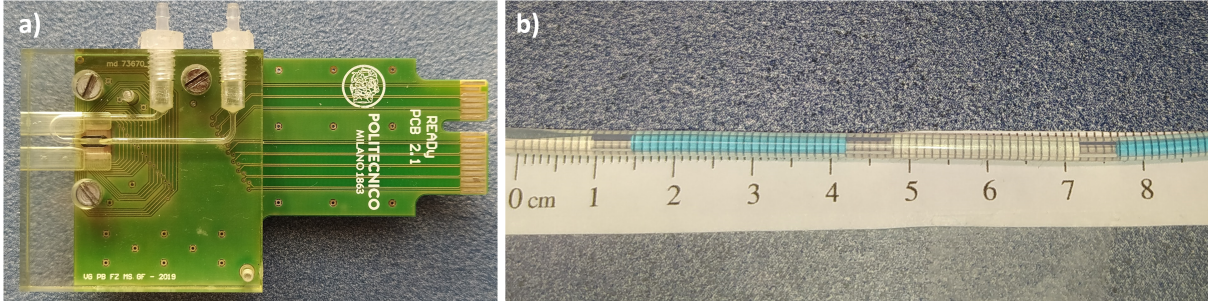
Figure 2.10: Fluidics on the chip. (**a**) Photonic board with SiPh chip and fluidic cell. (**b**) All the needed solutions are loaded into the silicone tube: to avoid mixing a small air bubble is inserted as interface.

the chip's surface with the liquid to be tested, a fluidic cell is mounted and fixed on the photonic board.

The fluidic cell, designed by HTA srl, is made of PMMA and contains a 1×1 mm^2 channel that allows the analyte to flux on the $\sim 1 \times 4$ mm^2 sensing area of the chip. A silicone O-ring seals the contact area and guarantees that there are no liquids leaking or air bubbles entering inside the channel. Two rectangular slits are milled on the side to let the fiber array to reach the chip and couple the light into the grating couplers.

The two tube fittings connect the cell to the fluidic system. On one side a short tube is connected to the syringe pump AL-1000 from WPI Ltd with a 15 mL volume syringe manually operated in aspiration mode for flux control. The other end of the channel is connected to a 1.5 mm inner diameter and 1 m long silicone tube used to preload all the solutions needed to execute the protocol. As in Figure 2.10b, the solutions are loaded sequentially into the tube, inserting a 5 mm ($\simeq$10 µL) air bubble between each other to avoid mixing.

Feedback resonance tracking

The electronic board from Elite srl (Figure 2.11a) is equipped with a series of devices that allow to perform a resonance shift tracking with femtometer precision developed during a past project with STm [8]. The basic principle is to lock the laser wavelength at the crossing point between Through and Drop transfer functions: follow this crossing position allows to accurately follow the resonance shifts.

The conceptual scheme of the working principle is reported in Figure 2.11b. The board collects the voltages at Through and Drop outputs of a MRR and computes the difference
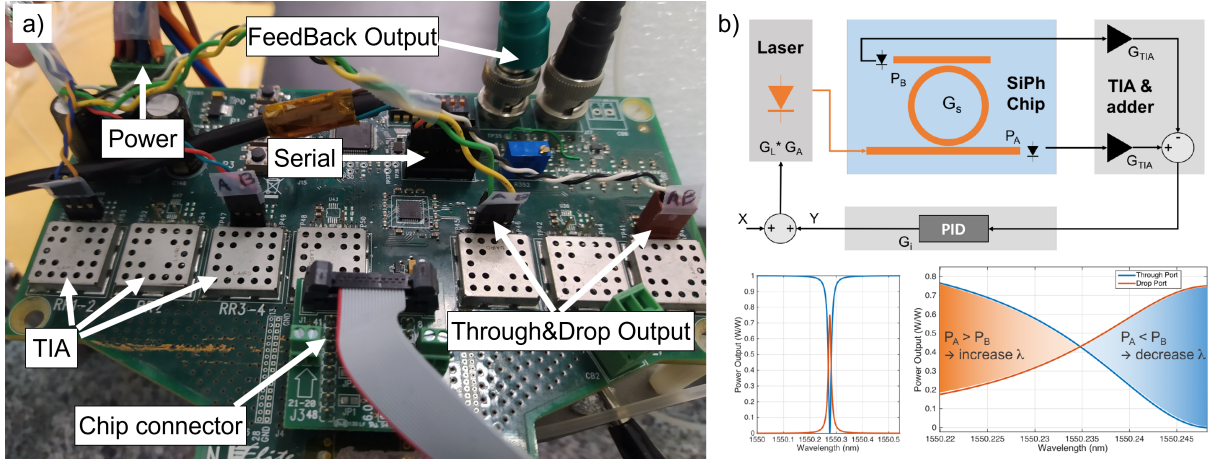
Figure 2.11: Electronic board and feedback loop. (**a**) The Elite electronic board with the required connections. (**b**) The feedback loop tracks the resonance position by fixing the laser wavelength at the Through - Drop crossing point, from [8].

thanks to a 16-bit analog-to-digital converter and a microprocessor.

The difference value is processed by a proportional-integrative-derivative (PID) controller and the recalculated error signal is used by the current driver of the laser to adjust the wavelength thanks to the current tunability. Knowing c_C it is possible to accurately track small and fast shifts in MRR resonance by simply looking at the feedback signal.

The wavelength measurement performed with this platform allow to see fast event up to 1 kHz and with a femtometer precision as can be seen from the raw data reported in Figure 2.12. The system has been used to measure refractive index differences between several fluids, with the aim to perform high precision hybridization measurements, towards the single-molecule detection, thanks to a fast noise standard deviation of $\sigma_{feedback} \simeq 20$ fm.

However, the imperfections in the etched waveguides decreased the quality of the MRR. Plus, the biological solutions fluxing on the surface with the metallic MNP binding to the sensing area act as increased waveguide roughness, leading to more electromagnetic scattering and causing the Drop transfer function's peak to decrease: as resulting effect, the crossing point gets easily lost. Without a crossing point the feedback system stops working and it often happened to loose the Drop signal mainly due to MNP interacting with the directional couplers. Some techniques have been employed to force the two transfer functions to cross but since the gain of the loop was not constant, being dependent on the slope at the crossing, they caused the feedback to behave unreliably.

A second issue is the widen of the resonance notch that happens at high molecular concentrations (example in next Section, in Figure 2.13). Since the feedback system follows the crossing point, it may results in a perceived resonance wavelength shift while in real-
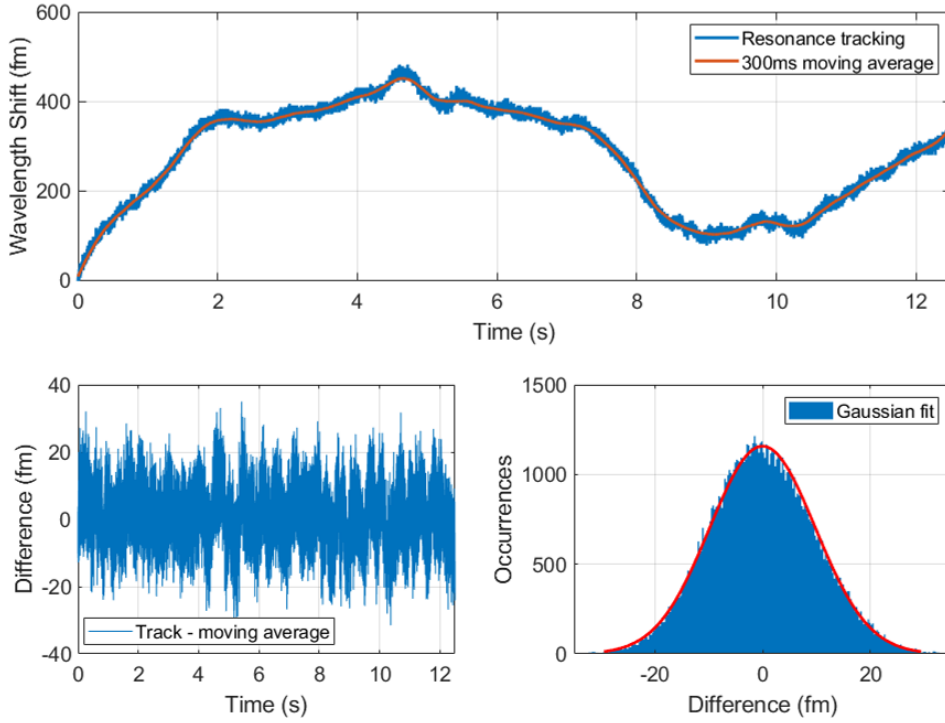
Figure 2.12: Resonance tracking with feedback loop. Fast shifts can be easily noticed and the noise has a standard deviation that ranges from 15 fm and 40 fm.

ity it is just a Q-factor decrease. Being this effect prevalent at medium to high analyte concentrations, we believe that it could be a negligible issue for low concentrations measurements.

With those issues putting at risk the good outcome of the tests and knowing the potential of the feedback technique, we decided to use this technology only in few occasions, leaving new developments for the future.

2.5. Molecular binding measurements

The molecular recognition, process that binds together complementary molecules, causes a modification in the mass concentration in the near proximity of the waveguide, which is our sensing element. The increased material on the MRR causes the refractive index of that area to slightly change, affecting the effective refractive index n_{eff} perceived by the electromagnetic field resonating in the cavity. The resonance condition is thus modified in the MRR and the resonating wavelength shifts according to

$$\frac{\Delta\lambda_{res}}{\lambda_{res}} = \frac{\Delta n_{eff}}{n_g} \tag{2.2}$$

This resonance shift could be measured in different ways, the classical being scanning the transfer function with a bench-top tunable laser. With the aim of reducing complexity and costs while assuring a reliable measurement, we decided to use a classical laser for telecom applications and shift its lasing wavelength over a MRR FSR as already described. The PD signals are collected after the TIA in differential configuration: collecting $V_{TD} = V_{Through} - V_{Drop}$ instead of just one of them allow us to be more resilient in case of a photodiode malfunction or an unstable Drop coupler; plus, V_{TD} presents a deeper notch, easier to fit when noise raises.

During the molecular recognition process the transfer functions are collected and an example is visible in Figure 2.13. As time passes and molecules bind, the resonance changes its position, quantifying the analyte concentration. Two facts are worth noticing: a change in cavity finesse in particular as the MNP start binding to the system, meaning that the metallic particles are perturbing the electromagnetic field like defects on the waveguide, and that the crossing point gets lost (i.e. V_{TD} does not reach 0V) when the quality of the cavity reduces.
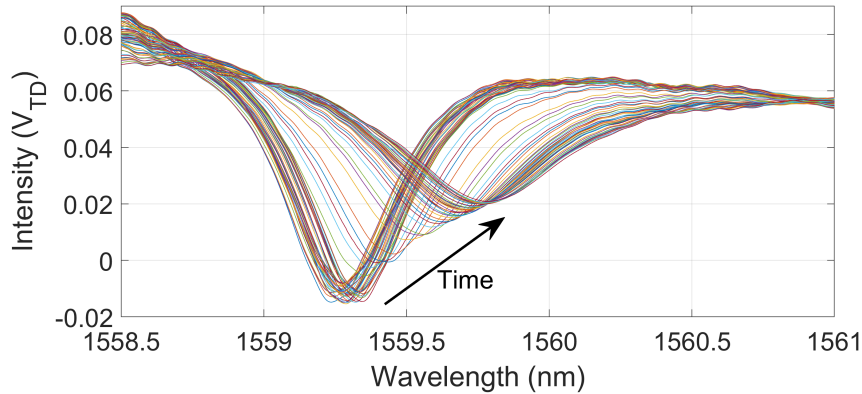
Figure 2.13: All the scans acquired for the 100 nM DNA hybridization. Resonance position and Q-factor are strongly affected by the labels.

Since the biomolecular effect would be worthless if not compared to a reference sensor, for every sensing MRR with the probe spotted surface, a nearby control unspotted MRR is tracked simultaneously. As explained in the surface functionalization section, the non-functionalized MRR are covered just by the copolymer so they are still affected by the refractive index of the fluids and by the aspecific binding, but not by the specific one, thus they are perfect to be used as reference sensors.

To recover the central wavelength, all the curves are fitted to a Lorentzian model that returns the correct position of the MRR resonance. Then the sensing and reference shifts

are compared to evaluate the net contribution caused by the target molecules and the MNP. These results are plotted in Figure 2.14, that shows an example of resonance shift over time. The first step, the label-free hybridization, is when the ssDNA becomes a
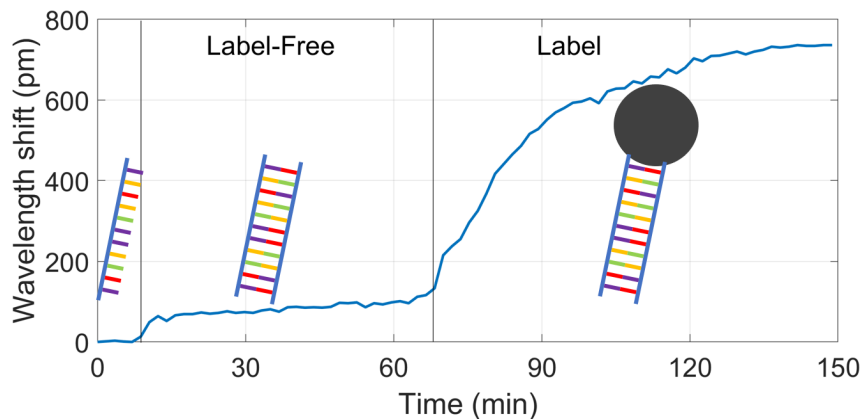
Figure 2.14: DNA hybridization curve at $100\,$nM concentration. The label-free approach is fast but it may be covered by noise. Labelling results in an increased signal.

dsDNA: it is a fast process but the shift is rather weak and the noise could hide it at lower concentrations. After $10\,$min the first hybridization is almost completed, but longer times were used to be consistent with lower concentrations measurements. After $30\,$min from the start the surface is gently washed to be cleared from unbound DNA.

The second step is the passive labelling. First some buffer solution is used to have a flat starting level and then the MNP solution is inserted in the cell. The labels binding, efficient thanks to the biotin-streptavidin high affinity, generates a shift increase by ten times due to the large impact of the MNP to the evanescent field. After other $60\,$min the buffer solution is used to remove unbound MNP.

The whole solutions sequence, exiting the fluidic cell, enters the aspirating syringe where it mixes and then treated as waste. In future, the use of different fluidic systems will keep the fluids separated in order to perform new sequential measurements.

Hybridization measurements are repeated for a large span of possible target molecule concentrations: in our case from $1\,$µM we decreased down to $10\,$pM, with one test for each decade of concentration. For each concentration the sensing and reference shifts are extracted and compared. Having just one measure per target concentration, the uncertainty over the retrieved shifts has been calculated acquiring $5\,$min of plateau data before and after the hybridization and evaluating the quadratic sum of the standard deviation of the considered plateaus. The values of the shifts with error bars are plotted in Figure 2.15, representing the calibration curve for molecular recognition measurement with our system.
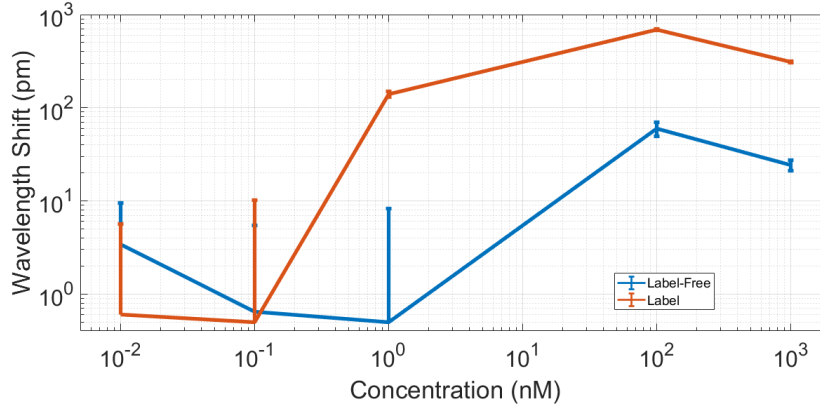
Figure 2.15: DNA calibration curve. Labelled measurements are 10 times better than label-free ones. At low concentrations both are noise-limited.

The acquisition method, spanning a DFB laser by means of its temperature and fitting the collected data to a lorentzian curve, is the simplest way to collect the shift informations. This simplicity comes at cost of noise: error in shift detection goes from 5 pm to 10 pm, and in cases of mechanical instabilities, excessive thermal fluctuations, non-homogeneus refractive index of the liquid this value can easily rise. The calibration curve in Figure 2.15 shows that with our conditions (i.e. chip, setup, microfluidic efficiency, ...) we can expect to be able to detect between $1 - 100$nM of DNA in label-free approach, concentration limit that reaches a range between $0.1 - 1$nM in case of labelling the biomolecules with MNP. In general, the labelling led to a signal enhancement by at least an order of magnitude.

Similar results have been obtained with a set of measurements on a more complex protocol involving the Peptide E01 as probe, rabbit anti-E01 IgG antibody as target, biotinylated goat anti-rabbit IgG as secondary antibody and MNP. The results are reported in Appendix A.

A better estimation of the performances of this biosensor can be obtained evaluating the Limit of Detection, obtainable considering the error in the refractive index measurement $\sigma_{n_{eff}}$ and applying Equation 2.2:

$$LoD = 3\sigma_{n_{eff}} = 3\frac{n_g}{\lambda_{res}}\sigma_\lambda. \tag{2.3}$$

Thus, considering that the measurement produces an error in the extracted resonating wavelength $\sigma_\lambda \sim 10$ pm we obtain $LoD \sim 7.5 \times 10^{-5}$ RIU.

This value does not compete with other techniques in terms of LoD, but it is proof that the system is working and that this scanning method with relatively cheap elements can

be implemented in out of the bench devices, paving the development and realization of diagnostic tools with integrated optics platforms at a reasonable quality/price ratio.

2.6.   Diagnostic semiautomatic device

Thanks to the results obtained with the experimental bench and the gained experience during the design and optimization of the system, in close collaboration with our partners in the regional project Ready we designed, realized and tested a diagnostic device. The apparatus is meant to be used in clinics and hospital laboratories, helping to perform analysis to detect and measure proteins and antibodies concentrations in human plasma samples.

The Ready project consortium, composed by many research and industrial partners from Lombardia region, was created to match the discovery, the development and the production of bioreagents with analytical kits and platforms, in order to provide a reliable check regarding the diffusion of infections caused by pathogens such Trypanosoma cruzi, Plasmodium spp, Schistosoma spp, Dengue virus, Chikungunya virus and Zika virus. Having a fast and correct estimation of tropical diseases diffusion will help to provide better health care, limit the diffusion rate and avoid them to become endemic.

The project saw our groups of Dipartimento di Fisica and Dipartimento di Elettronica, Informazione e Bioingegneria from Politecnico di Milano dedicated to the study and implementation of the sensing technology, HTA srl to the assembly of the device, SCITEC-CNR to the chip functionalization and target development and DiaPro srl with Sacco Hospital to the human plasma sample collection.

Figure 2.16: READY project partners that collaborated in the development, realization and testing of the diagnostic machine.

The device to be designed, had to be usable to non-expert user, automatic for the most

part of the operations and with a grafic user interface.

HTA srl, with its experience in producing and commercializing gas-chromatography devices, realized the mechanical assembly, the fluidic system and the software to manage the machine. On our side we transferred our knowledge providing the photonic microchips, the electronics to read and acquire the signals, the algorithm to process the data and the experience on similar measurements to test the device.

The programmable fluidic system is helpful in simplifying the operator's task. Up to 7 of all the required fluids, e.g. primary target, labels, washing and solutions are placed in the vials on the trail accessible by the user. A series of 7 electrostatic valves can be controlled to open or close the various tubes attached to the vials. Then a star manifold connects all the single-fluid tubes to the main pipe. The length of the pipe was chosen to preload all the needed solutions in the correct order as requested by the hybridization protocol that depends on the sample under test and on the biomolecules to detect. The syringe pump can fill up, aspirating the fluid sequence that fluxes through the fluidic cell wetting the chip surface. When the syringe is full, the directional valve changes its state and the syringe empties its content into a waste vial. The processes are fully automatic and programmable: the open/close valves combinations, the syringe that can move in either directions with a wide range of flux rate from $20\,\mu\text{L/min}$ to $2000\,\mu\text{L/min}$, the timed pauses and the steps to be repeated. The possibility to program many protocols, along with calibration and washing procedures is a huge advantage in terms of usability. For more temporary tasks, a manual mode is present.

The optical source is a DFB laser diode from LasersCom operating at $1550\,\text{nm}$ for telecom applications. The current and temperature driver is the CLD1015, with serial port for PC communication. The light is first corrected in polarization and then splitted into four channels. The fiber array for vertical coupling is mounted on a custom 3D printed holder on a 3-axis electro-mechanical micropositioner from Newport.

The laser wavelength scan is performed gradually changing its working temperature in order to cover at least one MRR FSR. The photodiodes currents are converted into voltages by the TIA and acquired by a data acquisition board USB-231 from Measurement Computing.

The working device is shown in Figure 2.17. A complete software interface allows the user to program a new fluidic protocol or load a previously saved one, to choose the parameters of the wavelength scan such range and rate, to check the light intensities at the photodiodes and to align the fiber array to the chip with the micropositioner controller. Then with a single button click the measurement can be started. As the four MRR spectra are continuously acquired and saved for later analysis, a lorentzian fitting
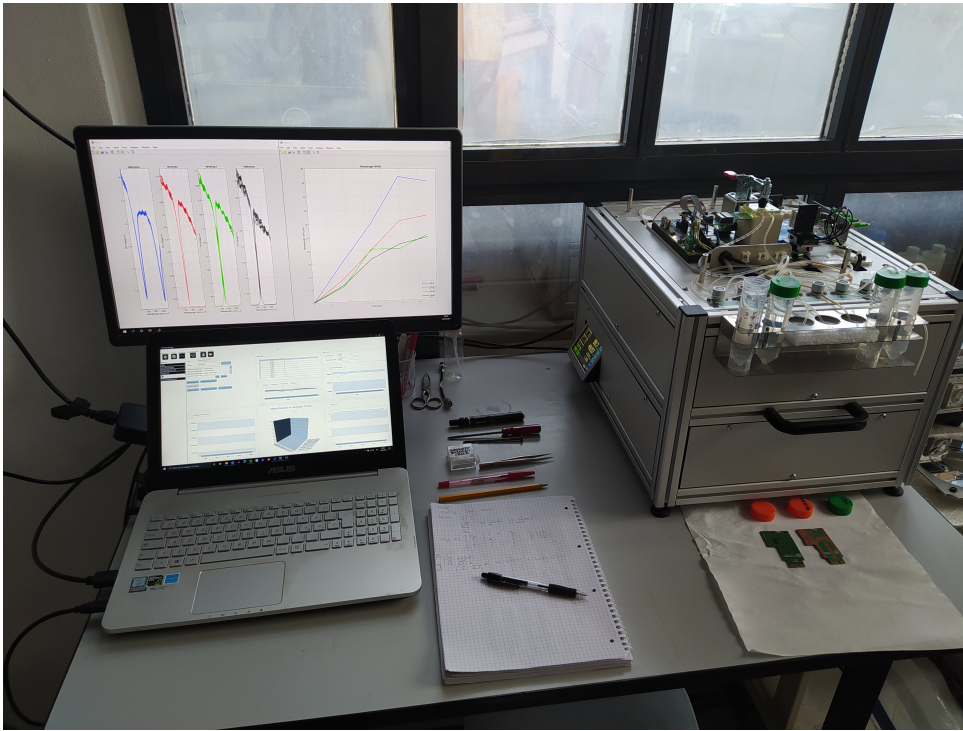
Figure 2.17: Diagnostic tool at work. Portable and easy to use, a laptop is enough to work with.

is performed and the resonance shifts are plotted in real-time.

Because of the slightly different method to change the laser temperature (direct external modulation vs serial communication) with respect to the laboratory equipment, we could not obtain the same accuracy in the wavelength scan. However, the noise in the track was measured in $15\,\mathrm{pm}$ leading to an estimated (Equation 2.3) $LoD \simeq 1 \times 10^{-4}\,\mathrm{RIU}$.

The tests we conducted on human samples from Dengue virus positive patients are reported in Appendix A. Biochemical issues regarding the probe molecule spotting and the secondary antibody prevented us to collect valuable data on the state of the patients' infection, but allowed us to verify the functionalities, the measurement tolerances and the possible outcome of the device, completing the design, prototipation and testing of a semiautomatic diagnostic device based on integrated photonics.

3 | Opto-Magnetic Labelling

3.1. Introduction

In the previous chapter we have seen how the classical approach to measure and quantify the entity of a biomolecular recognition has its advantages and disadvantages. The immediate benefits that can be noted are the simple sample preparation and the little time needed between sample collection and first response. As example, the steps required for a label-free measurement of antibodies in human plasma are: collect blood drops from the patient, dilute the sample if necessary, flux it into the fluidic system and collect few minutes of data from the sensor during the molecular hybridization. This approach can be fast and easy, but as already seen it is not suitable for very low concentrations of target molecule, because of noise and a possible lower binding efficiency in a fluidic cell. To improve performances at lower concentrations, we saw that a possible way to proceed is to exploit passive labelling techniques by using markers that enhance the sensor's response, but at the cost of having more needed steps while ensuring a good molecular binding efficiency, which can take longer times, as already seen. Tracking a resonance shift over long time may result in an increased difficulty to keep a low noise, due to mechanical oscillations, optical misalignment, temperature variations, small non-uniformities in chemical composition of involved fluids, and so on.

To overcome the issues, we propose a different approach that a) interrogates the sensor only after the recombination occurred, allowing to perform the molecular binding in the best possible conditions required by the biomolecules, b) it is more sensible at lower concentrations, improving the LoD thanks to the lock-in acquisition, c) it requires very little time to extract the needed informations, from few minutes to just few seconds. This technique falls in the active labelling category, in which the markers are not just passively enhancing the sensor's response like in the previous chapter, but they have a fundamental role in modifying a physical parameter measured by the sensor, in our case the resonance condition of the MRR. Since the method takes advantage of magnetic labels, oscillating magnetic field and it has been tested over optical MRR, we will refer to it as the opto-magnetic technique. It finds its first description in [8]. In this chapter, first

we will expose the concept at its base and how to exploit magnetic particles over optical structures. Then we will describe the experimental setup and the two methodologies we developed to perform the measurements. To conclude, the results will be shown and commented.

3.2.   Magnetic aspects

In the previous chapter we anticipated that the nanoparticles used for labelling the biomolecules have magnetic properties, which will be exploited in our opto-magnetic technique. To fully describe the active labelling approach, it is needed to have a brief overview on some properties and effects we are going to deal with, without entering too much in details.

Magnetic nanoparticles

Due to the domain wall width, magnetic objects are in a configuration of single domain when their sizes are smaller than a critical dimension. Being in a single domain configuration means that the magnetization, if we can assume the particles possesses uniaxial anisotropy, can be either parallel or anti-parallel with respect to the axis. Temperature can flip the magnetization, with an average time

$$\tau_n = \tau_0 \exp\left(\frac{KV}{k_b T}\right) \tag{3.1}$$

where T and k_b are the temperature and the Boltzmann constant, while V is the volume and K the material's anisotropy constant (expressed as energy per unit volume) that defines the energy barrier separating the two possible magnetization configurations. The time constant τ_0 lays between $10-12\times10^{-9}$ s, if the particles are non-interacting. Since the time needed to obtain a hysteresis loop measurement is typically considered to be 100 s, for a given temperature and material it is possible to find a critical volume for the flipping time to be lower, meaning $\tau_n < 100$ s. From Equation 3.1, the critical condition corresponds to $KV/k_b T = 25$. A particle with smaller volume than the critical one have a magnetization that jumps between the two states faster than the measurement time, leaving no magnetic remanence. These particles, when thermally activated, behave as paramagnetic objects and show a higher relative susceptibility than the paramagnetic materials, but still keeping the single atomic moments in their ferromagnetic order. Therefore these particles are called superparamagnetic [105, 106].

In normal conditions, superparamagnetic particles can be very small, with radius in the

order of 10 nm.

Low volumes leads to small magnetic forces, particularly true in biological applications, and the Brownian motion has a dominant role in their behaviour thus causing the particles' manipulation to be a difficult task. To overcome the issue, superparamagnetic particles arranged in ensembles are usually preferred. With diameters from tens of nanometers to microns, the assembled magnetic nanoparticles (MNP) are fabricated including superparamagnetic particles in a polymer matrix, as in Figure 3.1. Thanks to this structure, the magnetic moment of the MNP is simply the vectorial sum of all the superparamagnetic ones. The most common materials for the magnetic cores are magnetite Fe_3O_4 or magnemite Fe_2O_3.
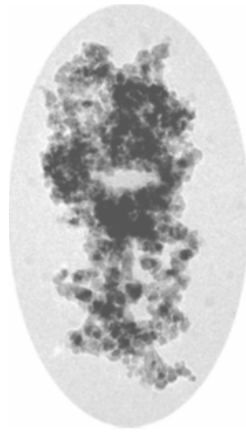
Figure 3.1: Picture of a magnetic nanoparticle. In this case section image of a 250 nm diameter nanomag-D, from Micromod catalogue.

MNP in magnetic field

When a MNP is subjected to an external magnetic field, its behaviour depends on the conditions. As in a magnetic compass, the magnetic moment is rotated to find the alignment with the external field. The particle achieves the alignment with two processes: Neel and Brownian relaxations [107, 108], in Figure 3.2a. Neel relaxation is the rotation of the magnetic moment inside the particle, while Brownians's one is the rotation of the particle, which mostly occurs in liquid suspensions. Being two different physical effects, the time constants of the two dynamics are different. Neel relaxation's time constant is described by Equation 3.1 since it is an intrinsic superparamagnetic behaviour, while Brownian's relaxation time constant is expressed by

$$\tau_b = \frac{3\eta V_h}{k_B T} \tag{3.2}$$

where η_{fluid} is the dynamic viscosity of the fluid and V_h is the hydrodynamic volume of the particle. Overall, the total relaxation time of such a particle is described by

$$\tau_{eff} = \frac{\tau_n \tau_b}{\tau_n + \tau_b} \tag{3.3}$$

and in Figure 3.2b it is reported an example of relaxation times for particles with different volumes [109]. When particles are larger than 20 nm in diameter, the relaxation favours
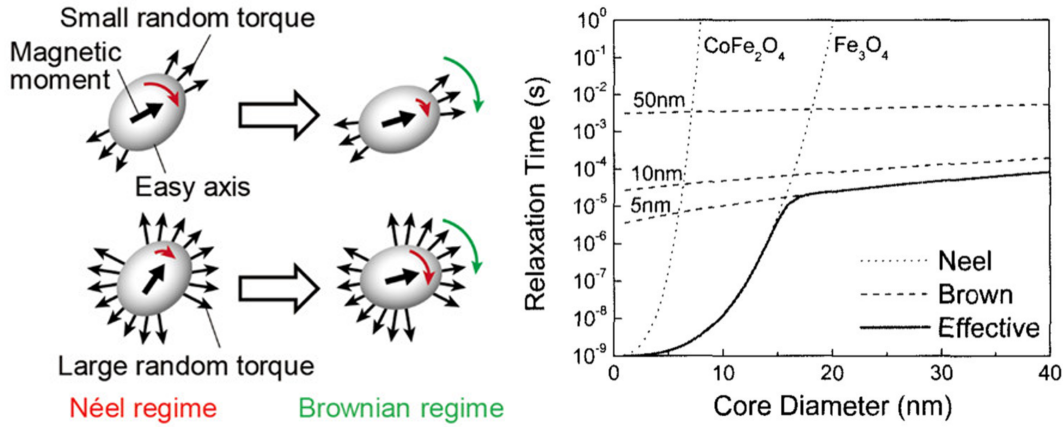
Figure 3.2: Brownian and Neel relaxations: mechanism and time as function of dimension. From [110].

Brownian mechanism, rotating the particles rather than the magnetic moment. Since for our experiments and measurements we used particles with an average diameter size of 130 nm, we can confidently state that the Brownian relaxation time τ_b is a close estimation for τ_{eff}.

As seen, a uniform field generates a torque while to obtain a translation it is required a magnetic field gradient [111]. The magnetic translational force is given by the gradient of the magnetic field and the magnetic moment **m** of the particle according to $\mathbf{F}_{mag} = \nabla(\mathbf{mB})$. While considering small single domain particles, the absolute value of the field gradient can be used to determine the magnetic force, but for larger MNP the force depends on the particle's volume V_{MNP}, its magnetic susceptibility with respect the environment susceptibility $\Delta\chi$, amplitude and gradient of the magnetic flux density **B**.

With some approximation for a simpler approach, we have

$$\mathbf{m} = V_{MNP}\mathbf{M} \tag{3.4}$$

$$\mathbf{M} = \Delta\chi\mathbf{H} \tag{3.5}$$

$$\Delta\chi = \chi_{MNP} - \chi_{env} \tag{3.6}$$

$$\mathbf{H} = \mathbf{B}/\mu_0 \tag{3.7}$$

where $\mathbf{H}$ is the applied magnetic field and $\mathbf{M}$ the magnetization field. Considering that the MNP is in position $\mathbf{r}_c$ and it is smaller than the length scale related to the magnetic field gradient we can write

$$\mathbf{F}_{mag} = \mu_0 \int_{V_{MNP}} (\mathbf{M} \cdot \nabla)\mathbf{H}dV \approx \mu_0 V_{MNP}(\mathbf{M}(\mathbf{r}_c) \cdot \nabla)\mathbf{H}(\mathbf{r_c}) \tag{3.8}$$

By considering the material of the MNP to have a linear susceptibility and to be isotropic and present negligible dispersion, we can simplify the previous equation into

$$\mathbf{F}_{mag} = \mu_0 \Delta\chi V_{MNP}(\mathbf{H}(\mathbf{r}_c) \cdot \nabla)\mathbf{H}(\mathbf{r}_c) \tag{3.9}$$

and recognizing the identity

$$(\mathbf{A} \cdot \nabla)\mathbf{A} = \frac{1}{2}\nabla(\mathbf{A}^2)$$

we obtain

$$\mathbf{F}_{mag} = \frac{1}{2}\mu_0 \Delta\chi V_{MNP}\nabla(H^2(\mathbf{r}_c)) \tag{3.10}$$

Thus, to optimize the magnetic force acting on the MNP, one can work with the involved materials, the particles volume and the gradient of the squared magnetic field. Since the MNP are usually fixed by manufacturers in terms of materials and dimensions, the main parameter is represented by the field. Optimizations and studies can be performed in order to maximize ∇H^2 thanks to different designs of the field generators.

3.3.   Active labelling

The opto-magnetic technique is an hybrid approach between optical measurements in integrated optics and magnetic manipulation of particles. These two aspects are joint together to generate a particular behaviour at the output of the optical cavity and a lock-in technique extracts low noise signals that are easy to process. Therefore it is important to study how the magnetic particles are activated and how the MRR responds to the

modified environment.

Opto-magnetic labelling

The MRR is in Add-Drop configuration, with three ports actively used: Input, Through and Drop. As reported in Chapter 2, the waveguide is first functionalized with a molecular probe over a tiny layer of copolymer. The hybridization process creates a structure in which the probe and target ssDNA form a double helix dsDNA with a MNP bound to the top. The resonance shift can be tracked to quantify the target analyte concentration.

The basic concept of the active labelling we used is pictured in Figure 3.3. Once the
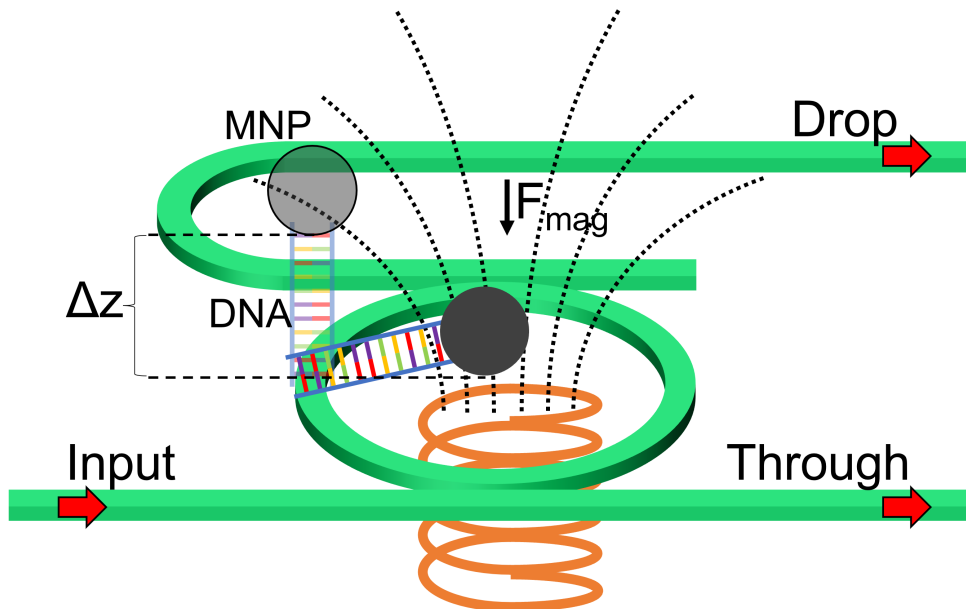
Figure 3.3: Conceptual image of the opto-magnetic technique.

hybridization process took place, an external magnetic field can be applied. Biological materials, with some exceptions [112], are not much affected by the magnetic field, but the MNP perceives a magnetic force which direction and intensity is proportional to the gradient of the field squared, as in Equation 3.10. If the magnetic field presents a gradient that is vertically oriented, condition valid for an electromagnet placed below the MRR, the MNP is attracted toward the waveguide.

Since the 60 base-pairs dsDNA are roughly 20 nm long and the persistence length of this molecule is computed to be around 200 nm, a simple estimation for the motion is that the double helix will behave as a nearly stiff rod with an end fixed on a joint. The system DNA-MNP, under the influence of an external vertical magnetic field gradient, bends towards the sensor's surface creating a displacement in the vertical position of the MNP. We have already seen how much the MNP presence affect the effective refractive index

n_{eff} and, consequently, the resonance condition of the light in the cavity. The changed position of the MNP modifies the disturbance effect, shifting the resonating wavelength.

The increased wavelength shift produced by the closer MNP is already exploitable as sensing approach if the resonance is being tracked. But instead of static, the magnetic field can be generated by an AC current. This results in a sinusoidally oscillating magnetic field at a frequency ω_0 and so the quantity $H(t)^2$ can be expressed as

$$H^2(\mathbf{r}_c, t) = |H_0(\mathbf{r}_c)|^2 \sin^2 \omega_0 t = \frac{|H_0(\mathbf{r}_c)|^2}{2}(1 - \cos 2\omega_0 t) \tag{3.11}$$

and it oscillates at double frequency $2\omega_0$. The same behaviour is followed by $\nabla(H^2)$ and, because of Equation 3.10, also F_{mag}. Therefore an AC magnetic field at frequency ω_0 generates on the MNP a magnetic force that oscillates at $2\omega_0$, displacing the particle at the same rate. This periodic perturbation causes the resonance condition to be modified creating an oscillating $\Delta\lambda_{2\omega_0}$ that we are going to exploit.
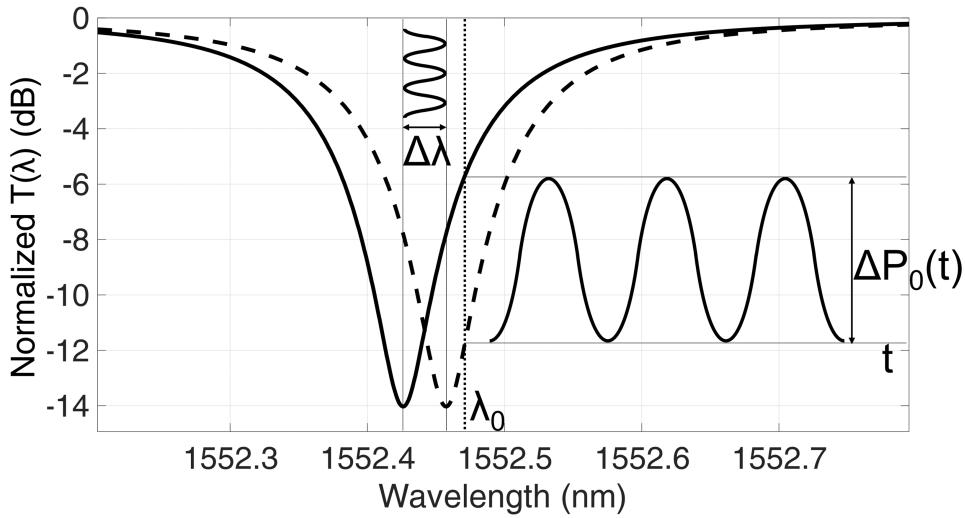
Figure 3.4: The resonance condition periodical shifts induce an oscillating output power that depends on the slope of the transfer function and on the intensity of the oscillation.

In Figure 3.4 an example of the transfer function $T(\lambda)$ of a MRR is plotted. The oscillating MNP produces the $T(\lambda+\Delta\lambda)$ shifted curve. A lasing input fixed at λ_0 wavelength produces a variation of the detected optical power $\Delta P_o(t)$ at the output port. The amplitude $\Delta P_o(t)$ of the power oscillation depends both on the slope of $T(\lambda)$ and on the wavelength shift $\Delta\lambda$, thus it contains informations about the quantity of MNP fixed at the waveguide surface.

3.4. Sensitivity of the MRR

To have a clear view of the effects of the MNP oscillating over the MRR and since we are going to look at the output power, we need to analyze the sensor properties. Considering the optical output power P_o of the resonating cavity, its variation ΔP_o with respect to the input power P_i can be expressed as

$$\frac{\Delta P_o}{P_i} = S_s \Delta_{env} \tag{3.12}$$

where S_s is the sensitivity of the biosensor to a generic environmental parameter modification Δ_{env}, which can be expressed as, for example, a temperature change or a refractive index change. In our case the environmental parameter affecting the sensor behaviour is the MNP-waveguide distance. Taking into consideration the tranfer function, Equation 3.12 can be rewritten as

$$\frac{\Delta P_o}{P_i} = S_s \Delta_{env} = \frac{\delta T}{\delta_{env}} \Delta_{env} \tag{3.13}$$

and with some arrangement we can identify three different terms for the sensor sensitivity

$$S_s = \frac{\delta T}{\delta_{env}} = \frac{\delta T}{\delta \lambda} \frac{\delta \lambda}{\delta n_{eff}} \frac{\delta n_{eff}}{\delta_{env}} = S_i S_\lambda S_{env} \tag{3.14}$$

Those terms are important to understand the response of the sensor when a parameter is changing:

- $S_{env} = \delta n_{eff}/\delta_{env}$ is the waveguide sensitivity to the environment and indicates how much the effective refractive index n_{eff} is modified by the external changes δ_{env}, the MNP-waveguide distance in our case;

- $S_\lambda = \delta \lambda/\delta n_{eff}$ is the wavelength sensitivity and gives how much the resonating wavelength of the cavity shifts for a given n_{eff} variation;

- $S_i = \delta T/\delta \lambda$ is the interferometric sensitivity and expresses the dependence of the transfer function variation with respect to the wavelength, i.e. the $T(\lambda)$ slope.

These three terms have to be analyzed to obtain a meaningful relation between ΔP_o and Δ_{env}.

The waveguide to environment sensitivity S_{env} is an important parameter to consider when optimizing biosensing platforms and it can be estimated depending on the environmental parameter under change. Being the opto-magnetic technique based on the oscillations of MNP above a MRR, numerical simulations have been implemented to study the ef-

fect. In Figure 3.5a the COMSOL Multiphysics simulation shows the silicon waveguide and the electromagnetic field. The MNP is modeled as an iron-oxide inner core and a dextran-polymeric shell, and as it is being placed at different distances from the waveguide top surface, the n_{eff} is extracted. Being a 2D simulation, the result has to be scaled considering the ratio between the volume of a spherical MNP and the volume of the thoroid extruded over the MRR circumference, as shown in Figure 3.5b, thus obtaining a reasonable approximation of the real case of a single MNP over the whole MRR sensor. Evaluating the n_{eff} for several distances of the particle from the waveguide and taking its first derivative, we obtain $S_{env} = \delta n_{eff}/\delta_{env}$. As shown in Figure 3.5c for 20 nm long biomolecules labelled with 130 nm MNP over our MRR we are expecting a change in the n_{eff} in the order of 10^{-9} RIU for each nanometric displacement for each MNP, thus $S_{env} \sim 10^{-9}$ RIU.
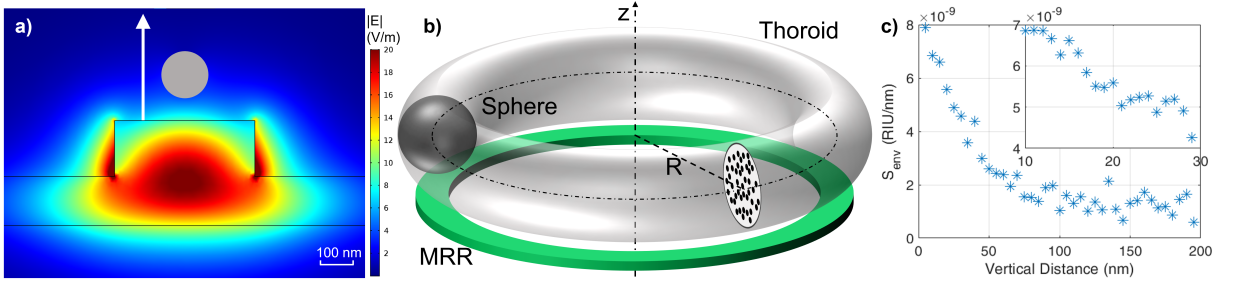
Figure 3.5: Numerical simulation to evaluate S_{env}, i.e. the dependence of n_{eff} from the waveguide-MNP distance. (**a**) COMSOL simulation for several distances; (**b**) the 2D simulation represents in 3D a toroid MNP over the waveguide: the single-MNP caused n_{eff} variation is estimated from the sphere to torus volume ratio; (**c**) S_{env} (Δn_{eff} caused by a 1 nm MNP displacement) dependence on the waveguide-MNP distance. Inset: S_{env} evaluated around the 20 nm waveguide-MNP distance, giving a conservative value of $S_{env} \sim 10^{-9}$ RIU.

The waveguide sensitivity S_λ quantify the MRR resonance change as the effective refractive index n_{eff} is modified by external conditions and it is not dependent by the optical structure. From $S_\lambda = \delta\lambda/\delta n_{eff}$ and knowing that the group refractive index is defined by $n_g = n_{eff} - \lambda \delta n_{eff}/\delta\lambda$, we have

$$S_\lambda = \frac{\delta\lambda}{\delta n_{eff}} = \frac{\lambda}{n_g} \tag{3.15}$$

so this term is determined just by the working wavelength and the group refractive index. For λ=1550 nm and $n_g = 3.89$, it results $S_\lambda \simeq 400$ nm/RIU.

The last term to consider is the interferometric sensitivity S_i and it is calculated as the slope of the transfer function. With just S_i, the power variation is related to the wavelength shift by

$$\Delta P_o(\lambda_0) = S_i(\lambda_0)\Delta\lambda_{2\omega_0} \tag{3.16}$$

In Figure 3.6 a normalized example of transfer function $T(\lambda)$ is plotted along its slope's absolute value $|\delta T(\lambda)/\delta\lambda|$. To maximize the overall effect it is necessary to set as working point the wavelength with the maximum slope: the methods we used to collect the data at the best wavelength is described in the next Sections. Depending on how the output of MRR is expressed ($T(\lambda)$ unit of measure), S_i will have different values. In the Section dedicated to the measurements of this Chapter we will see that $T(\lambda)$ is measured in V and a typical value, yet not constant for all the measures, for the slope is $|\delta T(\lambda)/\delta(\lambda)| \simeq 2.5\,\text{mV/pm}$.
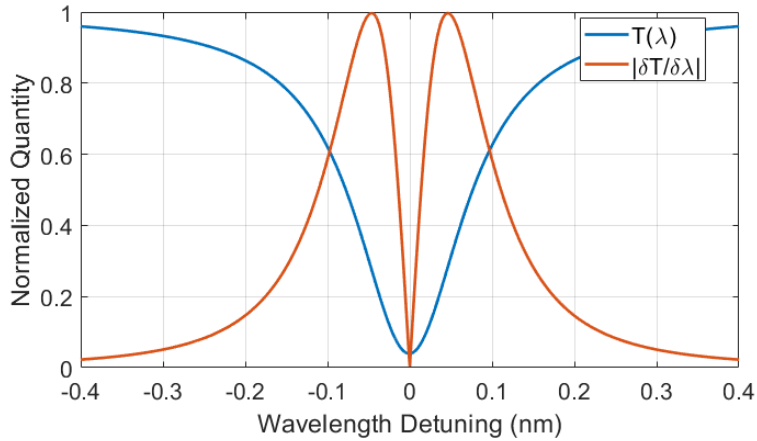
Figure 3.6: Ring transfer function and its slope. The best working points are at $|\delta T(\lambda)/\delta\lambda|$ peaks.

To conclude the sensitivity considerations for this labelling method with our platform and our experimental setup, we can recap the obtained values end estimate an overall sensitivity S_s

$$
\begin{aligned}
S_i &\simeq 2.5\,\text{mV/pm} \\
S_\lambda &\simeq 400\,\text{nm/RIU} \\
S_{env} &\sim 10^{-9}\,\text{RIU} \\
S_s &= S_i S_\lambda S_{env} \sim 1\,\mu\text{V/nm}
\end{aligned} \tag{3.17}
$$

that can be interpreted as an expected output value change of $1\,\mu\text{V}$ for every MNP on the MRR that is being vertically displaced from its $20\,\text{nm}$ distance by $1\,\text{nm}$.

3.5.   Experimental setup

To be performed accurately, biosensing with the opto-magnetic technique needs an experimental setup that properly joins the optical components and the integrated photonic chip, the magnetic field generator and its driver, the fluidic system with pump, fluidic cell and tubing and the electronics to control the system and manage the signals. All these aspects are fundamental in a system that is meant to perform accurate diagnostic measurements form the patient's sample to the final result with as little uncertainty as possible.

Preliminary tests have been conducted as proof-of-concept with a simple assembly and mainly performed by N. Peserico and C. Groppi [8]. In those cases the laser light was generated by a tunable laser source for bench-top applications and reached the all-optical sensor with a SMF. A second SMF collected the light from one of the output (usually the Through) and an external photodiode measured the optical power. To analyse the optical oscillation intensity, a lock-in amplifier processed the PD readout voltage obtaining some sort of value for ΔP_o. The tests gave an idea on how the approach may behave, but there were many problems that later developments tried to solve. To have access to input and output grating couplers placed in different areas of the optical circuit, the chip had to be exposed to air: while it is possible to deposit a drop of saline solution on the sensor to allow the biomolecules to oscillate, any liquid tend to evaporate, changing saline concentration and refractive index causing biochemical instabilities on the molecules under test. The action of depositing liquids on an optically coupled chip will likely disturb the alignment, decreasing the overall optical power in the chip and consequently also ΔP_o. Another difficult task is how to set as working point the wavelength presenting the maximum slope of the transfer function $T(\lambda)$ since the evaporating fluid cools the surface while the electromagnet warms it up.

With these considerations it is clear that an optical biosensor have to be developed as a system able to join all the different technological aspects. Effort has to be put in finding the best solutions to use optical, magnetic, electronic and fluidic systems altogether assuring reliability, repeatibility of measurement and to be able to extract meaningful results.

The experimental setup is pictured in Figure 3.7. As clear form the scheme, some parts are in common to the described setup in Chapter 2 since the system was designed to be efficiently used both for hybridization tracking and opto-magnetic measurements with little to no adjustments. Therefore the optical components and the fluidic circuit are the very same from the previous Chapter. The main differences are in the electronic
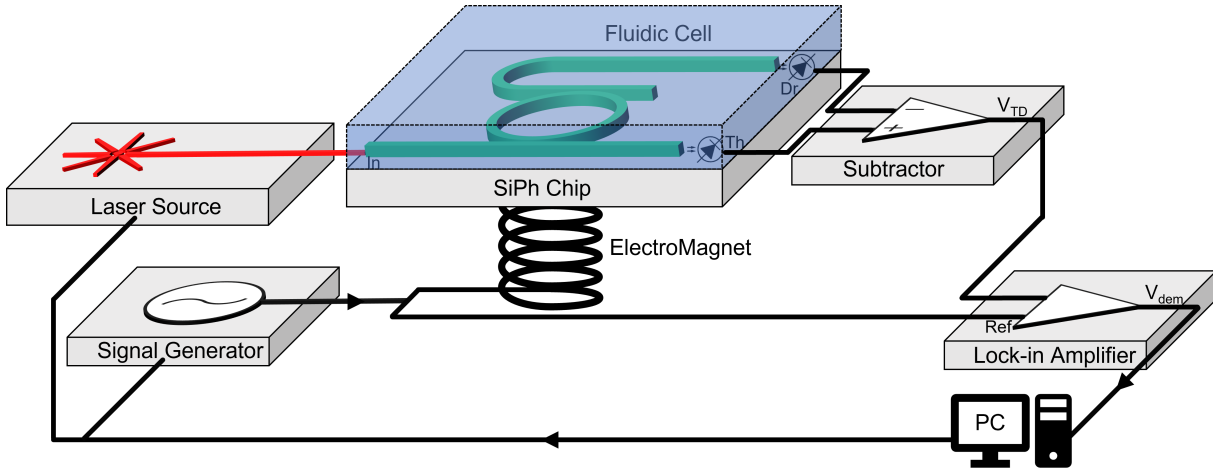
Figure 3.7: Opto-magnetic setup scheme. Many components are in common with the setup seen in Chapter 2. In addition there are a signal generator, an electromagnetic coil and a lock-in amplifier. The control software manages the various components.

connections, software controls and interfaces and of course in the magnetic part. The differential voltage $V_{TD} = V_{Through} - V_{Drop}$ from the TIA of the sensor under test is brought to the DAQ for acquisition and to the lock-in amplifier, a HF2LI from Zurich Instrument. Here, by imposing a bandwidth filter of $5\,\mathrm{Hz}$, a demodulator extracts the second harmonics (due to Equation 3.11) of a reference frequency obtaining V_{dem} at the output, which is acquired by the DAQ. The reference is generated by the internal signal generator of the LIA.
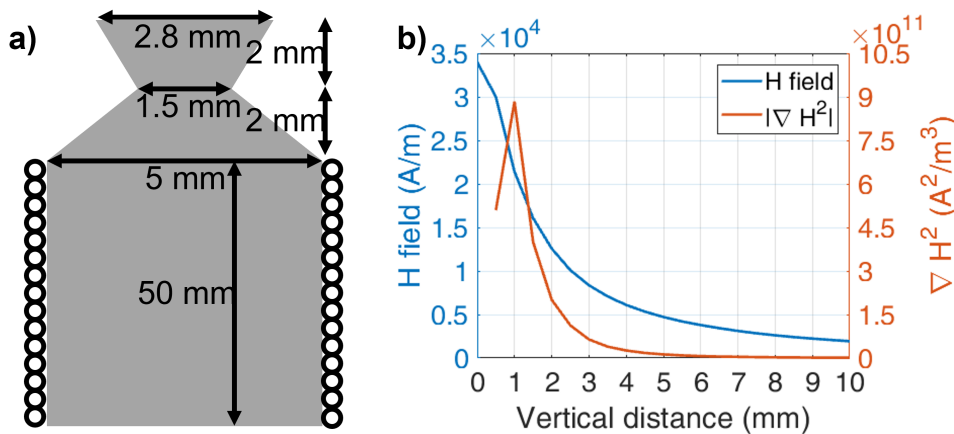
Figure 3.8: Electromagnetic coil: (**a**) structure and (**b**) measurements to characterize H and ∇H^2.

The signal, at frequency f_{EM} and with peak V_{EM}, controls the power supply Kepco BOP-36-12M that drives the magnetic field generator. The electromagnet, scheme in Figure

3.8a and designed by C. Groppi, is constituted by an iron core of $5\,\mathrm{mm}$ diameter and $50\,\mathrm{mm}$ long mounted on a micropositioner. At the top, the extremity has a bottle-neck shape, designed to maximize ∇H^2. Copper wire of $0.8\,\mathrm{mm}$ diameter is winded around the core for a total of 62 turns; measurements show an electrical resistance of $1\,\Omega$. A characterization of the magnetic field has been performed and it is plotted in Figure 3.8b. For a current $I_{EM} = 2A$, the gradient of the squared magnetic field reaches values in the order of $|\nabla H^2| = 10^{11} - 10^{12}\mathrm{A}^2/\mathrm{m}^3$ in the first millimeter above the tip. In some cases it may be necessary to inject high current in the coil. To avoid the excessive heat to disturb the measure and stress the biomolecules, several turns of a $1.5\,\mathrm{mm}$ diameter tube are fixed around the electromagnet with running water in it. This liquid cooling solution kept the element's temperature in an acceptable range.

Every component is controlled by a custom LabView interface that sets the needed values, controls the laser wavelength, acquires the data and saves them in a easily readable file.

A picture of the actual experimental setup is reported in Figure 3.9. From the top left there are the laser drivers, the laser and the SMF array on the micropositioner. The PCB carrying the silicon chip and the fluidic cell with tubes is right in the center, with the pluggable cable connecting it to the electronic board with the TIAs. The amplifier outputs are brought to BNC cable switch box to route the correct signals to the DAQ and to the LIA.

Thermal effects are usually an issue in integrated photonic circuits, due to the thermo-optic effect that links refractive index of the materials and temperature. Typically, temperature is controlled by means of a Peltier cell under the chip. As for the opto-magnetic measurements, thermal effects of the environment and the coil are less relevant. The coil gradually heats the chip causing a slow wavelength shift of the resonance of the MRR, but since we are extracting the second harmonics of f_{EM} frequency we do not perceive the slow change. Plus, the heat involves both sensing and reference MRR: the wavelength shift caused by thermal fluctuations is treated as common noise and therefore eliminated by comparing the two sensing elements.

3.6. Wavelength scan measurements

The opto-magnetic measurements are performed after the hybridization took place. In fact, being the technique an off-line approach, the interrogation process can be performed just after the biomolecular recognition but also hours or even days later if the chips with the molecule system are kept under stable conditions, i.e. avoiding direct light, maintaining a stable cool temperature and in buffer solution bath or fixed humidity environment.
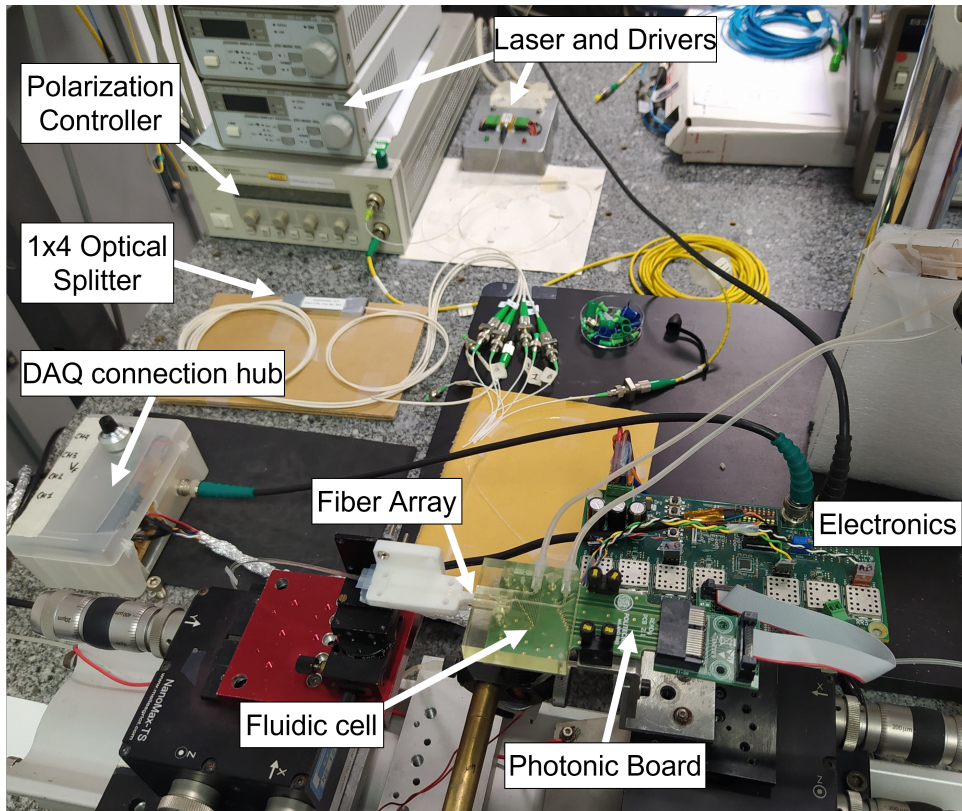
Figure 3.9: Photo of the opto-magnetic laboratory bench setup. At the top the laser , its drivers, the polarization controller and the 1x4 splitter are visible. The optical fiber array is coupled to the chip, that is mounted on the photonic board, which hold the fluidic cell with its tubes. The electrical signals are amplified by the reading electronics

Preparation and calibration

The measurement start with fixing the PCB on its support and plugging in the cable for the PDs. The laser light is turned on to perform the alignment between the optical fiber array and the grating couplers of the chip. With our setup, up to four MRR can be tested simultaneously. Polarization state is set maximising the optical powers at the through ports. The electromagnet is then accurately placed right below the center of the chip. At this point the electromagnet and the LIA are turned on to perform the parameters calibrations: it is important to stimulate the labels at the right frequency and with the correct magnetic force.

The choice of the frequency f_{EM} to be applied to the electromagnet is performed by sweeping it and looking at the demodulated signal V_{dem} when the wavelength is at the maximum $T(\lambda)$ slope. A good frequency should be higher than the $1/f$ noise and lower than a possible pole in the biomolecule-MNP system. In Figure 3.10 the V_{dem} spectrum shapes are confronted for two very different situations. In one case (Figure 3.10a), the

MNP are bound to the molecules and the chip has been properly rinsed by fluxing a buffer solution in the fluidic cell. It is clearly visible a flat response at lower frequencies, a pole around 100 Hz and then a descending slope indicating the classical behaviour of an overdumped system in which F_{mag} is the external force, the DNA or the proteins act as springs and the drag is produced by the fluid. The reference MRR has less MNP on its surface and therefore presents a lower signal. The other curves (Figure 3.10b) have
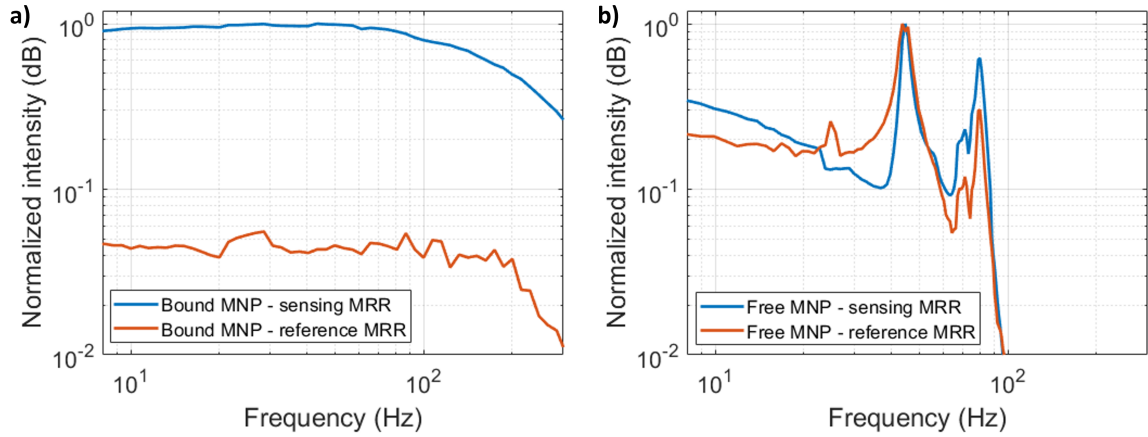
Figure 3.10: Calibration of f_{EM}: effect on sensing and reference MRR of (**a**) bound and (**b**) free-floating MNP. Unbound MNP create high intensity resonances at various frequencies.

been obtained by a MRR on which a large number of MNP did not find the probe and have not been rinsed. In this case the many free-floating MNP produce several resonance behaviours that can be seen on both sensing and reference MRR without any sort of difference, being the MNP homogeneously present. These resonances are most probably caused by the rotation of these particles. Brownian relaxation frequency can be retrieved from Equation 3.2

$$f_B = \frac{k_B T}{6\pi \eta_{fluid} V_h} \tag{3.18}$$

Considering a PBS viscosity $\eta_{fluid} \simeq 1\,\text{mPa s}$ [113] and a hydrodynamic radius of 65 nm we obtain a frequency of $f_B = 190\,\text{Hz}$. Since our demodulator extracts the second harmonic of f_{EM}, the effect of these rotations are expected to be around 95 Hz, in fair accordance with a measured peak. However, different observations demonstrated that these values were not fixed, most probably due to MNP aggregating into clusters of variable dimensions. We solved the issue of unknown resonances by periodically fluxing some buffer liquid into the cell in order to rinse the MRR surface and remove unbound MNP, suppressing the noise peaks and recovering a flat spectral response. At the end of the process, the frequency for the electromagnet actuation was chosen to be $f_{EM} = 80\text{Hz}$.

A second calibration is necessary to choose the correct amplitude of the magnetic field. A too weak magnetic field gradient cannot generate enough magnetic force to appreciably move the MNP, while a strong magnetic force can inhibit the MNP to oscillate bending the molecules out of their elastic range or sticking them to the copolymer layer on the surface. An effect to be considered is the increased electromagnetic noise that can be collected by chip's metal strips and PCB electrical routings as the magnetic field intensity rises. The
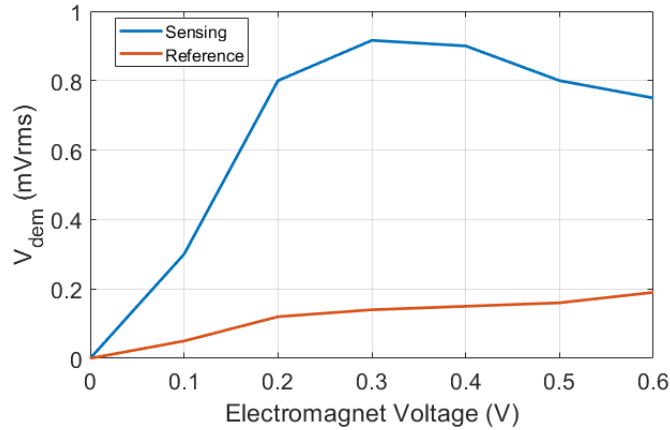
Figure 3.11: Calibration of V_{EM}: as the intensity of the magnetic field is increased the sensing signal rises until a peak is reached, while reference increases steadily.

voltage applied to the electromagnet has been changed to find the best response and as visible in Figure 3.11, the demodulated signal V_{dem} for a MRR with biomolecules and MNP on the surface increases rapidly, finds a large peak between 0.2 V and 0.5 V and then decreases. The signal V_{dem} from a reference MRR with no bound MNP steadily increases, indicating the presence of collected noise and spurious effects. A good compromise was found fixing V_{EM}=0.5 V, that corresponds to a magnetic field intensity at the surface of the chip of $H = 2-5 \times 10^3$ A/m.

Measurements

Once the fundamental parameters are fixed, the actual measurements can be performed. Since to improve the overall sensitivity, as discussed, it is important to perform the opto-magnetic measure at the wavelength that maximises $|\delta T/\delta \lambda|$, an effective and reliable solution is to perform a wavelength scan over a FSR of the MRR, as in Figure 3.12.

Acquiring simultaneously the transfer function $V_{TD}(\lambda)$ and the demodulated signal V_{dem} from the LIA, it is possible to directly compare V_{dem} to the slope $|\delta T/\delta \lambda|$ with the re-
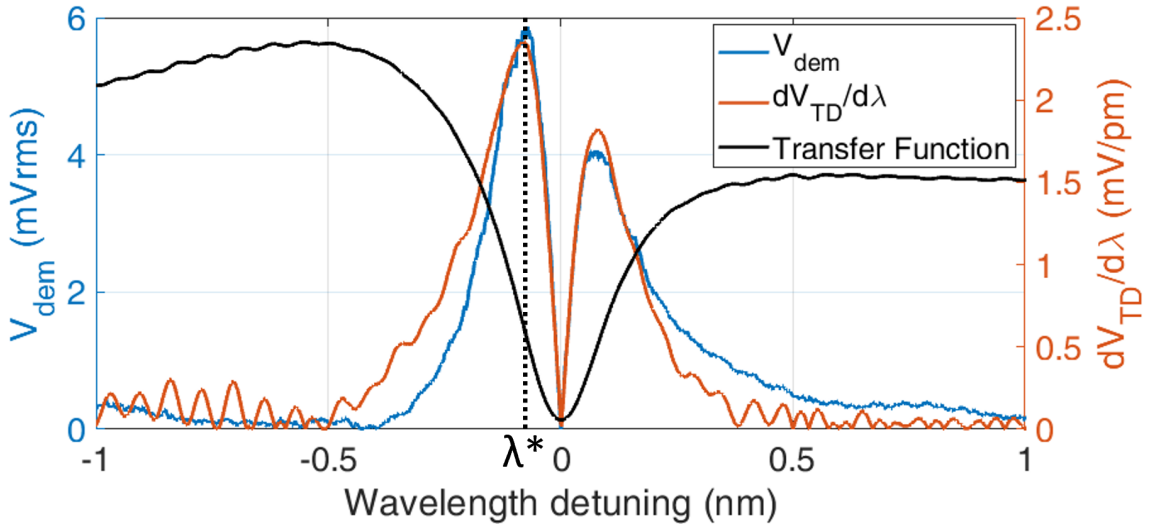
Figure 3.12: Typical opto-magnetic acquired curve. From the transfer function (black, no scale) we calculate the slope (red) while the demodulator extracts V_{dem} (blue). The transfer function derivative and demodulated signal are proportional. Scan obtained with DNA 1 nM.

arranged Equation 3.16:

$$\Delta\lambda_{2\omega_0} = \frac{\Delta P_0(\lambda_0)}{S_i(\lambda_0)} \quad \leftrightarrow \quad \Delta\lambda^* = \left(\frac{V_{dem}}{dV_{TD}/d\lambda}\right)_{\lambda^*}. \tag{3.19}$$

in which λ^* is the wavelength at the maximum $T(\lambda)$ slope. The peak positions of the scan allow a low noise evaluation of the two quantities and the amplitude of the resonance condition oscillation $\Delta\lambda^*$ is obtained by just dividing them.

The wavelength scan is performed at a fixed speed of 10 pm/s to let the LIA acquire properly the signal and filter with a 5 Hz bandwidth. When possible, the analysis is performed simultaneously on both sensing and reference MRR, to have a full comparison of the results.

Results

The wavelength scan method for the opto-magnetic technique has proved to be reliable and allowed to measure several MRR, both functionalized and not, on which different target concentrations has been fluxed during the hybridization process. For the DNA measurements, the tested concentrations range from a maximum of 1 µM to a minimum of 10 pM and the calculated $\Delta\lambda^*$ results are plotted in Figure 3.13.

For the sensing MRR, the relation between the wavelength oscillation amplitude and
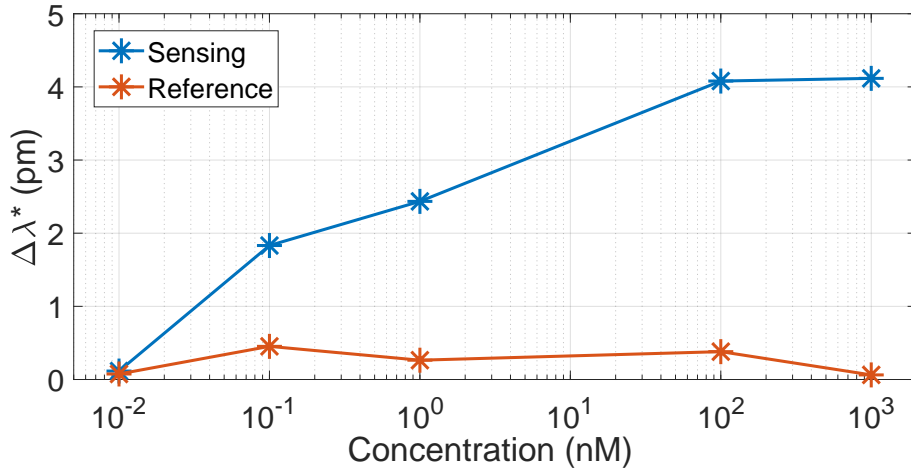
Figure 3.13: Extracted MRR resonance oscillations caused by the MNP agitating over the waveguide, being activated by an AC magnetic field. The difference between sensing and reference sensors is more appreciable at higher concentrations, but is lost around 10 pM.

the target concentration is clear: with higher analyte concentrations, more MNP are immobilized to the surface of the chip, oscillating under a magnetic force attraction and perturbing the resonating cavity. From the plot it is visible that the reference MRR responses are lower and evenly distributed, meaning that they are not related to the target molecule concentration, but most likely those signals come from free-floating MNP still present in the fluidic cell or a-specific binding between the copolymer and the target molecule or the MNP. Looking at the plot the lowest detectable concentration in this case appears to be in the range $LoD = 10-100$ pM, since at 10 pM sensing and reference are not anymore recognizable.

The collected values for the references show an average μ_{ref} =250 fm with a standard deviation σ_{ref} =175 fm, that leads thanks to Equation 2.3 to an expected limit of detection in refractive index variation of $LoD \sim 10^{-6}$RIU.

In the previous Chapter we have seen how the passive labelling improved our LoD from the label-free detection by one order of magnitude. In this case, with the active labelling opto-magnetic technique we improved by another factor of 10 using the same microchip and MRR.

3.7.   Feedback measurements

In Chapter 2 we described a technique based on a feedback loop we use to track the resonance position. In this approach, the add-drop configuration of the MRR has a crucial role, since the feedback signal is generated by the output powers at the ports. The

Through and Drop light intensities, expressed in terms of voltages, are compared and a PID controller generates an error signal that drives the laser to adjust the wavelength in order to keep it at the crossing point between the two transfer functions, roughly at $-3\,\mathrm{dB}$ from the maximum intensity. Monitoring the error signal in the feedback loop, we have the information on how much the resonance is moving from the starting point. Thanks also to insensibility to common power fluctuations, the feedback proved to be very fast and precise, with a tracking error of $\sigma_{feedback} \simeq 20\,\mathrm{fm}$ (see Figure 2.12).

The opto-magnetic technique produces a small shift in the MRR resonance that the wavelength scan method quantifies in the pm range, so it is reasonable to expect that the feedback loop would guarantee increased performances thanks to the improved accuracy. That is definitely true, but only if the MNP do not affect too much the quality of the resonance. The feedback method directly measure the wavelength shift of the MRR resonance condition, so it bypasses the issue of scanning the FSR to find the best slope position. In contrast, modifications on the Q-factor of the resonance lead to a slope change at the Through-Drop crossing point, changing the loop behaviour. Moreover, in some cases it is not possible to perform the feedback measurements since the Drop peak was not existent or was too far from the Through notch, causing the absence of a crossing point to which the laser had to be locked.

Results

The resonating wavelength measurements with the feedback have been conducted in particular at the lowest concentrations tested. The crossing point position is encoded in the feedback arm of the loop. To obtain its wavelength it is just needed to multiply the feedback voltage by the voltage to current and current to wavelength coefficients of the laser and its current driver.

The measurement were conducted with an On-Off interrogation scheme, switching on the electromagnet for few seconds and then switching it off, from hence the name.
A huge advantage of this approach compared to the wavelength scanning method, is that the modulation amplitude is expected to be roughly constant as long as the electromagnet is on. The demodulator filter can be set to a narrower window ($0.1\,\mathrm{Hz}$ filter bandwidth), with a strong noise extinction and a more accurate quantification of the resonance oscillation.
A great example of the capabilities of the feedback method measurements can be found in Figure 3.14, which shows the On-Off measurements of a sensing and a reference MRR for a concentration of $10\,\mathrm{pM}$. The previous techniques were able to distinguish the two sensors down to concentrations at the level of $10\,\mathrm{nM}$ for the label-free, $1\,\mathrm{nM}$ for the pas-
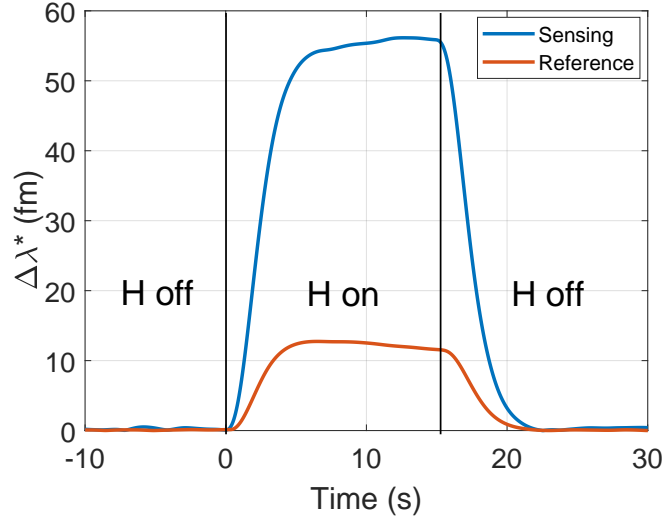
Figure 3.14: On-Off opto-magnetic measurement at $10\,\mathrm{pM}$. The narrow bandwidth filter of the lock-in amplifier demodulator removes lot of noise, enhancing the small resonance oscillation. The system interrogation lasts just few seconds.

sive labelling, $100\,\mathrm{pM}$ for the wavelength scan active labelling, while the On-Off with the feedback is clearly distinguishing sensing from reference MRR at $10\,\mathrm{pM}$: another order of magnitude in the lowest detected concentration.

The noise level is very low thanks to the narrow window of the lock-in filter. A $10\,\mathrm{s}$ plateau can be considered to evaluate average μ and standard deviation σ of the two signals, no additional post-processing filtering have been used to calculate these parameters. The reference MRR shows an average value of $\mu_{ref} = 12.3\,\mathrm{fm}$ while the sensing one a higher value of $\mu_{sens} = 55.5\,\mathrm{fm}$. The signal error can be evaluated according to the standard deviations that measure $\sigma_{ref} = 0.35\,\mathrm{fm}$ and $\sigma_{sens} = 0.6\,\mathrm{fm}$, a strong improvement in low wavelength shift detection.

Applying in this case Equation 2.3 to a $\sigma_{\lambda,On-Off} \sim 1\,\mathrm{fm}$, the theoretical limit of detection of this innovative technique results in $LoD_{On-Off} \simeq 7.5 \times 10^{-9}\,\mathrm{RIU}$, definitely a great result for several reasons:

- the theoretical LoD_{On-Off} is several order of magnitude better than ones obtained with the other techniques presented in this work

- the LoD is calculated from the error in wavelength tracking, meaning that a MRR built from a platform that presents a higher sensitivity (e.g. a slot waveguide MRR) can reach very interesting concentration limits

- even if these measurements have been performed after the whole hybridization pro-

cess, the time required to interrogate the system is very low (15 s)

The great precision in measuring small wavelength oscillations is a great advantage that can be exploited in two ways: a) performing the measurement like we did, it would be possible to detect very low concentrations of analyte, lower than the lowest one detected in this work; b) a second approach to exploit the system performances could be to start interrogating the system as soon as MNP are introduced into the fluidic cell. Being able to detect low number of oscillating MNP the system will measure an increasing wavelength oscillation amplitude as the binding process progresses. In this way the assay can return a quantitative result faster than usual labelling techniques.

4 | Integrated Opto-Magnetic Platform

4.1. Introduction

Citing [114]: *"Certain optical biosensors have been introduced into the market, but most of them are bulky and expensive. The complete integration of a sensor as well as single-chip detection forming a mechanically stable, reproducible, and user-friendly device has becoming imperative for future investigations. Because intensive investigations are being performed, integrated, miniaturized, and portable biosensors will undoubtedly become universal in our daily lives and positively impact our lives in the near future".*

In Chapter 3 the active labelling technique, here named opto-magnetic, is described. Several tests and measurements have been conducted both on DNA and antibodies proving that the methodology is effective and the obtained results were promising for future developments. With such good results already obtained, one may start thinking to design and develop a diagnostic tool just like we have done at the end of Chapter 2 implementing this new technique in a portable device.

However, as clear from the experimental bench description in the previous Chapter, it is a harder task to fit the opto-magnetic setup into a portable box, with the main issues caused by the bulky electromagnet and its current driver. The coil has to be accurately placed under the SiPh chip, directly below the MRR position and at the right vertical distance, meaning that to properly work with a plug&play-like cartridges another set of 3-axis motors and an alignment step are needed, adding complexity, points of failure and costs to the design. Plus the heat generated by the working coil has to be dissipated somehow and portable devices cannot always rely on running water like the laboratory bench.

If the redesign of the coil to optimize the field concentrator tip maximizing ∇H^2 and thus the magnetic force could represent an effective solution, a more interesting, compact and with possible future outcomes can be a study towards the integration of the coil inside the SiPh chip. This research direction presents its own advantages and disadvantages.

Certainly the magnetic field generated by the integrated coil will behave differently from the one arising from the external bulky one. Intensity of ∇H^2, its angle, the force acting on MNP and biomolecules and the consequent effects on waveguide n_{eff} and the MRR resonance are parameters that need to be looked into. After simulating these aspects to understand the possible behaviours, a SiPh chip with integrated coils has been designed and produced as well as electronic board with the main role to read, drive and control the chip.

4.2.   Coils and magnetic field

The switching from an external and bulky electromagnet to a chip-integrated magnetic field generator needs some advanced considerations, in particular regarding the fabrication process needed to produce and fabricate the device. The design has to take into account the necessity of the sensing waveguide to be exposed to the environment to have a proper contact with the analyte. Then the waveguide exposure process should preserve the integrity of the magnetic generator structures.

In literature there are several examples of structures to either produce, sense or concentrate magnetic field on a chip [28, 115, 116], some with direct biosensing applications.

Coil integration
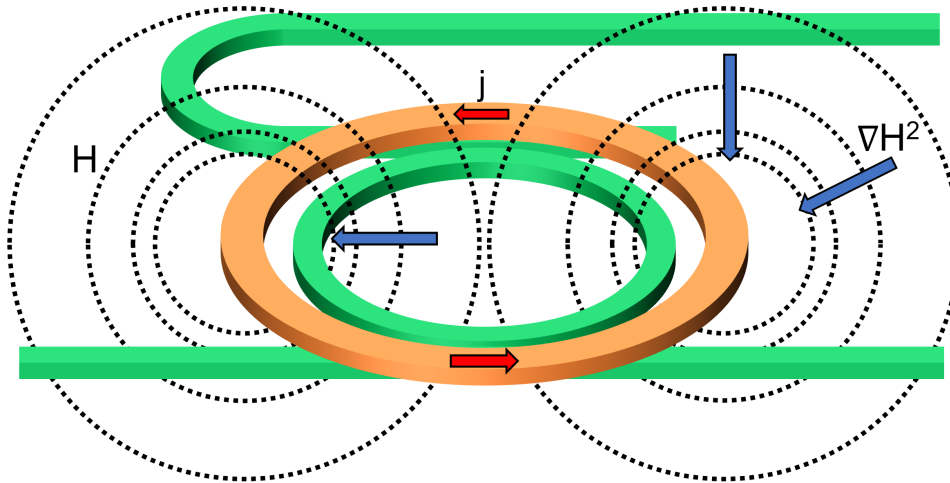
Figure 4.1: Concept: an electrical coil can be fabricated around the MRR to generate a magnetic field and to perform opto-magnetic measurements.

To obtain a magnetic field gradient on a photonic chip, and specifically in the region close to the waveguide of a MRR, we propose a structure as the one in Figure 4.1.

While the resonating optical structure is schematically the same as the one used in the
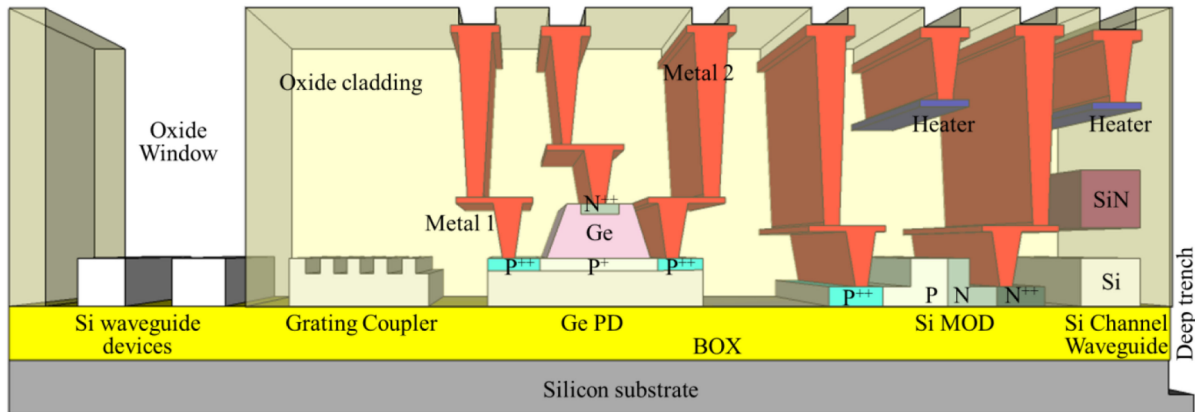
Figure 4.2: View of standard SiPh MPW flow cross-section from AMF foundry. Common elements such as waveguides, phase shifters, photodiodes and gratings are shown. From [93].

previous Chapters, it is surrounded by a metal coil that creates the magnetic field. The close proximity of the coil to the waveguide helps in increasing ∇H^2, but a gap has to be maintained to keep the sensors surface free to collect the target molecules and to avoid damaging the structure during the waveguide exposure process. The magnetic field generated by a current circulating in the coil permeates the area surrounding the MRR, in particular generating a vectorial ∇H^2 directed towards the coil itself.

The design process of the optical and magnetic structures needs to take into consideration that most wafer foundries allow a limited design choice, mostly to guarantee an up to the standards quality in fabrication.

The available design choices in MPW wafers can be even more limited since many customers are willing to fabricate on the same wafer. Each with a variety of designs with possibly their own peculiarities, they can jeopardize the production quality in case too many different fabrications steps are required, with the risk of increasing the error rate. An example of MPW stack cross section is reported in Figure 4.2. Therefore, each foundry provides to customers a set of files and rules to help in the design. Building blocks are for the most common structures, they are being optimized and are most likely guaranteed to work as expected. The Process Design Kit is a set of files and instructions containing all the needed information about the design constrains, the stack and the production process of the wafer.

After general considerations, we imagined different simple structures that could generate a magnetic gradient in the nearby of the MRR. To maintain a realistic approach, only most plausible geometries are analysed. However, we believe that the integration of magnetic

concentrators, magnetic materials or others passive or active technologies can enhance the effect and push forward the advance of an opto-magnetic integration.

Five simple proposed geometries are illustrated in Figure 4.3, in which the cross section is shown.
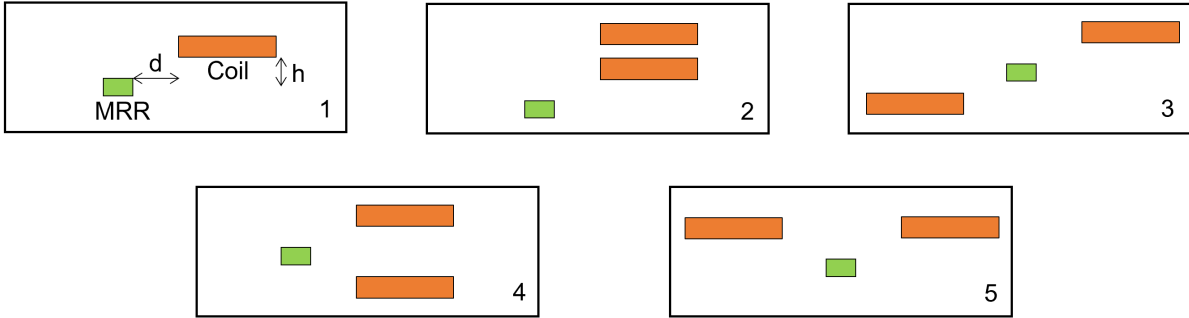
Figure 4.3: Several proposed integrated structures. First and second might be the easiest to be fabricated.

Regarding the elements placing, i.e. the optical MRR and the electrical coil for magnetic field generation, the structures follow general guidelines for fabrication processes.

- Structure #1 is the simplest among the proposed collection and it is identical to the conceptual image in Figure 4.1. Here a metal coil with a single turn is built outside of the MRR with a larger radius and placed at a different vertical level, as usually done for metal layers.

- Structure #2 adds some complexity to structure #1, placing a magnetic coil with two turns. Two-metals stacks are commonly found in foundries capabilities, so a multiple turns coil do not pose a hard challenge.

- Structure #3 however, with a two different turns coil, increases the fabrication requirements since a metal level is supposed to be below the waveguide level. This forces the process to be strongly adapted to the specific need, either depositing the metal and then fabricating the waveguide or etching the substrate to create a well in which the metal strip is deposited. Being inside the MRR, the lower coil has to cross the ring in order to be connected to the electrical routing and doing it without creating strong optical losses it may require some additional effort.

- Structure #4 uses the same concepts of the two previous structures: a two turns coil external to the MRR with the metal levels both higher and lower than the guiding material.

- Structure #5 presents both the turns of the coil higher than the waveguide, one in the inner side of the MRR and one in the outer. Like in structure #3, design and fabrication must take into account how to properly bring the electrical connection to the smaller metal strip without damaging the MRR functionalities.

Magnetic field gradient simulations

Once the general geometries have been decided, to find the ones that could perform better as biosensor element it was necessary to perform some calculation. In particular numerical simulations have been conducted to find the best solutions in terms of gradient of magnetic field squared ∇H^2 on the MRR surface.

To give the correct dimensions to the components we decided to use some fixed values. The MRR have been created to have a silicon channel waveguide, with the sectional dimensions for this platform to be the classical 500 nm width and 220 nm high. A silicon platform was chosen because we want to create a CMOS compatible biosensor to favour the mass production at low cost, being it possible to be produced in a large number of foundries. The channel waveguide, with its ability to support both TE and TM modes, was chosen since the latter polarization is notoriously more sensitive to the cladding refractive index, so more suited to sensing applications. The MRR dimensions have been kept from the previous Chapters, so $R_{MRR} = 40\,\mu m$.

To fix some more variables, we decided the metal layers thickness dimension and their vertical position h with respect to the silicon since metal layers are usually fixed by the foundry rules.

The variables to be optimized are the width of the coil turns and their radius. However, provided that the metal strip and MRR are close together, the width of the coil has a very little impact on ∇H^2, so the optimization process lead us to work by changing just the radius for the different structures.

The numerical simulations have been performed in COMSOL Multiphysics. Each structure have been modeled with an Al coil buried in SiO_2 with various dimensions and a Si ring. The metal layers have been fixed to the values that AMF foundry used for their customers MPW runs.

We simulated the effect of a 100 mA current circulating in the metal strip. In the near proximity of the coil, ∇H^2 is expected to get more intense so higher attractive magnetic force can be obtained. The area of interest is the waveguide: being its surface smaller than the typical MRR-coil distance, the gradient intensity as well as its direction can be considered constant across that area.

The vector ∇H^2 is expected to be different from the one generated by the external coil in

Chapter 3. With the use of the bulky electromagnet placed below the chip, ∇H^2 and the magnetic force F_{mag} were uniformly vertical, pointing towards the surface. Since the coil's turn is on the side and just few hundreds nm higher than the waveguide, this integrated solution causes the F_{mag} to be mostly horizontal. Increasing the horizontal distance between the MRR and the metal, the angle is expected to approach zero.

From the simulations, it turned out that the coils that are easier to fabricate may be also the best in terms of performances, allowing us to optimize the dimensions focusing our analysis on the two simplest structures (#1 and #2). During the fabrication and chip processing steps described in Chapter 2, we noticed that we could reliably obtain a litography and etching accuracy down to few µm. In order to be sure to expose the waveguide and avoid damaging the coil, a proper gap between the two objects has to be defined: a larger gap will guarantee a chip processing with little failures and more robust to imperfections, but it will decrease the intensity of the magnetic force in the waveguide region.
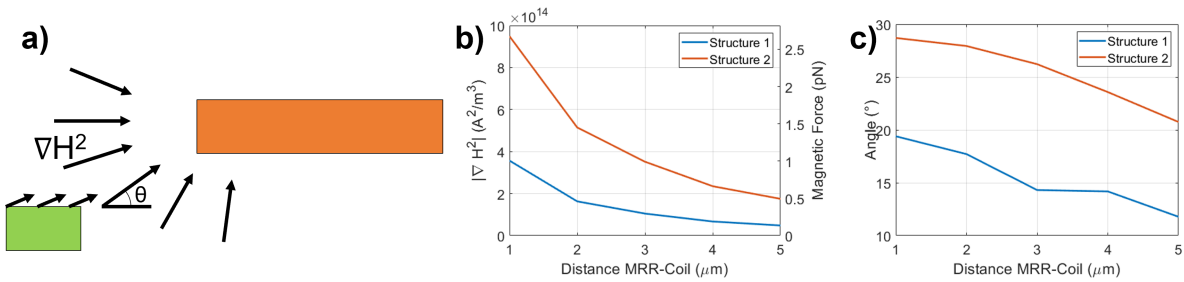
Figure 4.4: Study of ∇H^2. Intensity and angle are plotted for the most promising structures, considering different gaps between MRR and coil.

In Figure 4.4a, we show a schematic of the gradient of the squared magnetic field in the waveguide position. The gap separating the metal coil from the MRR ranges from $1\,\mu m$ to $5\,\mu m$, to study the dependence of the vector from the distance for the two selected structures.

In Figure 4.4b, $|\nabla H^2|$ is plotted. For a minimum gap of $1\,\mu m$, the highest value is reached, with the double-turns structure generating almost 10^{15} A^2/m^3, while the simplest one stops at $3 \times 10^{14}\,A^2/m^3$. Increasing the distance between the optical and the electrical parts, $|\nabla H^2|$ decreases down to one fifth of the higher value when at $5\,\mu m$ distance, so $1.8 \times 10^{14}\,A^2/m^3$ and $5 \times 10^{13}\,A^2/m^3$, respectively. As comparison, the calculated value for ∇H^2 obtained with the external electromagnet reached $10^{12}A^2/m^3$ when $2\,A$ where applied and a 10 times lower value, roughly $10^{11}A^2/m^3$, in measurement conditions. So the integrated solution theoretically offers a magnetic force that is at least 50 times stronger, all due to the close proximity between the sensing area and the magnetic field generator.

This is directly reflected to the magnetic force that can be generated on the MNP, in this case in the pN range.

The direction of ∇H^2 is plotted in Figure 4.4c and is expressed in terms of degrees with respect to the horizontal axis. As expected, with the bigger magnetic structure the magnetic force has a larger deviation from the horizontal direction, but will asymptotically converge to 0° for larger distances. The same concept applies to the simple structure, which starts from 20° and decreases for larger gaps.

The ∇H^2 vector direction is completely different from the one created by the external coil, so the effects of such force on the MNP motion need to be considered to evaluate the MRR resonance behaviour.

4.3. Magnetic force effect

We saw how an integrated coil can produce a magnetic gradient that our application wants to exploit to generate a magnetic force on a magnetic nanoparticle bound to a biomolecules system. The behaviour of molecules subjected to external forces is a complex topic, so we will use a simplified model to estimate the motion.

The force acting on the MNP can be directly estimated from Equation 3.10:

$$\mathbf{F}_{mag} = \frac{1}{2}\mu_0 \Delta\chi V \nabla(H^2)$$

If we use the same 130 nm diameter MNP used in the previous Chapter, the volume is $V = \frac{4}{3}\pi R_{MNP}^3 =$ 1.15 × 10^{-21} m^3 and the magnetic susceptibility $\Delta\chi = 3.9$. With these values we can estimate a conservative, i.e. 5 µm-gap, magnetic force $|F_{mag,1}| =$1.5×10^{-13} N $= 0.15$ pN for the first structure and $|F_{mag,2}| = 0.5$ pN for the second one, with the possibility to reach up to $|F_{mag,2,max}| = 2.5$ pN.

DNA bending

This force acts on the MNP which is bound to a biomolecule complex, producing a displacement of the system. The magnitude of the displacement strongly depends on the bending and elastic properties of the molecule under test. How the probe is attached to the surface, atomic and molecular bonds between probe and target, overall dimensions, rest position, number of molecules bound to the same MNP are just some of the parameters that affect the displacement we want to detect.

To have an idea about the MNP movement we would need a correct comprehension on the molecule bending mechanics. The topic, however, is so vast and complex [117–122]

that would fall out of our scope. Nonetheless, in literature the mechanics of a particular molecule is widely studied: DNA chains [123–128].

Being already familiar with these molecules after the measurements reported in Chapters 2 and 3 we can keep working on oligonucleotides. Plus, we can add to the experience already acquired on 60 base pairs DNA chains a simplified model of the short DNA bending mechanics as described in [129].

A DNA chain is a polymer [130] and for this kind of structures a persistence length ξ_p can be defined. It can be easily described by

$$\xi_p = \frac{\kappa_f}{k_B T} \tag{4.1}$$

in which κ_f is the flexural rigidity (or stiffness). The persistence length indicates the length of the polymer at which the thermal energy causes a decorrelation between the tangents of the filament. So if a polymer is much longer $L >> \xi_p$, it will be in a random and convoluted shape dominated by thermal motion and for which a statistical approach (as the worm-like chain) should be used to describe it. For shorter chains $L << \xi_p$ the polymer resembles a relatively straight and elastic rod, able to maintain its shape. For DNA the persistence length results in $\xi_p \simeq 50 - 70\text{nm}$, and corresponds to a chain of 150-200 base pairs, so the 60-bp DNA strands used in the previously described experiments possess an elastic behaviour.

To bend DNA chains at smaller scales with respect their ξ_p, it is necessary to provide an energy that is larger than the thermal one. A simple estimation for the energy required to bend a ΔL long oligo chain over an arc with radius R_{bend} is given by

$$\Delta E_{bend} = \Delta L \frac{\kappa_f}{2R_{bend}^2} = \Delta L \frac{k_B T \xi_p}{2R_{bend}^2} \tag{4.2}$$

With this information about the energy, it is possible to estimate the force needed to bend the segment at that radius:

$$F_{bend} = \frac{k_B T \xi_p}{2R_{bend}^2} \tag{4.3}$$

As example, the bacteriophage virus has a capside radius of $29\,\text{nm}$ and its DNA is looped multiple times inside it: to fit into that reduced space a force of $F_{bend} = 0.12\,\text{pN}$ is required. Alternatively we are able to retrieve the bending radius of the DNA segment when an external force is applied:

$$R_{bend} = \sqrt{\frac{k_B T \xi_p}{2F_{bend}}} \tag{4.4}$$

as schematically shown in Figure 4.5a.
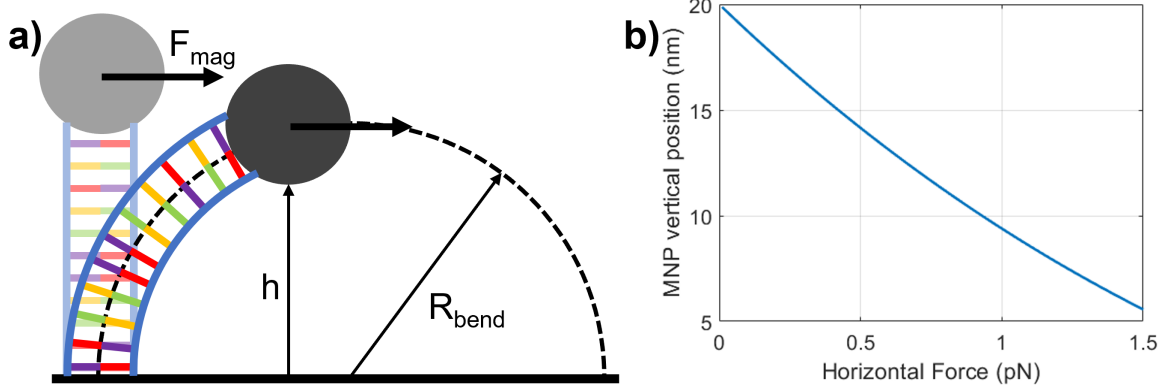
Figure 4.5: Under the effect of an external perpendicular force the DNA bends over a curvature. The vertical distance from the MNP to the surface depends on the force.

With our integrated coils we estimated that a magnetic force can be applied horizontally with respect to the waveguide surface. Magnitudes were estimated to be in the pN range, so comparable to the forces needed to bend the DNA over a curvature radius of several tens of nm. We can approximate that an horizontal force keeps the model valid if $\mathbf{F}_{mag}$ and the DNA rod are nearly perpendicular, meaning that the bending radius is large and the molecule is just slightly bent with respect to the rest position. Thus, the horizontal magnetic force can bend the DNA and change the vertical position of the MNP according to Figure 4.5b.

We now have an approximated model for the DNA bending that let us estimate the vertical position of a MNP depending on the magnetic force that is being created by coils integrated in a chip.

The vertical position of a label allows us to calculate the behaviour of a MRR resonance. Adapting the numerical simulations performed in Chapter 3, Figure 4.6a shows the cross section of the channel silicon waveguide with the TM optical mode perturbed by the MNP placed at various vertical distances.

Evaluated as in the previous Chapter, the resonance shift is calculated for a single MNP changing its vertical position in Figure 4.6b both with TE and TM modes.

Figure 4.6c finally merges bending considerations with the simulations results and we obtain the expected resonance shift $\Delta\lambda$ with respect the magnitude of the applied magnetic force F_{mag}. From the plots, we see that with just $F_{mag} = 0.15\,\mathrm{pN}$, a magnitude achievable also with the simplest magnetic coil structure, we can produce a 2 nm vertical displacement of the MNP from 20 nm (rest position) to 18 nm (bent chain). The nanoparticle then affects the electromagnetic field in the waveguide and causes the MRR to shift its
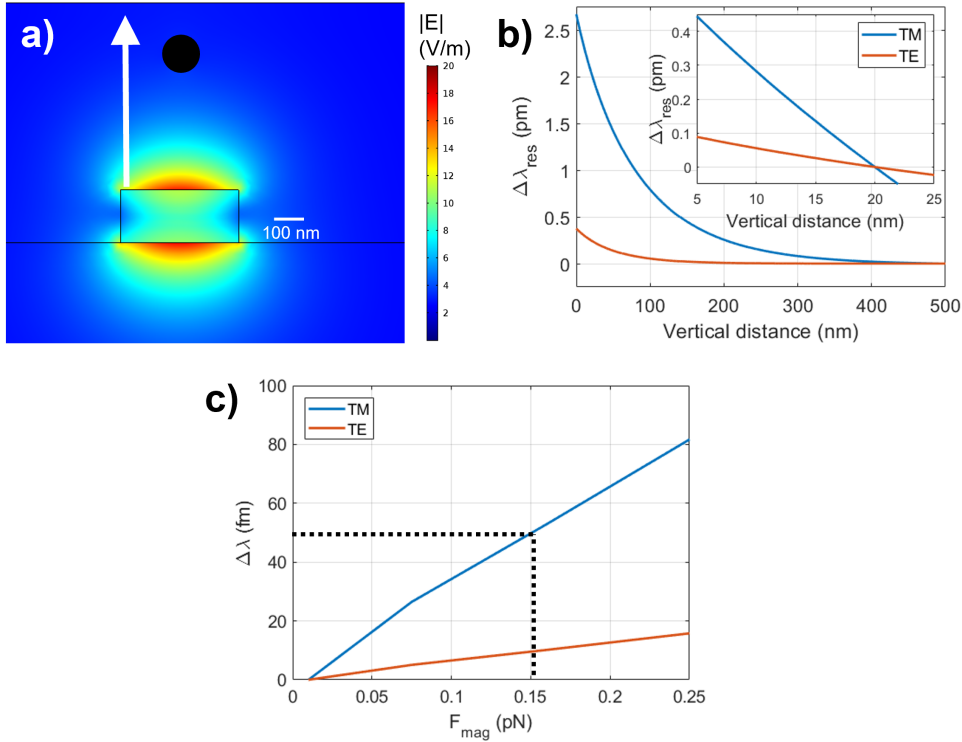
Figure 4.6: From magnetic force to wavelength shift. (**a**) COMSOL simulation of the MNP at several distances from the channel waveguide with TM mode. (**b**) Resonance shift for both TM and TE with respect to the MNP vertical distance. Inset: wavelength shift with respect a 20 nm starting position. (**c**) From ∇H^2 we evaluated the DNA bending radius, that gave us the vertical displacement of the MNP and thus the resonating wavelenght shift of the MRR caused by one MNP.

resonating wavelength by 50 fm when TM mode is excited.

A resonance shift of few tens of fm feels hardly perceivable for detecting techniques that just measure the transfer function shift by repeatedly scanning it. However, in this work we described two approaches that can detect such small amount of resonating change: the opto-magnetic technique with wavelength scan and with the feedback loop for resonance tracking. Both methods could be implemented to detect a single oscillating MNP attached to a DNA strand.

4.4. SiPh chip design

The consideration of the previous section were promising to move towards an efficient and compact biosensing platform that integrated the opto-magnetic technique. We had the possibility to participate in an industrial MPW run, so we decided to exploit this great

chance to test our ideas.

Being the MPW on a silicon platform, we could implement many of the studied concepts. In particular we focused on some aspects that we believed could help the quality of the project:

- we chose the waveguide to be in a channel structure, in order to being able to excite the TM mode, which we saw it is more sensitive to the cladding modifications;

- the chip should have integrated photodiodes to allow a low noise reading of the light intensity amplitude, to obtain a clean signal for resonance tracking measurements;

- the integrated coils should have different structures, possibly the best-showing performances analyzed previously

- the gaps between the waveguide and the metal strip of the coils should be minimized, but still should leave room for post-processing tolerances;

- the MRR should have a FSR similar to the ones previously used on the STMicro-electronics chips, so we could use the same experimental setup for the tests; the MRR should also be in add-drop configuration to allow the feedback loop to be used;

- the whole chip footprint should be the same of the STM ones, so to use the same fluidic cell for the tests.

Due to MPW constraints coming from other projects on the same wafer, we could not access some features that would have really helped. Slot waveguides, known for the high sensitivity, were not possible on this run. For fabrication requirements on other designs it was also not possible to have the MRR waveguides exposed by the foundry. This forces us to post-process the chips, increasing the possible failure rate to obtain working devices.

Taking into consideration what we wanted to achieve and the limitations, we designed the chip to maximize the obtainable performances.

The two metal layers thicknesses and positions inside the stack above the silicon are parameters fixed by the foundry and should be kept confidential, so we limit our description to the design we used.

The waveguide has been designed to have a channel cross section with dimensions $500\,\mathrm{nm}$ width and $220\,\mathrm{nm}$ wide. In the middle of the chip we placed four optical MRR each with a magnetic structure, either the previously named #1 or #2, as shown in Figure 4.7:

a) the first MRR has a radius of $40\,\mathrm{\mu m}$ and a coupler gap of $250\,\mathrm{nm}$. The magnetic coil is formed by a single turn of the lower metal layer to recreate structure #1. The
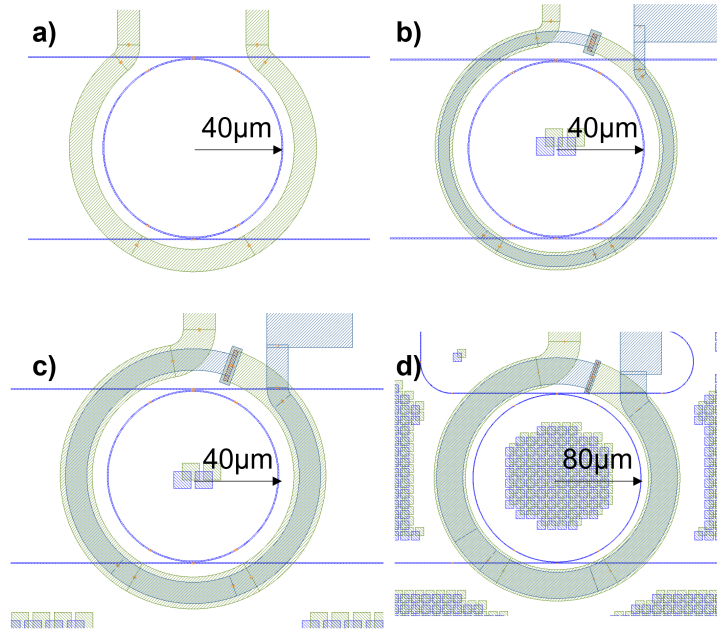
Figure 4.7: Designs of the 4 MRR with their relative magnetic structures.

metal strip is 10 μm wide and the inner radius measures 45 μm, leaving a 5 μm gap to deal with etching tolerances.

b) the MRR has the same radius and a coupler gap of 300 nm. The coil has two turns to create structure #2: the width of the lower one is 8 μm, while the upper measures 5 μm. The distance to the MRR-coil distance is 7 μm.

c) the 40 μm radius MRR with couplers gap of 350 nm is surrounded by a two-turns coil. The metals widths are 15 μm and 10 μm, leaving a 7 μm separation from the MRR.

d) the MRR is larger, with a radius of 80 μm, doubled with respect to the others. A 400 nm gap separates the waveguides in the couplers, while the metals are 7 μm away and their widths are 30 μm and 25 μm.

The designed structures, due to fabrication constraints, are slightly different from the simulated ones in the previous section, but concepts and shapes are maintained and all the considerations on the generated magnetic force and expected resonance shift are still valid.

Finally, the fabricated chip is shown in Figure 4.8. It has a footprint of $5 \times 6\text{mm}^2$ and in the middle the four sensing structures are present with the MRR surrounded by the coils devoted to generate a magnetic field to obtain a magnetic force on the MNP proportional to ∇H^2. The photodiodes are integrated at each optical output, and the PD are connected

to the electrical pads for the electronic readout of the signals. On the bottom-left, four optical couplers are used to inject the light into the waveguides that bring the field to the resonating cavities.
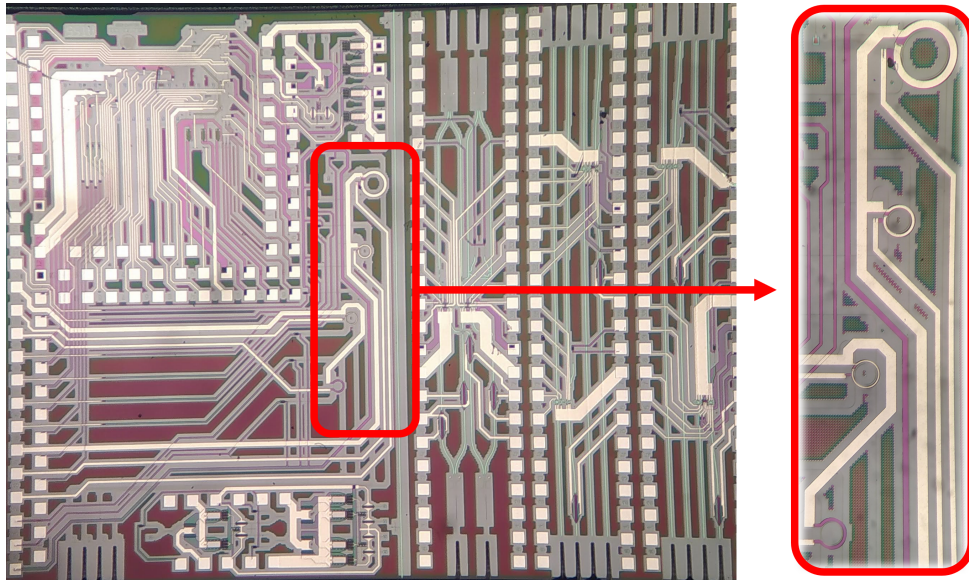
Figure 4.8: Opto-magnetic integrated SiPh chip. In the detail the four MRR with magnetic generators.

Basic tests have been performed on the chip, mostly on the coil structures to understand their electrical properties. The resistances have been all measured in a range between $5\,\Omega$ and $7.5\,\Omega$, guaranteeing a low thermal dissipation. Then, we tested the maximum current that can be injected in them by slowly increasing it until the structure burn. We found that the coil of the second MRR burned at $300\,\text{mA}$, leaving us plenty of current range to drive them during the opto-magnetic experiments. The last test performed wanted to measure the coil responses at higher frequencies, but as expected we got a flat response up to $10\,\text{kHz}$, well beyond our $\sim100\,\text{Hz}$ working point.

The close proximity of the coils to the waveguides suggests that thermal effects can be seen in the outcome of the measure. However, the electrical routes do not heat up as thermal phase shifters, commonly known as heaters, being not optimized for that role. A second reason to imagine a reduced thermal effect is that the waveguide is covered by fluid, most likely flowing, while the magnetic field generator is buried in SiO_2. To conclude, just like we have seen in the previous Chapter, the result of an opto-magnetic measure is the comparison between a sensing and a reference transductor: being the two sensors exactly the same, the thermal effects are comparable and thus the only difference in the outcome is caused by the presence of biological material and oscillating MNP.

4.5.　Experimental setup

The realization of the new photonic chip forced us to design a new control electronics to meet the needs of the integrated opto-magnetic platform.
The integrated photodiodes need to be accurately read and the coils need to be driven in terms of current and frequency to obtain a proper opto-magnetic measurement.

A new photonic board has been designed to accomodate the new chip, while the old fluidic cell could be fixed on the top to perform liquids measurements and full experiments, like in Chapters 2 and 3. The major differences with respect to the previous version involve the electrical routing, since there are now 8 photodiodes to be read and 4 coils to be driven. The connection is maintained flat, in PCI standard shape, to easily plug the connector that enable the communications between the photonic board and the control electronics.

The scheme of the main electronic board is in Figure 4.9. It is connected both to the PC with the use of the DAQ interface and with the chip on the photonic board. To read
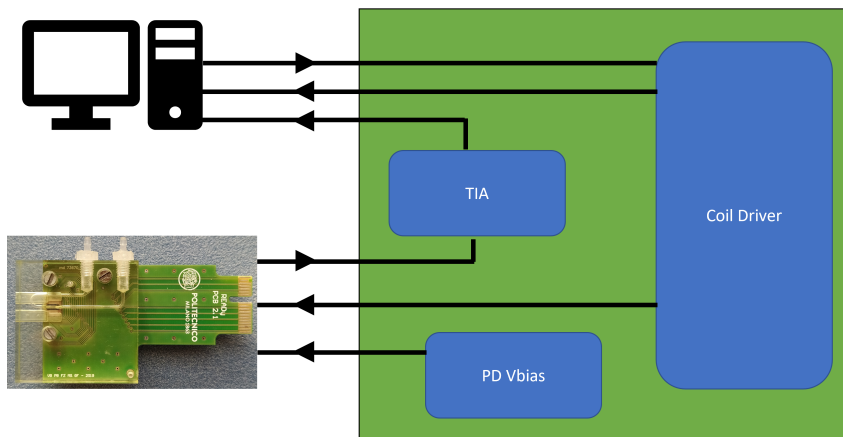
Figure 4.9: Blocks scheme of the electronics needed to drive the chip and perform the measurements.

the light intensities, an operational amplifier sets the PD in reverse bias condition. The photocurrent is directed towards a series of Trans-Impedance Amplifiers with logarithmic gain that convert the current generated by the light in the photodiodes into a voltage to be read by the DAQ and the Lock-In Amplifier.
The stage devoted to drive the coils receives an external signal from the DAQ, usually a sinusoidal one to create a time-dependent magnetic force on the MRR. An operational amplifier in buffer configuration injects the current into the coils after an Instrumentation Amplifier retrieves the current flowing in the line, converts it to voltage and sends it to the DAQ for accurate control on the magnetic field generators.

The board production suffered from the widely known chip shortage, and after being delayed few times we decided to change some integrated amplifiers. Instead of an amplifier with 250 mA maximum current for driving the coils we had to mount a 26 mA maximum current chip to avoid other delays. It is unfortunate that to reach a coil current up to 100 mA as in the simulations we will need to wait for the other components to return available on the market and mount them on the electronic board, but this current limit will be enough to test the platform functionalities.
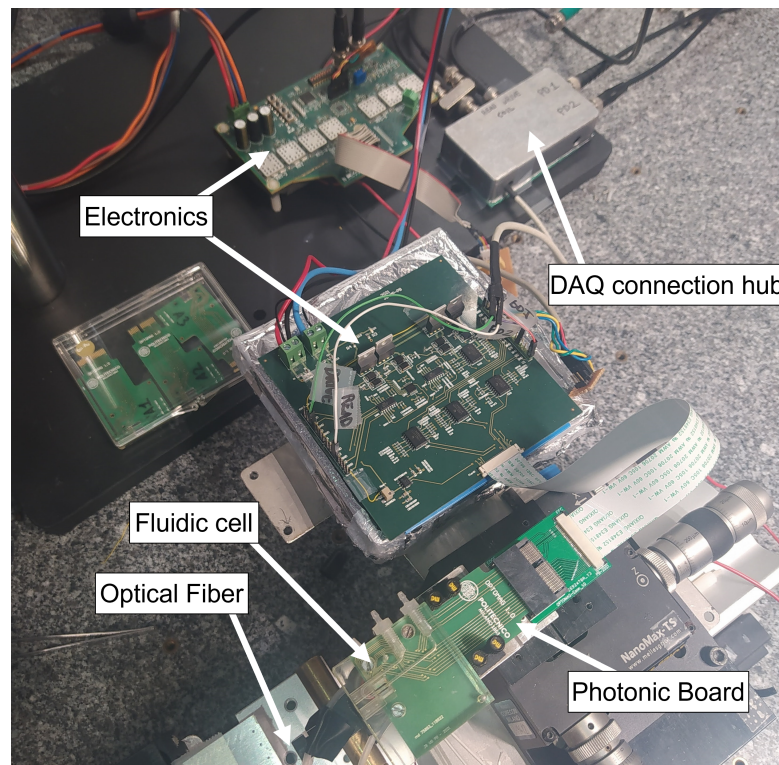
Figure 4.10: Photo of the bench setup for the integrated opto-magnetic platform.

The final setup is showed in Figure 4.10. At the bottom of the picture, an optical fiber is in position to be edge-coupled to the silicon microchip, glued and wire bonded to the new photonic board that is holding the fluidic cell. A connection board with flexible flat cable transfers the electrical signals between the photonic board and the main electronic board. A connector box, on the upper right, intermediates the signals coming to and from the DAQ and route them towards the control electronics. Here the sinusoidal voltages are amplified to drive the coils and the photodiodes' currents are converted into voltages and sent to the PC and to the LIA for demodulation. A small interface have been produced to let the control electronics to be connected to the Elite board used in the previous Chapters. In contrast to the classic opto-magnetic setup, here there is no need for the bulky electromagnet and its driver to be present, showing a simpler system and paving

the way to a leaner assembly for prototyping.

This experimental bench setup, completed with the laser source, its drivers and a custom LabView control software, allows us to perform opto-magnetic measurements using the same established approaches already described. Opto-magnetic biosensing with wavelength scan or feedback-loop methods are now possible with a silicon photonics chip that efficiently integrates both optical and magnetic structures to enhance even more the capabilities of these technologies.

Sadly, the delays in the tests of the semiautomatic diagnostic device presented in Chapter 2 and the Dengue virus positive human samples (see Appendix A), the issues in fabrication and material supplying for the electronic board and some technical difficulties encountered during the new chips post-processing to expose the waveguides led to defer sensing tests on the new platform. At the time of writing, proper tests with biomolecules on the integrated opto-magnetic platform have not been performed yet.
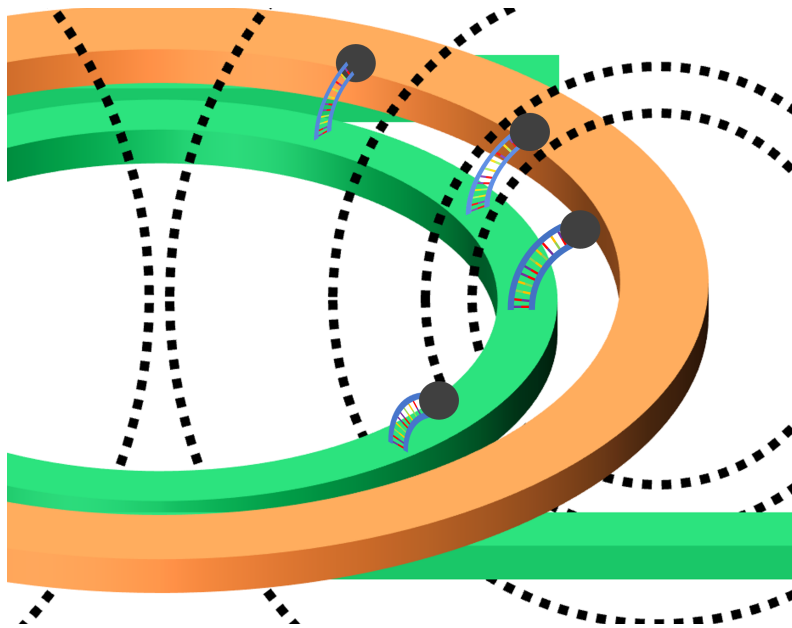
Figure 4.11: Representation of the DNA and MNP wobbling on the MRR, under the influence of the magnetic force generated by the integrated coil.

We strongly believe that the opto-magnetic technique can improve the performances of biosensing and diagnostics in optical platforms and that a big step towards a wider adoption is set to be performed by the integration of the optical and magnetic parts, which is a fundamental passage to have a simplified system with less bulky components, cheaper to be produced and easier to work with and to manage.

5 | Conclusions

This thesis describes how integrated photonics, and in particular microring resonators, can be implemented in a biosensing system to detect analytes of various species. The work focused on the development of a diagnostic methodology and system that could find their way into hospital and clinical laboratories, but still considering a possible future in which the biosensor reaches the population in a disposable and low-cost device.

The system we developed merges knowledge from different research field: optics, biochemistry, magnetism, electronics and fluidics.

The sensing element is an optical microcavity on a silicon photonics platform, which is CMOS compatible thus it can be easily fabricated in industrial and commercial electronics foundries. Sensitive to refractive index variations on the waveguide cladding, the microring resonators change the resonance frequency according to the molecule quantity immobilized on the surface, giving a direct information on the presence and concentration of a particular analyte in the tested sample.

The molecules to be detected were DNA strands for a model detection to prove the capabilities of the system and then human antibodies to show a clinically focused application. The sensors functionalization were performed at our research partners laboratories by using copolymer coating and probe molecules microspotting: this technology is easy, cheap, scalable and adaptable to many different analytes and molecules of various genre.

Instead of dropping the biological sample on the sensor, an easy-to-use diagnostic device has to deal with the sample management with little to no intervention from the user. A fluidic system is therefore used for the process. The fluidic cell puts the sample in contact with the sensor's surface, while a collection of programmable valves and syringe pump moves the liquids at desired flux rate, with desired time and automatically creates the solvents and buffers sequences needed for the whole biochemical process to be efficiently performed.

To improve the capabilities of the detection, a new active labelling technique was developed and implemented. Making use of magnetic nanoparticles in the assay, magnetic fields have been created by coils. Coil shapes have been studied to find the best solution for our application. Bulky coil core shape has been chosen to optimize the magnetic force, while

the integrated solution needed a study to find the best trade-off between a strong magnetic force and a structure which is robust against fabrication and chip post-processing imperfections.

The electronics system close the loop, connecting all the different blocks. A custom software, through an input-output PC interface, controls all the elements by fixing or scanning the laser wavelength, starting the programmable fluidic protocol, switching on-off the electromagnet and controlling the voltage intensity and frequency, reading the photodiodes output and performing the calculations needed to clearly understand the outcome of the measurements.

The system has been used to measure the hybridization process of biomolecules, to detect and return a quantitative response of a biorecognition and binding.

First, a label-free detection has been performed, measuring the resonance shift determined by the target DNA binding to the probe complementary chain fixed on the surface. Dealing with low refractive index changes, the signals were low and easily covered by noise. On the DNA model we reached a detectable concentration between $1 - 100$ nM.

A passive labelling approach was used to enhance the resonance shift by using iron oxide nanoparticles. The high impact of such corpuscles on the electromagnetic field produced in the microring a resonance shift one order of magnitude larger, leading to an improved detection limit, $0.1 - 1$ nM.

These concepts where used to design, assemble and test a prototype diagnostic device to be used in hospital laboratories on human samples. The machine is semiautomatic, easy to use, portable and with a graphical user interface adapted to non-expert users. Testing were performed with human plasma samples from patients infected by Dengue virus.

To lower the detection limit we studied and developed an active labelling technique, here named opto-magnetic. With the use of the magnetic nanoparticles already used as labels and time varying magnetic fields, we impose a bouncing behaviour to the particles bound to the molecules above the sensors. The consequent microring transfer function oscillation causes at the output a modulation on the optical power, which is demodulated by a lock-in amplifier. The demodulated amplitude, together with the information on the transfer function shape, returns the actual resonance oscillation entity induced by the wobbling nanoparticles. Thanks to the lock-in technique, with respect to the previous system the limit of detection is improved by at least another order of magnitude: in the range $10 - 100$ pM for the robust scanning method and below 10 pM for the fast feedback tracking method, which shows great improvement potential.

The advantage of this approach is not only in the detection limit. The time required to acquire an opto-magnetic measurement ranges from few minutes to just ten seconds,

depending on the method, a real advantage for the operators. Plus, the interrogation is performed after the hybridization so there is no need to track the resonance position as it evolves during the molecular recognition. Without this constrain, the hybridization can be performed in the conditions that favour more the molecular binding, e.g. temperature, humidity, fluidic flux or mechanical agitation, without worrying about the optical alignment. This allows to potentially increase the binding efficiency, improving even more the detection at low concentrations.

The last step of our work was focused on studying a possible integration of the opto-magnetic technique. A microchip containing both the optical microring and the magnetic coil would radically ease the prototyping process, while improving measurements repeatability, with better signals and lower power consumption. Different coil geometries were proposed and the consequent magnetic force were applied to a model for molecule bending. The molecule displacement has been used to obtain an estimation of the expected wavelength shift of the microring resonance. From the calculations results, we expect with this platform to improve the limit of detection even more and with an easier to use measurement setup.
The system have been designed and fabricated, with the fluidics for liquid control and the electronics for coil driving and photodiodes reading ready to be exploited to perform new biosensing measurements.

Future developments on the system and on the magnetic part will take into account the outcome of the new integrated chips tests. We strongly believe that the opto-magnetic technique could be a real asset in several assays and that with this work the optical biosensing framework acquired a niece yet important piece.
Possible improvements could be the use of new magnetic field generators or concentrators, or the use of waveguides more suitable for biosensing, e.g. slot waveguides, or changes in the devices moving from microring resonators to Mach-Zehnder interferometers or surface plasmon devices.

Choices on the technology could be made, but biosensing and healthcare are topics that gain importance year by year.
Research in these fields is strong and fast and it is our duty to keep up the pace to have updated biosensing systems available, filling the gap between the fundamental research and the developed devices that could someday reach the market and improve everybody's quality of life.

Bibliography

[1] Piero Borga et al. "Active Opto-Magnetic Biosensing with Silicon Microring Resonators". In: *Sensors 2022, Vol. 22, Page 3292* 22.9 (Apr. 2022), p. 3292.

[2] Paola Piedimonte et al. "Differential Impedance Sensing platform for high selectivity antibody detection down to few counts: A case study on Dengue Virus". In: *Biosensors and Bioelectronics* 202 (Apr. 2022), p. 113996.

[3] World Health Organization, ed. *Global expenditure on health: public spending on the rise*. Geneva, 2021.

[4] K. C. Sekhar and S. S.C. Chakra Rao. "John Scott Haldane: The father of oxygen therapy". In: *Indian Journal of Anaesthesia* 58.3 (2014), p. 350.

[5] Michael A Lang and Alf O Brubakk. "The Haldane Effect". In: ().

[6] Varnakavi. Naresh and Nohyun Lee. "A Review on Biosensors and Recent Development of Nanostructured Materials-Enabled Biosensors". In: *Sensors 2021, Vol. 21, Page 1109* 21.4 (Feb. 2021), p. 1109.

[7] Parikshit Pratim Sharma, Daniela Petti, and Riccardo Bertacco. "Magnetoresistive and opto-magnetic biosensors". PhD thesis. 2017.

[8] Nicola Peserico. "Integrated Optical Platform for Biosensor Application". PhD thesis. Politecnico di Milano.

[9] Pavel Damborský, Juraj Švitel, and Jaroslav Katrlík. "Optical biosensors". In: *Essays in Biochemistry* 60.1 (June 2016), pp. 91–100.

[10] Haleh Nazemi et al. "Advanced Micro- and Nano-Gas Sensor Technology: A Review". In: *Sensors 2019, Vol. 19, Page 1285* 19.6 (Mar. 2019), p. 1285.

[11] Andreas Hänsel and Martijn J.R. Heck. "Opportunities for photonic integrated circuits in optical gas sensors". In: *Journal of Physics: Photonics* 2.1 (Jan. 2020), p. 012002.

[12] Nunzio Cennamo et al. "A Molecularly Imprinted Polymer on a Plasmonic Plastic Optical Fiber to Detect Perfluorinated Compounds in Water". In: *Sensors 2018, Vol. 18, Page 1836* 18.6 (June 2018), p. 1836.

[13] Saddam Hussain and Soo Young Park. "Sweat-Based Noninvasive Skin-Patchable Urea Biosensors with Photonic Interpenetrating Polymer Network Films Integrated into PDMS Chips". In: *ACS Sensors* 5.12 (Dec. 2020), pp. 3988–3998.

[14] R. D. McDowall. "Sample preparation for biomedical analysis". In: *Journal of Chromatography B: Biomedical Sciences and Applications* 492.C (Aug. 1989), pp. 3–58.

[15] Jeanette C. Roberts and David J. Francetic. "The Importance of Sample Preparation and Storage in Glutathione Analysis". In: *Analytical Biochemistry* 211.2 (June 1993), pp. 183–187.

[16] Janusz Pawliszyn. "New directions in sample preparation for analysis of organic compounds". In: *TrAC Trends in Analytical Chemistry* 14.3 (Mar. 1995), pp. 113–122.

[17] Kevin D. Clark, Cheng Zhang, and Jared L. Anderson. "Sample Preparation for Bioanalytical and Pharmaceutical Analysis". In: *Analytical Chemistry* 88.23 (Dec. 2016), pp. 11262–11270.

[18] Kirsty Phillips, Nicola McCallum, and Lindsey Welch. "A comparison of methods for forensic DNA extraction: Chelex-100® and the QIAGEN DNA Investigator Kit (manual and automated)". In: *Forensic Science International: Genetics* 6.2 (Mar. 2012), pp. 282–285.

[19] Leona M. Schmidt-Speicher and Kerstin Länge. "Microfluidic integration for electrochemical biosensor applications". In: *Current Opinion in Electrochemistry* 29 (Oct. 2021), p. 100755.

[20] Jinhong Guo, Xiwei Huang, and Xing Ma. "Clinical identification of diabetic ketosis/diabetic ketoacidosis acid by electrochemical dual channel test strip with medical smartphone". In: *Sensors and Actuators B: Chemical* 275 (Dec. 2018), pp. 446–450.

[21] Maximilian Grösche et al. "Microfluidic Chips for Life Sciences—A Comparison of Low Entry Manufacturing Technologies". In: *Small* 15.35 (Aug. 2019), p. 1901956.

[22] Kiran Raj M and Suman Chakraborty. "PDMS microfluidics: A mini review". In: *Journal of Applied Polymer Science* 137.27 (July 2020).

[23] Frederick K. Balagaddé et al. "Microbiology: Long-term monitoring of bacteria undergoing programmed population control in a microchemostat". In: *Science* 309.5731 (July 2005), pp. 137–140.

[24] Joonyeong Kim et al. "Investigations of chemical modifications of amino-terminated organic films on silicon substrates and controlled protein immobilization". In: *Langmuir* 26.4 (Feb. 2010), pp. 2599–2608.

[25] James T. Kirk et al. "Multiplexed inkjet functionalization of silicon photonic biosensors". In: *Lab on a Chip* 11.7 (Apr. 2011), pp. 1372–1377.

[26] Shahrzad Forouzanfar et al. "Perspectives on C-MEMS and C-NEMS biotech applications". In: *Biosensors and Bioelectronics* 180 (May 2021), p. 113119.

[27] Michael J. Schöning and Arshak Poghossian. "Recent advances in biologically sensitive field-effect transistors (BioFETs)". In: *Analyst* 127.9 (Sept. 2002), pp. 1137–1151.

[28] Francesca Milesi et al. "On-Chip Selective Capture and Detection of Magnetic Fingerprints of Malaria". In: *Sensors 2020, Vol. 20, Page 4972* 20.17 (Sept. 2020), p. 4972.

[29] Parikshit P. Sharma et al. "Integrated platform for detecting pathogenic DNA via magnetic tunneling junction-based biosensors". In: *Sensors and Actuators B: Chemical* 242 (Apr. 2017), pp. 280–287.

[30] Pierre-A. Besse et al. "Detection of a single magnetic microbead using a miniaturized silicon Hall sensor". In: *Applied Physics Letters* 80.22 (May 2002), p. 4199.

[31] Daniel L. Graham, Hugo A. Ferreira, and Paulo P. Freitas. "Magnetoresistive-based biosensors and biochips". In: *Trends in Biotechnology* 22.9 (Sept. 2004), pp. 455–462.

[32] P. P. Freitas et al. "Magnetoresistive sensors". In: *Journal of Physics: Condensed Matter* 19.16 (Apr. 2007), p. 165221.

[33] M Carmen Estevez, Mar Alvarez, and Laura M Lechuga. *Integrated optical devices for lab-on-a-chip biosensing applications*. Apr. 2012.

[34] Patrik Forssén et al. "Reliable Strategy for Analysis of Complex Biosensor Data". In: *Analytical Chemistry* 90.8 (Apr. 2018), pp. 5366–5374.

[35] Shengbo Sang et al. "Progress of new label-free techniques for biosensors: A review". In: *Critical Reviews in Biotechnology* 36.3 (Apr. 2016), pp. 465–481.

[36] Pinar Kara et al. "Label-Free and Label Based Electrochemical Detection of Hybridization by Using Methylene Blue and Peptide Nucleic Acid Probes at Chitosan Modified Carbon Paste Electrodes". In: *Electroanalysis* 14.24 (Dec. 2002), pp. 1685–1690.

[37] Matthew S. Luchansky et al. "Sensitive on-chip detection of a protein biomarker in human serum and plasma over an extended dynamic range using silicon photonic microring resonators and sub-micron beads". In: *Lab on a Chip* 11.12 (June 2011), pp. 2042–2044.

[38] Suhee Kim et al. "Ultra-sensitive detection of IgE using biofunctionalized nanoparticle-enhanced SPR". In: *Talanta* 81.4-5 (June 2010), pp. 1755–1759.

[39] S. Kubitschko et al. "Sensitivity Enhancement of Optical Immunosensors with Nanoparticles". In: *Analytical Biochemistry* 253.1 (Nov. 1997), pp. 112–122.

[40]   Thijs Wink et al. "Liposome-Mediated Enhancement of the Sensitivity in Immunoassays of Proteins and Peptides in Surface Plasmon Resonance Spectrometry". In: *Analytical Chemistry* 70.5 (Mar. 1998), pp. 827–832.

[41]   Z Guo et al. "Surface Plasmon Resonance Imaging Measurements of DNA Hybridization Adsorption and Streptavidin/DNA Multilayer Formation at Chemically Modified Gold Surfaces". In: *Analytical Chemistry* 69.24 (1997), pp. 4939–4947.

[42]   Lin He et al. "Colloidal Au-enhanced surface plasmon resonance for ultrasensitive detection of DNA hybridization". In: *Journal of the American Chemical Society* 122.38 (Sept. 2000), pp. 9071–9077.

[43]   M. A. Hayat. *Colloidal Gold: Principles, Methods, and Applications*. Vol. 14. 4. 1996, pp. 2881–2885.

[44]   Tomáš Kaláb and Petr Skládal. "Disposable multichannel immunosensors for 2,4-dichlorophenoxyacetic acid using acetylcholinesterase as an enzyme label". In: *Electroanalysis* 9.4 (Mar. 1997), pp. 293–297.

[45]   D. Danon et al. "Use of cationized ferritin as a label of negative charges on cell surfaces". In: *Journal of Ultrastructure Research* 38.5-6 (Mar. 1972), pp. 500–510.

[46]   K. Mishra et al. "A simple, artificial-membrane feeding method for the radio-isotope labelling of Aedes aegypti polypeptides in vivo". In: *http://dx.doi.org/10.1179/136485905X6* 99.8 (Dec. 2013), pp. 803–806.

[47]   M. Sameiro and T. Gonçalves. "Fluorescent labeling of biomolecules with organic probes". In: *Chemical Reviews* 109.1 (Jan. 2009), pp. 190–212.

[48]   Angela Leung, P Mohana Shankar, and Raj Mutharasan. "A review of fiber-optic biosensors". In: *Sensors and Actuators B* 125 (2007), pp. 688–703.

[49]   Ye Tian et al. "Tapered Optical Fiber Sensor for Label-Free Detection of Biomolecules". In: *Sensors 2011, Vol. 11, Pages 3780-3790* 11.4 (Mar. 2011), pp. 3780–3790.

[50]   Guy D. Griffin et al. "Fiber-Optic Chemical Sensors for Competitive Binding Fluoroimmunoassay". In: *Analytical Chemistry* 59.8 (1987), pp. 1226–1230.

[51]   Frank Kleinjung et al. "Fibre-optic genosensor for specific determination of femtomolar DNA oligomers". In: *Analytica Chimica Acta* 350.1-2 (Sept. 1997), pp. 51–58.

[52]   Briliant Adhi Prabowo, Agnes Purwidyantri, and Kou-Chen Liu. "Surface Plasmon Resonance Optical Sensor: A Review on Light Source Technology". In: *Biosensors 2018, Vol. 8, Page 80* 8.3 (Aug. 2018), p. 80.

[53]   Asiyeh Jebelli et al. "Recent advances in surface plasmon resonance biosensors for microRNAs detection". In: *Biosensors and Bioelectronics* 169 (Dec. 2020), p. 112599.

[54] E. Kretschmann and H. Raether. "Radiative Decay of Non Radiative Surface Plasmons Excited by Light". In: *Zeitschrift fur Naturforschung - Section A Journal of Physical Sciences* 23.12 (Dec. 1968), pp. 2135–2136.

[55] Ewa Pol et al. "Evaluation of calibration-free concentration analysis provided by Biacore™ systems". In: *Analytical Biochemistry* 510 (Oct. 2016), pp. 88–97.

[56] Andrei V. Kabashin et al. "Silicon based total internal reflection bio and chemical sensing with spectral phase detection". In: *Optics Express, Vol. 17, Issue 23, pp. 20847-20852* 17.23 (Nov. 2009), pp. 20847–20852.

[57] Jose L. Melendez, Richard A. Carr, and Robert C. Keller. *Integrally formed surface plasmon resonance sensor*. 1997.

[58] Francesco Arcadio et al. "A Nanoplasmonic-Based Biosensing Approach for Wide-Range and Highly Sensitive Detection of Chemicals". In: *Nanomaterials 2021, Vol. 11, Page 1961* 11.8 (July 2021), p. 1961.

[59] Fiore Capasso et al. "Universal tool for surface plasmon resonance sensors realized in waveguides". In: *2021 IEEE Sensors Applications Symposium, SAS 2021 - Proceedings* (Aug. 2021).

[60] Nicholas M. Fahrenkopf et al. "The AIM Photonics MPW: A Highly Accessible Cutting Edge Technology for Rapid Prototyping of Photonic Integrated Circuits". In: *IEEE Journal of Selected Topics in Quantum Electronics* 25.5 (Sept. 2019).

[61] Enxiao Luan et al. "Silicon photonic biosensors using label-free detection". In: *Sensors (Switzerland)* 18.10 (Oct. 2018).

[62] A. Botsialas et al. "Broad-band Mach-Zehnder interferometers as high performance refractive index sensors: Theory and monolithic implementation". In: *Optics Express, Vol. 22, Issue 8, pp. 8856-8870* 22.8 (Apr. 2014), pp. 8856–8870.

[63] Katrin Schmitt et al. "Interferometric biosensor based on planar optical waveguide sensor chips for label-free detection of surface bound bioreactions". In: *Biosensors and Bioelectronics* 22.11 (May 2007), pp. 2591–2597.

[64] W. Bogaerts et al. "Silicon microring resonators". In: *Laser and Photonics Reviews* 6.1 (2012), pp. 47–73.

[65] Xuefeng Jiang et al. "Whispering-Gallery Sensors". In: *Matter* 3.2 (Aug. 2020), pp. 371–392.

[66] D. K. Armani et al. "Ultra-high-Q toroid microcavity on a chip". In: *Nature 2003 421:6926* 421.6926 (Feb. 2003), pp. 925–928.

[67] Martin D. Baaske, Matthew R. Foreman, and Frank Vollmer. "Single-molecule nucleic acid interactions monitored on a label-free microcavity biosensor platform". In: *Nature Nanotechnology 2014 9:11* 9.11 (Aug. 2014), pp. 933–939.

[68] Vanessa Zamora et al. "Cylindrical optical microcavities: Basic properties and sensor applications". In: *Photonics and Nanostructures - Fundamentals and Applications* 9.2 (Apr. 2011), pp. 149–158.

[69] Judith Su, Alexander Fg F.G. Fg Goldberg, and Brian M. Stoltz. "Label-free detection of single nanoparticles and biological molecules using microtoroid optical resonators". In: *Light: Science and Applications* 5.August 2015 (2016), pp. 2–7.

[70] Jian-Jun He et al. "Cascaded silicon-on-insulator double-ring sensors operating in high-sensitivity transverse-magnetic mode". In: *Optics Letters, Vol. 38, Issue 8, pp. 1349-1351* 38.8 (Apr. 2013), pp. 1349–1351.

[71] Dale Henneke et al. "Optimization of multiple-slot waveguides for biochemical sensing". In: *Applied Optics, Vol. 53, Issue 23, pp. 5169-5178* 53.23 (Aug. 2014), pp. 5169–5178.

[72] Enrique Valera, Winnie W. Shia, and Ryan C. Bailey. "Development and validation of an immunosensor for monocyte chemotactic protein 1 using a silicon photonic microring resonator biosensing platform". In: *Clinical Biochemistry* 49.1-2 (Jan. 2016), pp. 121–126.

[73] Muzammil Iqbal et al. "Label-free biosensor arrays based on silicon ring resonators and high-speed optical scanning instrumentation". In: *IEEE Journal on Selected Topics in Quantum Electronics* 16.3 (May 2010), pp. 654–661.

[74] Leslie J. Donato et al. "Evaluation of the genalyte maverick SARS-CoV-2 multi-antigen serology panel". In: *Journal of Clinical Virology Plus* 1.3 (Sept. 2021), p. 100030.

[75] Martin A.M. Gijs. "Magnetic bead handling on-chip: new opportunities for analytical applications". In: *Microfluidics and Nanofluidics 2004 1:1* 1.1 (Oct. 2004), pp. 22–40.

[76] Michael Zeinoun et al. "Configurable High-Frequency Alternating Magnetic Field Generator for Nanomedical Magnetic Hyperthermia Applications". In: *IEEE Access* 9 (2021), pp. 105805–105816.

[77] Claudia Matschegewski et al. "Biocompatibility of magnetic iron oxide nanoparticles for biomedical applications". In: *Current Directions in Biomedical Engineering* 5.1 (Sept. 2019), pp. 573–576.

[78] Kai Wu et al. "Magnetic nanoparticles in nanomedicine: a review of recent advances". In: *Nanotechnology* 30.50 (Sept. 2019), p. 502003.

[79] Jeff W.M. Bulte. "In Vivo MRI Cell Tracking: Clinical Studies". In: *AJR. American journal of roentgenology* 193.2 (Aug. 2009), p. 314.

[80] Andreas S. Lübbe, Christoph Alexiou, and Christian Bergemann. "Clinical Applications of Magnetic Drug Targeting". In: *Journal of Surgical Research* 95.2 (Feb. 2001), pp. 200–206.

[81] Jobin Jose et al. "Magnetic nanoparticles for hyperthermia in cancer treatment: an emerging tool". In: *Environmental Science and Pollution Research 2019 27:16* 27.16 (Dec. 2019), pp. 19214–19225.

[82] Helena Gavilán et al. "Magnetic nanoparticles and clusters for magnetic hyperthermia: optimizing their heat performance and developing combinatorial therapies to tackle cancer". In: *Chemical Society Reviews* 50.20 (Oct. 2021), pp. 11614–11667.

[83] Alexander Van Reenen et al. *Integrated lab-on-chip biosensing systems based on magnetic particle actuation-a comprehensive review.* May 2014.

[84] C. P. Moerland, L. J. Van IJzendoorn, and M. W.J. Prins. "Rotating magnetic particles for lab-on-chip applications-a comprehensive review". In: *Lab on a Chip* 19.6 (2019), pp. 919–933.

[85] Marco Donolato et al. "Novel readout method for molecular diagnostic assays based on optical measurements of magnetic nanobead dynamics". In: *Analytical Chemistry* 87.3 (Feb. 2015), pp. 1622–1629.

[86] Jaeyoung Yang et al. "Blu-ray based optomagnetic aptasensor for detection of small molecules". In: *Biosensors and Bioelectronics* 75 (Jan. 2016), pp. 396–403.

[87] Bo Tian et al. "Shape anisotropy enhanced optomagnetic measurement for prostate-specific antigen detection via magnetic chain formation". In: *Biosensors and Bioelectronics* 98 (Dec. 2017), pp. 285–291.

[88] Rokon Uddin et al. "Lab-on-a-disc agglutination assay for protein detection by optomagnetic readout and optical imaging using nano- and micro-sized magnetic beads". In: *Biosensors and Bioelectronics* 85 (Nov. 2016), pp. 351–357.

[89] Jianlong Wang et al. "Magnetic Nanoparticle Enhanced Surface Plasmon Resonance Sensing and Its Application for the Ultrasensitive Detection of Magnetic Nanoparticle-Enriched Small Molecules". In: *Analytical Chemistry* 82.16 (Aug. 2010), pp. 6782–6789.

[90] Yi Wang, Jakub Dostalek, and Wolfgang Knoll. "Magnetic Nanoparticle-Enhanced Biosensor Based on Grating-Coupled Surface Plasmon Resonance". In: *Analytical Chemistry* 83.16 (Aug. 2011), pp. 6202–6207.

[91] Agnes T. Reiner et al. "Magnetic nanoparticle-enhanced surface plasmon resonance biosensor for extracellular vesicle analysis". In: *Analyst* 142.20 (Oct. 2017), pp. 3913–3921.

[92] Enrique Valera, Melinda S. McClellan, and Ryan C. Bailey. "Magnetically-actuated, bead-enhanced silicon photonic immunosensor". In: *Analytical Methods* 7.20 (Oct. 2015), pp. 8539–8544.

[93] S Y Siew et al. "Review of Silicon Photonics Technology and Platform Development". In: *Journal of Lightwave Technology* 39.13 (2021).

[94] F. Boeuf et al. "A multi-wavelength 3D-compatible silicon photonics platform on 300mm SOI wafers for 25Gb/s applications". In: *Technical Digest - International Electron Devices Meeting, IEDM*. 2013.

[95] Kwang Yu Chu and A. Ralph Thompson. "Densities and Refractive Indices of Alcohol-Water Solutions of n-Propyl, Isopropyl, and Methyl Alcohols". In: *Journal of Chemical and Engineering Data* 7.3 (July 1962), pp. 358–360.

[96] U. V. Biradar and S. M. Dongarge. "Refractive Index of Salt (NaCl) from Aquous Solution". In: *International Journal of Computer & Mathematical Sciences* 4.12 (2015), pp. 33–39.

[97] Marina Cretich et al. "A new polymeric coating for protein microarrays". In: *Analytical Biochemistry* 332.1 (Apr. 2004), pp. 67–74.

[98] Giovanna Pirri et al. "Characterization of A Polymeric Adsorbed Coating for DNA Microarray Glass Slides". In: *Analytical Chemistry* 76.5 (Mar. 2004), pp. 1352–1358.

[99] Emre Özkumur et al. "Quantification of DNA and protein adsorption by optical phase shift". In: *Biosensors and Bioelectronics* 25.1 (Sept. 2009), pp. 167–172.

[100] Elisa Chiodi et al. "A Reliable, Label Free Quality Control Method for the Production of DNA Microarrays with Clinical Applications". In: *Polymers 2021, Vol. 13, Page 340* 13.3 (Jan. 2021), p. 340.

[101] Marina Cretich et al. "Overcoming mass transport limitations to achieve femtomolar detection limits on silicon protein microarrays". In: *Analytical Biochemistry* 418.1 (Nov. 2011), pp. 164–166.

[102] Alessandro Gori et al. "Screening Complex Biological Samples with Peptide Microarrays: The Favorable Impact of Probe Orientation via Chemoselective Immobilization Strategies on Clickable Polymeric Coatings". In: *Bioconjugate Chemistry* 27.11 (Nov. 2016), pp. 2669–2677.

[103] Larry Johnson. *Laser Diode Burn-In and Reliability Test*. Tech. rep.

[104] A. Bensoussan et al. "A unified multiple stress reliability model for microelectronic devices — Application to 1.55 μm DFB laser diode module for space validation". In: *Microelectronics Reliability* 55.9-10 (Aug. 2015), pp. 1729–1735.

[105] Subhankar Bedanta and Wolfgang Kleemann. "Supermagnetism". In: *Journal of Physics D: Applied Physics* 42.1 (Dec. 2008), p. 013001.

[106] Q. A. Pankhurst et al. "Applications of magnetic nanoparticles in biomedicine". In: *Journal of Physics D: Applied Physics* 36.13 (June 2003), R167.

[107] Louis Néel. "Théorie du traînage magnétique des substances massives dans le domaine de Rayleigh". In: *Journal de Physique et le Radium* 11.2 (Feb. 1950), pp. 49–61.

[108] William Fuller Brown. "Thermal Fluctuations of a Single-Domain Particle". In: *Physical Review* 130.5 (June 1963), p. 1677.

[109] S. H. Chung et al. "Biological sensors based on Brownian relaxation of magnetic nanoparticles". In: *Applied Physics Letters* 85.14 (Oct. 2004), p. 2971.

[110] Satoshi Ota and Yasushi Takemura. "Characterization of Néel and Brownian Relaxations Isolated from Complex Dynamics Influenced by Dipole Interactions in Magnetic Nanoparticles". In: *Journal of Physical Chemistry C* 123.47 (Nov. 2019), pp. 28859–28866.

[111] Alireza Bahadorimehr, Jafar Alvankarian, and Burhanuddin Yeop Majlis. "Magnetic force on a magnetic bead". In: *2012 10th IEEE International Conference on Semiconductor Electronics, ICSE 2012 - Proceedings* (2012), pp. 280–284.

[112] M. Giacometti et al. "On-Chip Magnetophoretic Concentration of Malaria-Infected Red Blood Cells and Hemozoin Nanocrystals". In: (Nov. 2018), pp. 1–1.

[113] Eunseop Yeom, Yang Jun Kang, and Sang Joon Lee. "Changes in velocity profile according to blood viscosity in a microchannel". In: *Biomicrofluidics* 8.3 (May 2014).

[114] Chen Chen and Junsheng Wang. "Optical biosensors: an exhaustive and comprehensive review". In: *Analyst* 145.5 (Mar. 2020), pp. 1605–1628.

[115] Tonio Blondi et al. "Analysis and modeling of layout scaling in silicon integrated stacked transformers". In: *IEEE Transactions on Microwave Theory and Techniques* 54.5 (May 2006), pp. 2203–2210.

[116] R. S. Popovic, Z. Randjelovic, and D. Manic. "Integrated Hall-effect magnetic sensors". In: *Sensors and Actuators A: Physical* 91.1-2 (June 2001), pp. 46–50.

[117] Hein Sprong, Peter Van Der Sluijs, and Gerrit Van Meer. "How proteins move lipids and lipids move proteins". In: *Nature Reviews Molecular Cell Biology 2001 2:7* 2.7 (July 2001), pp. 504–513.

[118] Patrick Lagüe, Martin J. Zuckermann, and Benoît Roux. "Lipid-Mediated Interactions between Intrinsic Membrane Proteins: A Theoretical Study Based on Integral Equations". In: *Biophysical Journal* 79.6 (Dec. 2000), pp. 2867–2879.

[119] Karen G. Fleming et al. "Thermodynamics of glycophorin A transmembrane helix dimerization in C14 betaine micelles". In: *Biophysical Chemistry* 108.1-3 (Mar. 2004), pp. 43–49.

[120]   Paul Wiggins and Rob Phillips. "Membrane-Protein Interactions in Mechanosensitive Channels". In: *Biophysical Journal* 88.2 (Feb. 2005), pp. 880–902.

[121]   Maddalena Venturoli et al. "Mesoscopic models of biological membranes". In: *Physics Reports* 437.1-2 (Dec. 2006), pp. 1–54.

[122]   Frédérick Jean Marie De Meyer, Maddalena Venturoli, and Berend Smit. "Molecular Simulations of Lipid-Mediated Protein-Protein Interactions". In: *Biophysical Journal* 95.4 (Aug. 2008), pp. 1851–1865.

[123]   Christoph G. Baumann et al. "Ionic effects on the elasticity of single DNA molecules". In: *Proceedings of the National Academy of Sciences USA* 94.12 (June 1997), pp. 6185–6190.

[124]   Gil Ariel and David Andelman. "Persistence length of a strongly charged rodlike polyelectrolyte in the presence of salt". In: *Physical Reviews E, Statistical, Nonlinear, and Soft Matter Physics* 67.1 (2003), pp. 11805–11814.

[125]   Timothy E. Cloutier and Jonathan Widom. "Spontaneous Sharp Bending of Double-Stranded DNA". In: *Molecular Cell* 14.3 (May 2004), pp. 355–362.

[126]   J. F. Allemand et al. "Loops in DNA: an overview of experimental and theoretical approaches". In: *European Physical Journal E, Soft Matter* 19.3 (Mar. 2006), pp. 293–302.

[127]   Justin P. Peters and L. James Maher. "DNA curvature and flexibility in vitro and in vivo". In: *Quarterly Reviews of Biophysics* 43.1 (Feb. 2010), pp. 23–63.

[128]   Jan Lipferta et al. "Double-stranded RNA under force and torque: Similarities to and striking differences from double-stranded DNA". In: *Proceedings of the National Academy of Sciences of the United States of America* 111.43 (Oct. 2014), pp. 15408–15413.

[129]   Hernan G. Garcia et al. "Biological consequences of tightly bent DNA: The other life of a macromolecular celebrity". In: *Biopolymers* 85.2 (Feb. 2007), pp. 115–130.

[130]   David Boal. *Mechanics of the Cell*. Cambridge University Press, 2012, p. 608.

A | Appendix: Peptide, antibodies and Dengue virus positive patients

The regional project READy goal was to help preparing a collaboration platform at regional level to help fighting new deseases and bioemergencies. One of the aims of the project was to develop and realize a diagnostic machine that could be used in hospital laboratories.

HTA srl, SCITEC-CNR, DiaPro srl, Ospedale Sacco and Politecnico di Milano collaborated to study the best solution for the tool, to understand the peculiarities these devices needed to present, to design, realize and finally test it.

Aim and planning It was decided to collect human plasma samples from patients that have resulted positive in Dengue virus (DENV) hospital tests.

The antigen covering the DENV capside can be emulated by the peptide E01. Thus, initial tests have been conducted on a laboratory bench setup on the peptide E01 with label-free hybrdization, passive label-based and active opto-magnetic labelling.

Then, since the technology (fluidic cell, microchips, functionalization process) is the same as the one for the previous case, we moved to the prototype to work with real human samples.

Issues Sadly, towards the end of the process we faced some issues. First, a whole batch of faulty chips prevented us to properly expose the waveguides. Then, calibration issues on the probe spotter made it difficult to reliably center the functionalization area on the MRR. Last, when the problems have been mostly solved, the secondary antibody showed some unexpected inefficiency, drastically reducing the quality of the outcome. These hiccups affected the measurements for the model system at low concentrations and all the tests of the prototype diagnostic device.

Antibodies model measurement   As explained in Chapter 2, the model we used mimics the presence of the DENV with the peptide E01 deposited on the chip's surface. The rabbit anti-E01 IgG antibody acts as target, binding to the spotted peptide. A second antibody, goat anti-rabbit IgG with biotine, is used to bind a streptavidin-coated MNP to the biomolecular system. The protocol is very similar to the one for DNA, with a second target step before the magnetic nanoparticles. Because of the additive step, the overall time needed to complete the hybridization is longer. The tested concentrations range from $10\,\mu g/mL$ to $10\,ng/mL$. At lower levels than $10\,ng/mL$, issues started impeding our measurements.

The binding effect have been measured in both label-free and passive labelled technique. The extracted results are in Figure A.1a.
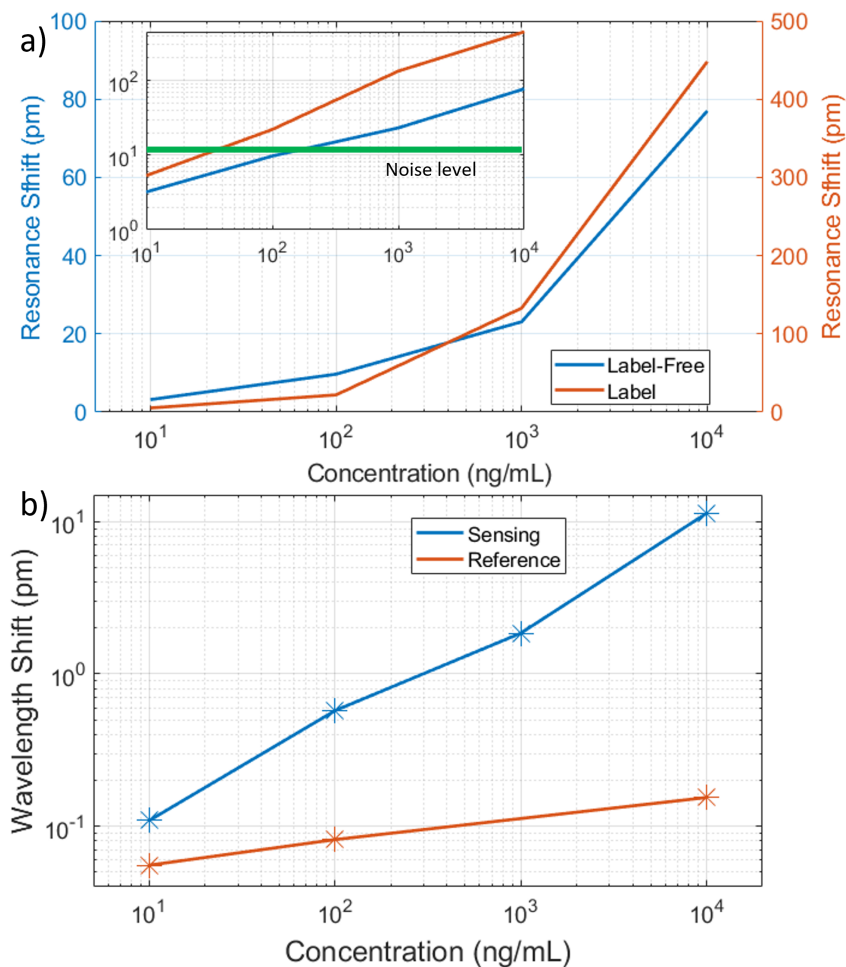
Figure A.1: Peptide E01 and antibody measurements. (**a**) Hybridization measurements are noise limited. (**b**) Opto-magnetic measurements suggest a limit of detection possibly below the lowest tested concentration.

In this case the MNP labels induce a wavelength shift that is roughly 5 times larger than the one caused by the target antibodies only. Noise limits the label free detection to $\simeq 100$ ng/mL, while the label-based technique signal reaches the noise level at $\simeq 30$ ng/mL.

Opto-magnetic measurements (Figure A.1b) show a behaviour similar to the one of DNA. At the lowest tested concentration, sensing and reference MRR signal were still distinguishable. Prolonging the data, the possible cross between the two curves would probably occur between 1 ng/mL and 1 ng/mL.

Diagnostic device   The diagnostic device has been tested with the same protocol used for the antibody model, but the sample containing the target molecule was human plasma from patients that have been in contact with the Dengue virus. Therefore in the bloodstream large quantities of antibodies that react to the DENV should be found.
As already explained, several biochemical issues prevented us to collect good hybridization data. However we were able to use this measurement to show the tool properties and capabilities.

In Figure A.2a the transfer functions of the 4 MRR collected over one long measurement are shown. From the transfer functions, with a Lorentzian fit the wavelength shifts over time are evaluated, Figure A.2b. The main visible shifts are due to temperature or liquid refractive index changes, since the MRR resonances move altogether. The difference track shifts by just 50 pm, corresponding to $\Delta T \simeq 0.5$ K or $\Delta n_{liq} \simeq 2.5 \times 10^{-3}$ RIU, over a 6 hours time period.
Even if no interesting biochemical results were obtained during these tests, we validated the reliability of the portable and semiautomatic diagnostic tool, proving that it can ease the work of biochemical and clinical laboratories operators.
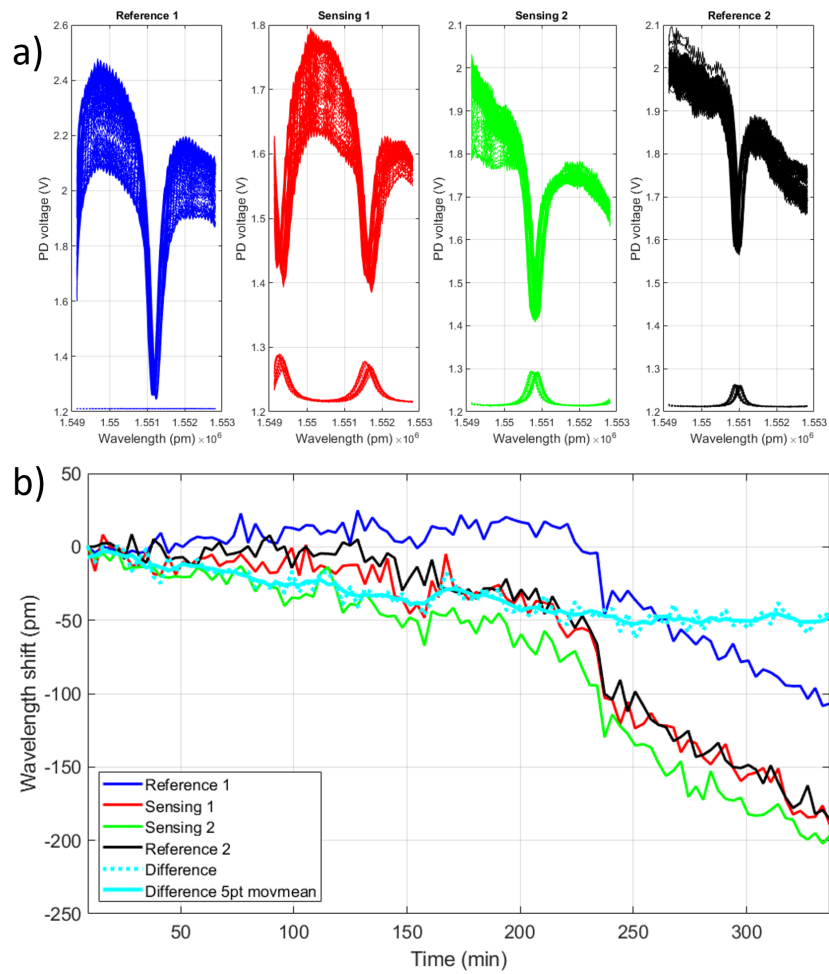
Figure A.2: Diagnostic device measurements. (**a**) Collection of the transfer functions of the 4 MRR under test and (**b**) their resonance shift over a long measurement time (6h).

Figure A.3: My colleague P. Piedimonte and I during the DENV tests [2].

List of Figures

List of Tables